SNOW DEPTH AND SWE ESTIMATION USING MULTI-SENSOR MICROWAVE AND OPTICAL REMOTE SENSING TIME SERIES DATA FOR INDIAN HIMALAYAS

SHIVANG PANDEY
August 2022

SUPERVISORS:
Dr., P. K., Thakur
dr.ing., H., Aghababaei

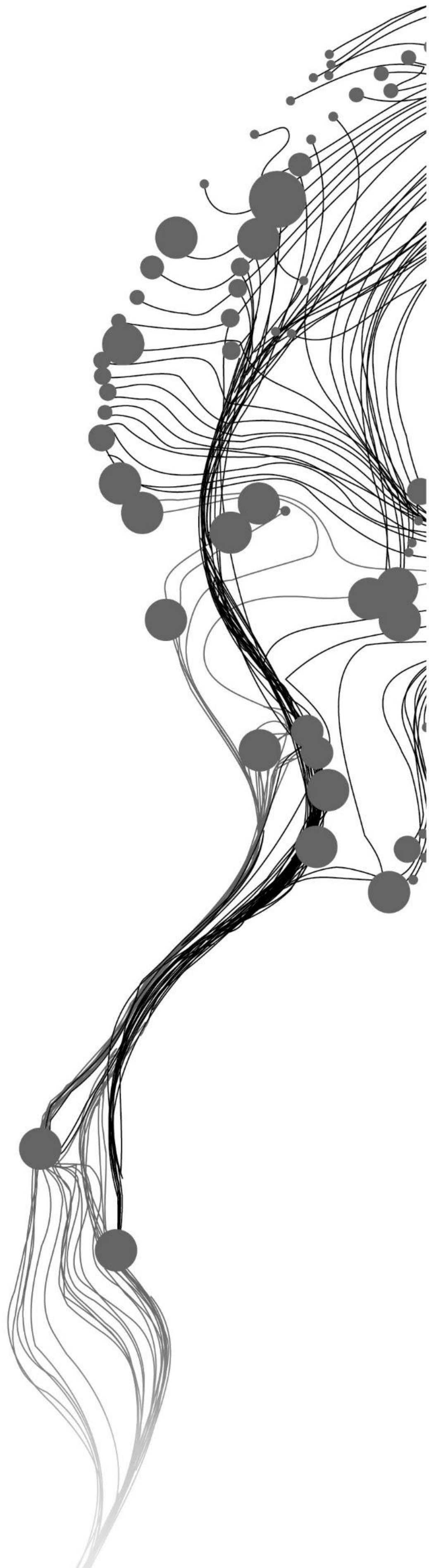

SNOW DEPTH AND SWE ESTIMATION USING MULTI-SENSOR MICROWAVE AND OPTICAL REMOTE SENSING TIME SERIES DATA FOR INDIAN HIMALAYAS

SHIVANG PANDEY
Enschede, The Netherlands, August 2022

Thesis submitted to the Faculty of Geo-Information Science and Earth Observation of the University of Twente in partial fulfilment of the requirements for the degree of Master of Science in Geo-information Science and Earth Observation.
Specialization: Geoinformatics

SUPERVISORS:
Dr., P. K., Thakur
dr.ing, H, Aghababaei

THESIS ASSESSMENT BOARD:
Prof. dr. ir., Persello, C (Chair)
Dr., S.P., Aggarwal (External Examiner, Director, NESAC)

Like how water, snow, and hail all contain the same element, but the same formless water solidifies to create hail or a mountain of snow, both of which have a shape, in same way knowledge transforms into an idea, and idea transforms into the triumph. ~ Tulsidas

ABSTRACT

Seasonal Snow in Indian Himalayas plays important role for water resources in South Asia which give water supply over the hundreds of millions of people living in most of the south Asian countries and hydro-electricity city to the several states of northern India. The study of SD and SWE can play a major role in forecasting yearly water supplies, flood prediction, and general climate research. Seasonal snow is an important part of the Himalayan hydrological system which gives water to billions of people and is a major source of generation of hydroelectricity in south Asian region. Depending on the availability and variety, mathematical model selection, and the hydro-meteorological conditions of the area of interest of the data, it is extremely difficult to estimate these two factors accurately. Estimation of SD and SWE using multi-sensor microwave and optical remote sensing time series data for Indian Himalayas is feasible but challenging. This thesis is intended to develop a model which can estimate SD and SWE values at optimal temporal and spatial resolution using multi-sensor data like active and passive microwave sensors, optical sensors and other climatological and topographical factors which affects snow and its physical properties.

In this research work, two study areas were the focus which are Beas and Sutlej basin in North-western Himalayas. Both basins are large water resources supply as well as snowmelt indulge in crucial role in terms to provide water supply. Water year October 2016 to September 2017 has been selected for this research work as per the optimum availability of the input dataset that has been used in this thesis work. Machine Leaning based model has been trained to obtain SD and SWE estimations from extracted input features from different dataset and prediction later has been done. Also, downscaling has been done for coarser resolution datasets. The quality of developed model (SVR) has been analysed by creating another machine learning model (RFR) to check how accuracy metrices are varying in similar circumstances in two different developed models.

As SD and SWE values varies a lot with elevation and aspect in the mountainous regions like Himalayas, an analysis has been done to observe how aggregated SD and SWE varying with these parameters. Analysis has been performed for month of February, which is approximately most snowy month of the years 2017, 2018 and 2019. Other ideas for improving the model quality, issued that arrived in research phase and drawbacks of the research work has been discussed in this report.

ACKNOWLEDGEMENTS

This research work is incomplete without all the people who were with me during this MSc course tenure. I would like to personally thanks to every individual who were with me in the journey of MSc degree and later in research phase.

My interest in this field of research is incomplete without constant guidance and mentorship of my supervisors. Dr. Praveen K Thakur briefed me beforehand that this topic is going to be not only a difficult one but also an adventurous journey in the remote sensing field. His guidance and extensive knowledge were boon for me to proceed in the field of this research work. At ITC, Dr. Hossein Aghababaei not only helped me in framing structure of this thesis but also constantly supported me with all my shortcomings that I faced. I would specially like to be thanking him for his immense help and guidance which was continued even when I am away from the ITC. Both supervisors uplifted me, in my knowledge, helped me to improve my conceptual knowledge, critical thinking, and scientific writing abilities through this entire thesis research phase. In addition, I would like to convey my sincere gratitude towards Mr. Mayank Upadhyay who helped me in my field work in north-western Himalayas of which I am very fortunate to tackle such harsh conditions which made my thesis more memorable.

Next, I would like to thank all my peers who made these two years memorable and helped me out in my research work from their busy MSc thesis schedule. I would like to thank Mr. Aravind Manimaran, Mr. Rohith Badrigari, Mr. Omkar Jadhav, Mr. Prateet Tiwari, Ms. Gautamee Baviskar, Ms. Margarret Ashmitha, Ms. Ketaki Jambhali, Ms. Neethu Narayanan and Ms. Priyadarsini Sivaraj who all are being part of ITC-IIRS family whose support was there with me throughout the journey of MSc. Each of them owes immense of gratitude from my side. I would like to thanks GID Department of IIRS, who trained me for difficulties in GIS & RS field and made me learn a lot from them throughout this course. I would also like to thank our ITC faculties, ITC student support and , my friends at ITC who made my ITC tenure one of the most memorable moments of my life.

Final words for the most loving people in my life, my parents, because of their constant love and support I was able to pursue this course and tackled all the difficulties. Love and support of my big brothers and my dear sister-in-law made easier for me to go through the difficult phases during this tenure. And I would like to thank each soul in the universe to be a part in my journey at the same time when I needed to be here the most. I hope I kept up with expectations of all the people who believed in me.

TABLE OF CONTENTS

LIST OF FIGURES

LIST OF TABLES

LIST OF ACRONYMS

API	Application Program Interface
ASAR	Advanced Synthetic Aperture Radar
AMSRE	Advanced Microwave Scanning Radiometer for EOS
AWS	Automatic Weather Station
BBMB	Bhakhra Beas Management Board
BTD	Brightness Temperature Difference
CT	Computer Tomography
CHIRPS	Climate Hazards Group InfraRed Precipitation with Station
CRIB	Center of Expertise in Big Geodata Science
DEM	Digital Elevation Model
DL	Deep Learning
DMSP	Defense Meteorological Satellite Program
DSD	Dry Snow Depth
EM	Electromagnetic
fSCA	fractional Snow Cover Area
GEE	Google Earth Engine
GHz	Giga Hertz
GRD	Ground range Detected
HMASR	High Mountain Asia Snow Reanalysis
InSAR	Interferometric Synthetic Aperture radar
IW	Interferometric Wide
LANDSAT	Land Remote-Sensing Satellite
LiDAR	Light Detection and Ranging
LST	Land Surface Temperature
PolSAR	Polarimetric Synthetic Aperture Radar
MAE	Mean absolute error
m.a.s.l	Mean absolute sea level
MIR	Mid-infrared
ML	Machine Learning
MODIS	Moderate Resolution Imaging Spectroradiometer
m.s.l	Mean Sea level
MW	Microwave
MWt	Megawatts
NDVI	Normalized Difference of Vegetation Index
NDSI	Normalized Difference of Snow Index

NETCDF	Network Common Data Form
NIR	Near-infrared
NWH	North-western Himalayas
OOB	Out of bag
PMW	Passive Microwave
PolSAR	Polarimetric Synthetic Aperture Radar
QA	Quality Assessment
RADARSAT	Radar Satellite
RF	Random Forest
RFR	Random Forest Regressor
RMSE	Root mean square error
S1	Sentinel-1
SAR	Synthetic Aperture Radar
SCA	Snow Cover Area
SCE	Snow Cover Extent
SCF	Snow Cover Fraction
SD	Snow Depth
SGD	Stochastic Gradient Descent
SLC	Single Look Complex
SNAP	Sentinel Application Platform
SNR	Signal-to-noise ratio
SRTM	Shuttle Radar Topography Mission
SSD	Surface Snow Depth
SSMI	Spectral Sensor Microwave Imager
SVM	Support vector Machine
SVR	Support Vector Regression
SWE	Snow Water Equivalent
TB	Temperature Brightness
UIB	Upper Indus Basin
USDA	United States Department of Agriculture
VH	Vertical-Horizontal polarization
VV	Vertical-Vertical polarization
WY	Water Year

1. INTRODUCTION

1.1. Background

Snow studies are the study about physical qualities of snow like the bulk properties of snowpack that are places in a particular area, changes happening there over time, and snow cover region aggregate properties (National Snow and Ice Data Center, 2016). Studies on the snow can be done by combining on-the-ground physical measuring techniques with remote sensing techniques to obtain a better knowledge of snow-related process over vast areas (National Snow and Ice Data Center, 2016). Several properties of snow play an essential role in its study like, the thickness of the snow, grain shape and size, height of snowpack, or Snow Depth (SD), the height of fresh snow (like, over a day), Snow Water Equivalent (SWE) and Water Equivalent of snowfall (Fierz et al., 2009). Snow's two most salient features are SD and SWE which broadly used in hydrological models like snow avalanche and snowmelt run off predictions (Thakur et al., 2017). While SD allude to the height of snowpack from surface base at ground to the top surface of the snow, SWE measures the water content present in the given snowpack, also SWE is directly proportional to SD and snow density. Depending on the availability and variety, mathematical model selection, and the hydro-meteorological conditions of the area of interest of the data, it is extremely difficult to estimate these two factors accurately. Estimation of SD and SWE using multi-sensor microwave and optical remote sensing time series data for Indian Himalayas is feasible but challenging. In this work, a Machine Learning based approach for SD and SWE estimation has been introduced and to get optimum spatial and temporal resolution.

1.2. Motivation

After polar regions, accumulation of ice, snow, and glaciers in the globe is found highest in the Himalayas, the source of important rivers in Southern part of Asia continent (Immerzeel et al., 2010). These rivers have a high potential for water supplies and hydropower generation. But in the start of May 2021, Bhakra Beas Management Board (BBMB) officials stated that the water level in the Gobind Sagar Lake (Himachal Pradesh, India), which serves as the reservoir for the Bhakra dam was 1,505.39 feet, was 56 feet down from the previous year's equivalent days (Kanchan Vasdev, 2021).The dam could be filled to a maximum height of 1,680 feet. The concerns are growing since the reservoir only has 10% of the 9.27 billion cubic meters of water it can hold. Any further drop in the level might result in the partner state's power plants and water supplies being shut down (Kanchan Vasdev, 2021). The senior management, on the other hand, thought that the monsoon would hit the region by mid-June and restock the dam. Power generation at the dam's powerhouses has been reduced by 20% to deal with the dire situation and restrict outflows (Kanchan Vasdev, 2021). The Bhakra dam has a total capacity of 1,415 megawatts of power generating (MWt). To keep the reservoir level in check, 14,000 cusecs of water is released from the dam against a 20,000-cusec intake (Shukla et al., 2017). Silt makes up at least 23% of the reservoir's filling capacity, causing the dam to quickly fill and empty. The reservoir covers an area of 168 square km, and the amount of silt entering the reservoir is far more than projected when the dam was built in 1963 (Shukla et al., 2017).The reservoir also supplies a source of drinking water for the three northern Indian states, as well as India's national capital, New Delhi (Shukla et al., 2017). Low water storage has been attributed to a lack of snow and rainfall during previous winters. Furthermore, in many sections of the Himalayas, unseasonal rain, and snow in May kept temperatures low and thereby decreased snowmelt. This is just an example of a dam based on one river of the western Himalayas. Similar cases of lack of snowfalls in the Northern Himalayas, leading to water shortage can be seen for other rivers like Beas and Indus (Vikas Vasudeva, 2021).

Our planet experiences significant cooling due to snow, and it gets affected the most due to solar radiation and dissipating energy of the snowmelt in summers (Shi & Dozier, 2000). An essential component of the Himalayan hydrological system is seasonal snow which gives water to billions of people and is a major source of generation of hydroelectricity south Asian region(Smith & Bookhagen, 2018), but due to lack of high-altitude measurements makes it difficult to assess and anticipate water supply in this region (Kirkham et al., 2019). The study of SD and SWE can play a major role in forecasting yearly water supplies, flood prediction, and general climate research (USDA Natural Resources Conservation Service, 2021). Studies have shown that snowmelt has greater importance in the field of agriculture also, as hydrological runoff models include snowmelt as a parameter in different phases like accumulating snowpack, melt water distribution and its distribution into ground water (M. Kumar et al., 2013). On top of that, snow studies using Remote Sensing techniques brought a revolution in SD and SWE estimation domain (Dietz et al., 2012). In recent times when a lot of satellites are capturing images on the different electromagnetic spectrum (like radar and optical) with a great temporal resolution, image fusion techniques can be very helpful for getting more information about a particular point of view and interpretation of it (S. C. Kulkarni & Rege, 2020). Grain size, impurity, and age of the snow can be obtained from visible wavelengths due to the high proportion of radiation coming from these wavelengths (Winther et al., 1999).

As there are so many difficulties on irregular terrains to get ground based in-situ measurements for SD and SWE, the combination of remote sensing techniques and ground measurement has widely been used to enhance the quality of data snow physical parameters in sample space and time domains. Snow parameters over extensively on-ground regions (Takala et al., 2011). Sensors which are widely used in studies of snow, ice and glacier like cryospheric studies generally are LiDAR (Light Detection and Ranging) and SAR followed by Passive Microwave (PMW) remote sensing (Deems et al., 2013; Leinss et al., 2014; Tedesco & Jeyaratnam, 2016). However, there is one drawback of LiDAR is that it can only use to determine the SD and cannot be used to measure other snow physical parameters like Snow grain size, snow wetness and snow density. Adding to that, cost to operate LiDAR is significantly higher as compared to microwave and other optical remote sensing sensors and it is dependent on weather conditions unlike microwave sensors (Deems et al., 2013). To overcome come this, space borne SAR, PMW and other optical remote sensing sensors which are globally available, PMW and SAR sensors have additional edge for cloud insensitivity, operability during night-time and that is why these both sensors are widely used in the measurement of snow physical parameters at good spatial and temporal resolution (Moreira et al., 2013; Thakur et al., 2012).

First, discussion of snow cover monitoring using SAR was happened in 1977 (Ulaby et al., 1977) where backscattering coefficient for snow was measured and frequencies, layers, and polarisations was used for the modelling of the same also (Zuniga et al., 1979). It has been seen that Ku-band, which having high frequency or frequencies which higher than this show high relation with SD and SWE for complex snow cover like standing or dry snow (Yueh et al., 2009) whereas X-band, which is low frequency microwave band or below than this can penetrate through this complex snow till the ground surface or soil which is underneath the frozen ground and it reflects as the radar backscatter signal. If it is the case of moist snow, which a transitional state of dry and wet snow, and wet snow itself, the scattering occurs from snow surface for wet snow and snow volume for moist snow because of water presence in snow particle. Water modifies the dielectric properties of snow as it has high dielectric constant itself and radar pulses' capacity of snow penetration also decreases (Abe et al., 1990). Typically, a snow-covered area's backscattering mechanism can be conceptualized from Figure 1-1. Different SAR techniques like InSAR and PolSAR which works on different principles have developed the methods is to utilize the target echoes which are received from snowpack created various applications for cryosphere-based microwave remote sensing.

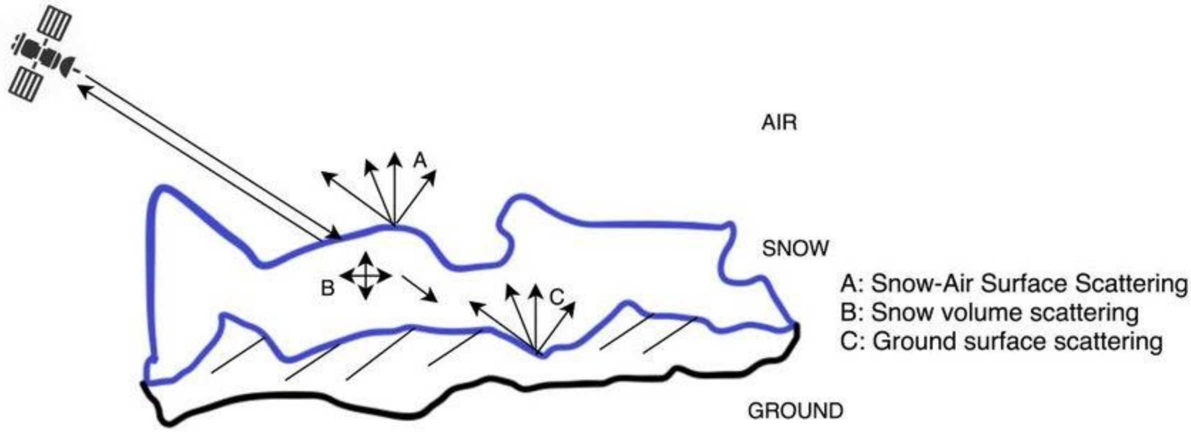

Figure 1-1: Backscattering structure of snow in mountainous region conceptual diagram (Thakur et al., 2012)

The core observation of PMW remote sensing with snow is that microwave radiation emitted from snow has strong relation with physical properties of snow, like stratification, grain size and snow density (Rosenfeld & Grody, 2000). Temperature Brightness (TB) of PMW data reflects information of scattering from snowpack like combined influence of liquid water content, particle size, snow density, and snow metamorphism along with dielectric properties of snowpack. Snow density, grain size, snow metamorphism and liquid water content along with dielectric properties of snow are the physical parameters of snow also their combination information can be obtained from the scattering value of PMW Temperature Brightness (TB) values as it is directly proportional to them. Snow physical parameters shows positive correlation with microwave radiation scattering but when airborne microwave sensors come into play, it shows a negative correlation with snow physical properties (Gan et al., 2013). Additionally, using daily ground-based snow depth data, it was discovered that snow density had a positive and negative relationship with latitude and elevation, respectively (X. Zhong et al., 2014).

Many studies have shown that topographical factors also play very crucial role in distribution of snow and physical properties of snow (Gharaei-Manesh et al., 2016; Q. Li et al., 2019a; Smith & Bookhagen, 2018). Several products of snow cover which are derived from PMW remote sensing have been widely used in application of global and regional climate change and to validate many climate and hydrological models (Brown & Mote, 2009; Brown & Robinson, 2011). Biggest advantage of PMW remote sensing is that its In contrast to visible and thermal infrared bands, which are unable to offer dual polarisation data at different frequencies, radiation can interact with snowpack via clouds (C. Liu et al., 2020; Majumdar et al., 2019; Tedesco & Jeyaratnam, 2016).

High reflectance and albedo of the snow in optical remote sensing range (0.350 to 1 μm) differs the snow from other majority of earth surfaces as reflectance from the snow is close to 100% (see Figure 1.2): It can also be said like that snow reflects back roughly whole the incident in optical wavelengths specially those which are above 1 μm which also often referred as mid-infrared or 'MIR' in which snow's reflectance from snow decreases significantly. Snow is much less reflective that certain types of vegetation in these wavelengths. Snowpack absorbs most of the radiation in such wavelengths. The difference between snow and other type of earth surfaces can be distinguished by such unique spectral characteristics of snow and remote sensing. Snowpack can penetrate in microwave wavelengths ranges which also implied at different wavelengths with snow optical properties. Penetration of snowpack in optical rays is till only 50 centimetres in visible spectrum. On other hand, signal quickly absorbs the surface and reflectance in infrared wavelength and only top few millimetres of snow cover properties get reflected (Dumont & Gascoin, 2016).

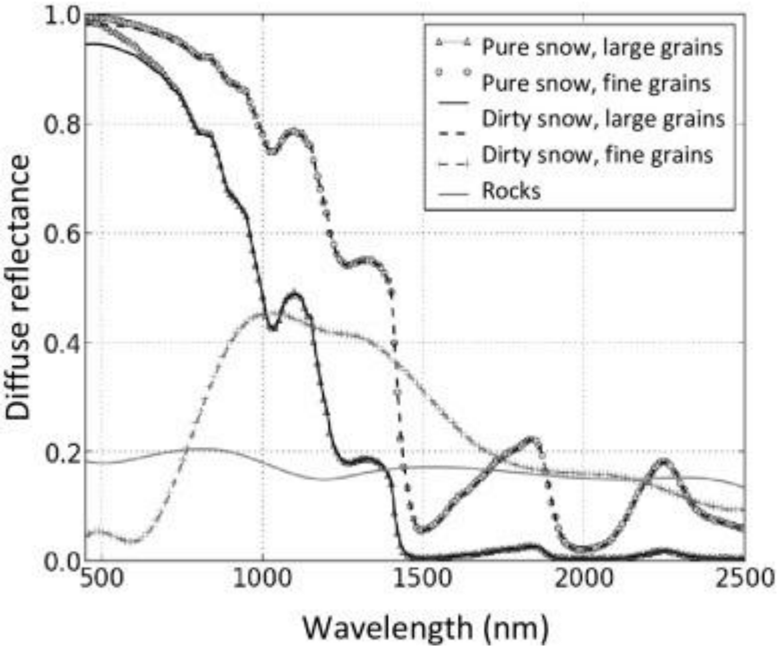

Figure 1-2: Diffuse reflectance properties of snow and soil in several wavelengths of Electromagnetic waves (Dumont & Gascoin, 2016)

These methods can show potential for extensive studies in complex snow cover regions like the Himalayas, where debris and forest regions are present using advanced computation like ML and DL algorithms(Bair et al., 2018; Breiman, 2001; J. Liu et al., 2019; Xiao et al., 2018a; Yang et al., 2020). Machine-learning and deep-learning technology power many aspects of remote sensing: from target recognition to semantic segmentation to spatial-temporal prediction, and they are increasingly present in snow parameter estimation and retrieval for developing a novel by integrating remote sensing data with SD and snow density data, one can estimate SD and SWE by use of machine learning with SD and Snow density's hundreds of field measurement. Many studies tell that snow physical parameters vary dramatically with spatial variability on a given date while estimating SWE (Avanzi et al., 2014; Broxton et al., 2019).

1.3. Research Problem

There are several products available online for SWE estimation in near real-time also, but each has its drawbacks. GlobSnow SWE product by the Finnish Meteorological Institute which gives monthly, but datasets are available only for the non-mountainous regions (Luojus et al., 2020) which will be not helpful for this area mentioned in this research. Similarly, Copernicus' SWE product which is daily but only from 35°N to 85°N (Takala et al., 2011), does not cover the above-mentioned study area to the full extent. Passive microwave observations (M. J. Brodzik, 2016) are generally not considered mountains because of coarse (~25km) resolution, and they are not able to do observation in deep snow like more than a meter (Smith & Bookhagen, 2018). In optical satellite images, it is difficult to distinguish between cloud and cloud like snwo deposits as both have a alike magnitude of spectral reflectance in the visible and near-infrared ranges (Kokhanovsky et al., 2018; Winther et al., 1999). Fusion of Radar and optical sensors for snow studies can affect spectral (Zhu et al., 2021) and temporal (Snapir et al., 2019) resolution which will be a hindrance to obtaining optimal results for SD and SWE estimations. The high-resolution characteristics of the sensor provide favourable conditions for the analysis the snow cover area related research. Nevertheless, having the similar reflectance spectrum characteristics of snow and cloud, optical remote-sensing monitoring of snow cover is greatly limited by weather conditions. Simultaneously, snow depth is hardly detected by optical sensors. Passive microwave can penetrate cloud layers for all-weather work and achieve the parameter of snow depth through the surface based on the sensitivity of different snow frequency. The model of retrieving snow depth from PMW data has created from simple linear regression to non-linear models considering complex meteorological and geographical factors. However, the SD 10 to 25km of spatial resolution is not suitable in areas like arid and semi-arid alpine region where the vertical drop is extremely significant. In practical application, snow depth mapping with higher spatial resolution is more useful for regional snow disaster evaluation and hydrological model establishment. Recent studies have demonstrated that higher snow depth mapping can be developed based on high-resolution geographic and meteorological data, together with downscaling microwave data or using active microwave sensors like SAR data can be used (L. Zhu et al., 2021a). But long repeat time along with shadowing and layover makes SAR studies difficult as regions remains unobserved. Creating InSAR and PolSAR results for large study is area is also difficult (Moreira et al., 2013).

1.4. Thesis Outline

This report has majorly been divided into 8 chapters and each chapter consists of several sub-chapters. Chapter 1 talks about introductory discussion followed by research identification and objectives of the thesis in Chapter 2. In Chapter 3, state of the start of different microwave (both passive and SAR) and optical remote sensing sensors in application of snow cover, SD and SWE has been discussed along with detailed physics behind the snow. Thereafter, study area, data materials and several tools has been discussed in Chapter 4. From Chapter 5 onwards the research methods that have been implemented in this thesis has been. Results has been included in Chapter 6 and in detailed discussion with each objective, sub-objectives and research questions has been mentioned in Chapter 7. In the last, conclusions and recommendation for the thesis work has been covered in Chapter 8. Appendices has been added for some additional information about Sensors and outputs generated in this thesis.

2. RESEARCH IDENTIFICATION

2.1. General Objective

This research will be focussed on many objectives:

1. Feature Extraction using radar and optical data for SD and SWE applications.
2. To develop a machine learning-based model which can estimate SD and SWE based on the features extracted from multi-sensor data.
3. To estimate SD and SWE at efficient resolution using features obtained from the fusion of high-resolution multi-sensor data.

2.2. Sub Objectives

1. To extract the different types of features using different multi-sensor data for SD and SWE estimation
2. To find an optimal downscaling technique for the fusion of extracted features from multi-sensor data.
3. To create a generalized model based on features extracted from the collection of datasets and implement a machine learning model for SD and SWE estimation
4. To validate the model using ground observation data

2.3. Research Questions

The following research questions will be addressed-

1. Referring to sub-objectives 1:
    a) What are input optimal features that can be obtained from multi-sensor data?
    b) What are the useful SAR modalities (i.e., SAR, PolSAR, InSAR) for optimal feature extraction?
2. Referring to sub-objective 2:
    a) Which downscaling technique should implement to get SD and SWE at an efficient resolution?
    b) What optimal resolution can be obtained by the fusion of multi-sensor data?
3. Referring to sub-objective 3:
    a) How can input features extracted affect the training of the model from SVR?
    b) What are the optimal parameters of SVR to create a generalized model that gives results with minimum error?
4. Referring to sub-objective 4:
    a) What is the performance of SVR based model, and how precisely can SD and SWE be estimated?

2.4. Innovation

With the successful completion of this research work is to create a model for estimation of SD and SWE in near-real time with accuracy nearer to the ground observations which can help in forecasting yearly water supplies, flood predictions, and general climate research.

3. LITERATURE REVIEW

This chapter deals with state-of-the-art of PMW, SAR, and optical sensors and approaches in the context of cryosphere research with particular emphasis on SD and SWE. At first, there will be a general overview of the electromagnetic (EM) properties of snow is provided in section 3.1 for coherently guiding the reader through this chapter, followed by climatological and topographical effects on Snow has been discussed in section 3.2. Thereafter, an in-depth discussion is put forward about microwave and optical remote sensing specific literatures concerning the estimation of SD and SWE in section 3.3. Fusion of multiple sensors datasets for estimation of SD and SWE applications has been discussion in section 3.5. In the last, downscaling of coarse resolution data of SD and SWE has been discussion in section 3.6

3.1. Electromagnetic Properties of Snow

Most remote sensing-based applications are built upon the theories of the EM wave effects and matter, with the exceptions being those which rely on gravimetric measurements (Tedesco & Jeyaratnam, 2016). The characteristics of snow in the microwave and optical(visible/near-infrared) regions are briefly reviewed in this section. Noted that since use of multi-sensors datasets is primary topic of concern in this thesis, the relevant microwave and multi-sensors datasets are succinctly mentioned along with some other climatological and topographical datasets .

3.1.1. Snow Reflectance in the Visible/Near-Infrared and Thermal-Infrared Regions

Freshly fallen snow seems brighter to human's eye as compared to the metamorphic snow such as firn and depth hoar. This is due to because flat spectral reflectance has high values across the entire visible EM spectrum (Figure 2.1). Moreover, the spectral reflectance values are indirectly proportional to the grain size of ice or snow. In essence, with having the least grain size, fresh snow exhibits the highest albedo (sometimes more than 90%) whereas for metamorphosed and dirty snow it is usually in the range of 20- 40%. Additionally, the snowpack's water content is liquid indirectly affects the albedo as it results in grain size growth and subsequent recrystallisation and metamorphosis (Tedesco & Jeyaratnam, 2016).

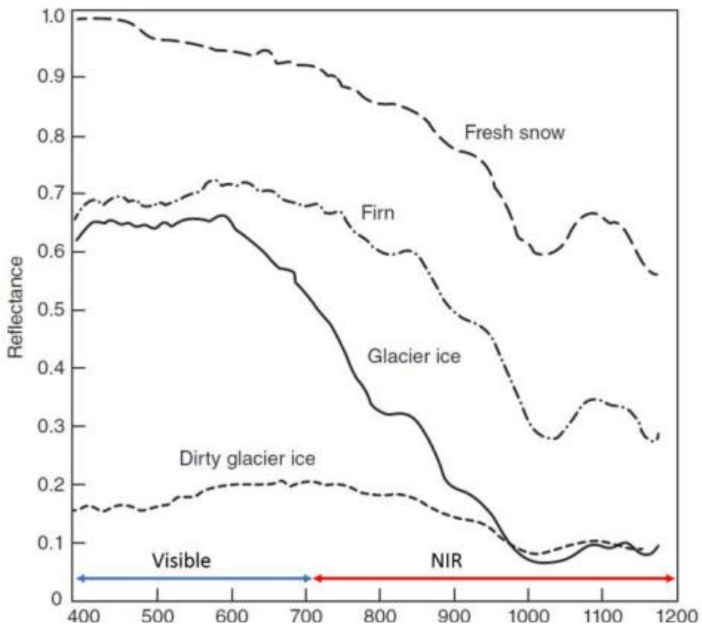

Figure 3-1: Spectral reflectance curve in the high frequency ranges for different snow and ice surfaces. Adapted from (Dumont & Gascoin, 2016)

Figure 2.1 shows the reflectance peaks occur between 400 and 600 nm (visible portion) and close to 800 nm in the near infrared (NIR). However, in the thermal infrared (3 μm – 100 μm) and higher wavelength regions of the EM spectrum, the snow reflectance is quite low. Also, the thermal emissivity of snow lies in the range of 0.965 to 0.995 with the maximum being at 10 μm (Tedesco & Jeyaratnam, 2016).

3.1.2. Microwave Region

Microwaves play a substantial role in the cryosphere research domain because they can pass through the Earth's atmosphere almost without any obstruction and can significantly interact with the snowpack volume. Due to the porous structure of snow, which in effect, is composed of three material phases— air, ice and water, the interaction of microwaves occurs with all these constituent phases (Leinss et al., 2014; Petrenko & Whitworth, 2002). Essentially, the microscopic structure of snow can be characterised based on the microwave wavelength, for which the dielectric properties of air, ice and water need to be considered along with other features of the snow medium (Leinss et al., 2014).

Dielectric Properties of Air, Ice and Water

Due to the significant water vapour content in the atmosphere, the microwave absorption owing to the water vapour saturated air in a snowpack of few meters' depth is negligible. Accordingly, the relative permittivity of water vapour saturated air in snow (ϵ_{air}) has been calculated to be about 1.00059 (Bryan & Sanders, 1928)

In the case of ice, a solid-state body, as indicated in (1), complex permittivity' is quite small and hence, radio waves below less 1 GHz EM wave (which are radiowaves) have large penetration, from several hundred metres to even kilometres. However, with higher the frequency, the radio wave's penetration capacity declines (about 1 m at 20 GHz) (Warren & Brandt, 2008). It has also been found that with increasing temperature, there is a slight increase in both imagery and real portion of the dielectric permittivity (Matzler & Wegmuller, 1987). Furthermore, this real part ($\Re(\epsilon ice)$ = 3.179) between 10 MHz and 100 GHz exhibits essentially no frequency dependency, and for measuring seasonal snow properties using microwave remote sensing, the imaginary part can be neglected (Bohleber et al., 2012; Leinss et al., 2014; Warren & Brandt, 2008).

$$\epsilon_{ice} = R(\epsilon_{ice}) - j\Im(\epsilon_{ice}) \quad (1)$$

where, ϵ_{ice}, $R(\epsilon_{ice})$, and $\Im(\epsilon_{ice})$ are the complex permittivity, relative permittivity (based on vacuum as unity) and the relative loss factor of ice respectively with j being the imaginary unit, and the negative sign is appearing as snow is a lossy dielectric medium (Evans, 2016).

Liquid water, on the other hand, is responsible for strong microwave absorption in snow and Debye relaxation peak calculates its relative permittivity. For water at 0°C, this peak is located at approximately 10 GHz, i.e., at the centre of the radio window. As a result, the relative permittivity (ϵ_{water}) varies greatly with the change in microwave frequencies, from ϵ_{water} < 5 (about 100 GHz) to ϵ_{water} ≈ 87 (below 10 GHz) (Buchner et al., 1999; Ellison et al., 1996).

Spatial Distribution and Length Scales of Snow

The three constituent phases of snow (air, ice, and water) exhibit spatial distribution across many length scales, the smallest being the crystal edges of dendritic snow crystals having length scales in the order of micrometres or below (Leinss et al., 2014).While single ice grains in the snowpack display length scales in the range of a few tens of micrometres to a few millimetres, the depth of an entire snowpack can vary from meters to several kilometres and is strongly dependent on the topography (Fassnacht & Deems, 2006; Ma & Tzler, 2002; Sturm & Benson, 2004). Such multi-scale variation of the snow properties is primarily governed by the snow accumulation, metamorphosis, and ablation processes (Fassnacht & Deems, 2006).Hence, to understand and describe the snow and microwave interactions, all the relevant scales need to be assessed. In fact, for remote sensing systems, it is actually the resolution of the observing sensor that defines these length scales (Leinss et al., 2014).

Snow as a Homogeneous and Effective Medium

AS SD is much smaller than the incident microwave wavelength ($\lambda 0$), then the snowpack can be modelled as a non-scattering homogeneous medium having an effective (or complex) permittivity ϵ_{snow}. In such a case, the interference pattern resulting from the whole group of scatterers (each having length d) present in a cube of length $\lambda 0$ needs to be considered to theoretically understand this non-scattering mechanism. Since $d \ll \lambda 0$, the scattering characteristics of all the ($\lambda 0/d$) scatterers is shown as Rayleigh scattering. A more detailed description in this regard is provided by (Leinss et al., 2014).

Snow as a Heterogeneous Medium

Snow can also act as a heterogeneous medium composed of small ($\lambda 0 \approx 10d$) or large ($\lambda 0 \approx d$) ice grains. For both these scenarios, the idea that the medium isn't dispersing does not apply, therefore scattering effects must be considered (Leinss et al., 2014).

In the first case, the Rayleigh scattering can again be applied to describe the scattering characteristics of the medium. The relatively larger ice grains scatter the microwave radiation more strongly owing to the higher dependence on the radar cross-section. This eventually leads to volume scattering which takes place because of the constructive interference in all directions. Thus, the ice grain size is a significant factor for the occurrence of volume scattering within the snowpack (Tsang et al., 2007).

when the wavelength and the size of the ice grain match (for frequencies higher than 100 GHz), Mie scattering is used to describe the scattering mechanism instead of Rayleigh scattering. However, the incident wave's propagation direction and coherence cannot be determined because of multiple scattering and as such are entirely lost (M. Hallikainen et al., 1987; Tsang et al., 2007).

Snow Anisotropy

After snowfall, fresh snow (after accumulation) exhibits an isotropic random structure containing inclusions of ice and snow that are X-band wavelength smaller. In the following steps, the weight of the fresh snow settles and compresses it. As a result, the previous randomly oriented microstructure gradually transforms into an anisotropic medium consisting of horizontally aligned snow particles. Eventually, these horizontally shaped particles undergo further metamorphosis to form isotropic structures, and finally, weeks later height hoar (which come under the snowpac) plus firn (granular form of snow) are formed which display vertically aligned structures.

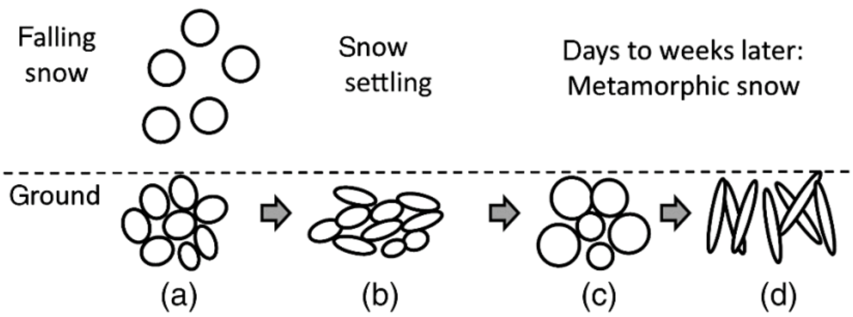

Figure 3-2: Snow metamorphism steps. (a) Random (b) Horizontal structures (c) Isotropic (d) Vertical Structures. Adapted from (Leinss et al., 2014)

The entire chain of processes that govern this snow metamorphosis process has been experimentally evaluated using X-ray computer tomography (CT) scans (Riche et al., 2013). A simplistic conceptual diagram is provided (Figure 3-2) to understand this transformation process clearly.

Snow as a Multilayered Structure

A snowpack is formed from layers of snow that have accumulated over time. So, when the microwave interaction of snow is concerned, the respective measurements need to be conducted for different layers displaying varying physical properties of snow and consequently, different refractive indices (Leinss et al., 2014). In this case, multilayer and multiple-scattering radiative transfer models have been applied for obtaining reliable simulation results related to snow microwave emission and backscattering (Mätzler & Wiesmann, 1999; Picard, Sandells, & Löwe, 2018; Royer et al., 2017; Tuzet et al., 2017).

Speckle Formation by the Snowpack

Although plane wavefronts propagating through homogeneous media are not distorted, in the context of snow as an effective homogeneous medium, it has been observed that the wavefronts get significantly deteriorated due to the snow-ground surface and snow-air surface scatterings (Figure 1). These plane wavefronts are also affected by the varying densities and volume scattering within a snowpack. In actuality, the interference of these warped wavefronts causes a speckle, which is an intensity pattern with a randomly distributed intensity which is a common phenomenon for all scattering surfaces (particularly the rough ones) which interact with coherent EM waves such as SAR and LiDAR (Goodman, 2007; Leinss, 2015). Due to the inherently spatial nature of speckle, the backscattered signal undergoes heavy spatial modulation, and as a result, suitable spatial averaging is an essential factor that needs to be incorporated for obtaining statistically significant measurements. Moreover, for snow related studies which rely on the phase information of the backscattered signal, large temporal changes in the snow surface (caused by wind drift, snow depth and density variations) lead to strong decorrelations in the phase and the speckle patterns, thereby posing difficulty in obtaining results with sufficient quality (Leinss, 2015).

3.2. Climatological and Topographical Effects on Snow

The three important parameters which describes seasonal snow cover are SD, SWE and snow density, and the evaluation of water resources, surface energy balances, various hydrologic processes, and earth's ecosystems are all significantly impacted by these variables(X. Zhong et al., 2018). These parameters pf snow cover get effected by topography of the region also. Topographical parameters like elevation, aspect, slope and vegetation cover correlates highly with snow cover spatial resolution. For example, *in-situ* data in British Columbia, Canada affects snow cover from 80%-90% . Similar study in in Swiss Alps shows that SD increases with increase in elevation to certain altitude, after that it decreases at the topmost elevations (Grünewald et al., 2014). (Rees et al., (2014) also mentioned that terrain strongly correlates with SD and SWE in the Daring Lake area (Canada).

Additionally, vegetation has an impact on where snow covers the ground. (Kuusisto, 1984) observed that the most snow was accumulated in exposed places, close to forest borders, and in sparse woodlands within of forests. Zhong et al. (2014) also found that forests have snow densities 8%–13% lower than open fields. A major contributing factor to these lower accumulations in forests is the canopy's ability to intercept snow (Faria et al., 2000; Winkler et al., 2005). There is a wide range of variation in the distribution of SD in mountains, which is heavily influenced by meteorological and topographic factors (Balk & Elder, 2000; Elder & Dozier, 2000; Erickson et al., 2005; Pflug & Lundquist, 2020).

3.2.1. Topographical effect on snow property distributions

Numerous studies discovered that the four topographic factors of height, slope, aspect, and maximum upwind slope significantly and consistently affected the SD distribution across time, which is similar to other studies (M. Kumar et al., 2013; Winstral & Marks, 2002). As a proxy for solar radiation (Elder et al., n.d.; McClung & Schaerer, 2006) and northness, the slope parameter has been found to account for a considerable portion of the snow distribution in steep terrain (Fassnacht & Deems, 2006). The most important factor influencing the distribution of snow depth in this investigation was slope. Elevation can be very important for large scale of data (Fassnacht et al., 2003) and has been shown high correlation with flat and forested terrain (Fassnacht et al., 2018). It has been known that elevation and slope are correlated hence, slope also affects SD and SWE a lot due to its high feature importance towards it (L. Zhu et al., 2021a).

Studies also been shown that SD gets a lot affected by elevation and latitude. There is an increase in SWE also has been observed due to latitude and elevation Hultstrand et al., 2022; X. Y. Zhong et al., 2021)

3.2.2. Land Cover influence on snow property distributions

The scattering and attenuation degree of microwave emission energy of various land cover are different, which is a significant factor for retrieving SD. A huge difference of polarization between snow cover and the bare surface, and the horizontal polarization is much smaller than the radiation BT of vertical polarization. AS SD increases, the polarization effect of microwave radiation enhanced, the dual polarization BT of different frequencies tends to be consistent and there is free snow cover. In arid and semi-arid regions, water, frozen soil and cold desert will be misjudged as snow cover due to the similar microwave radiation characteristics. Snow cover should be accurately distinguished from other land covers before retrieving snow depth.

The radiation BT of snow cover in the high-frequency channel decrease obviously. Thus, the BTD between high and low frequency channels is used as scattering index, its change and threshold value are used as a characteristic index in retrieval algorithm. In the actual snow depth microwave radiation modelling, the influence of surface roughness (high mountain, hilly, flat, etc.) and land cover parameters (glacier, vegetation, forest, desert, desert, etc.) should be considered. Moreover, microwave radiation can penetrate snow and detect radiation from the surface beneath, which shows as the detection results are affected by the volume scattering caused by the difference of soil physical properties in vertical direction. Therefore, the natural environmental differences of snowfields must be considered comprehensively in snow depth retrieval. (Deronde et al., 2014; Faria et al., 2000; Salomonson & Appel, 2004; Yu et al., 2012; L. Zhu et al., 2021a)

3.2.3. Effect of Climatological on snow property distributions

Due to temperature changes or an influx of recently fallen snow, SD and SWE might vary significantly between successive days (Hultstrand et al., 2022). Changes in snow cover has seen to be largely governed by temperature. Both SWE and SCE was strongly correlated with temperature in Yukon basin. During melt season, both SWE and SCE decreased during a period of temperatures around 0 °C and increased in fall when temperatures again were around 0 °C (Q. Li et al., 2019b).

Azmat et al. (2017) found a correlation between temperature increase (decrease) and SCA decrease (increase) and hence a streamflow increase (decrease). The strongest correlations were found during pre-monsoon or snowmelt season. They furthermore saw an inverse correlation between precipitation and SCA during pre-monsoon and monsoon season, but a positive correlation during the winter season. The correlation was stronger for the higher elevation zones. Temperature was also seen to control SCA varies in the basin of

Gilgit River in the western part of Himalayas, with snowmelt as well as subsequent increase in streamflow because of high temperatures, and low temperatures resulting in delayed snowmelt (Tahir et al., 2016).

3.3. Estimation of Physical Snowpack Parameters using microwave and optical sensors

3.3.1. SD Measurement

Snow depth measurement is still a challenging topic in the remote sensing domain due to numerous uncertainty sources such as the topography induced snow density and microstructure variations (Leinss et al., 2014). However, significant efforts have been made to minimise these uncertainties, thereby achieving sufficiently accurate site-specific SD results. In the context of SD retrieval using SAR, the research works have mainly emphasised on estimating dry snow depth (DSD) (Esmaeily-Gazkohani, Granberg, & Gwyn, 2010; Li et al., 2017; Liu et al., 2017), however, there have been recent studies on fresh and wet snow depth measurements (Leinss et al., 2018, 2014). Additionally, the well-known PolInSAR based tree height inversion algorithms are also applicable for SSD estimation (Leinss et al., 2014).

The regular Sentinel-1 C-band illumination of the earth's surface by the constellation allows scientists to quantify backscatter in both vertical-vertical (vv) and vertical-horizontal (vh) or, co-polarization and cross-polarization, transmit-receive, respectively. A four-component model can be used to approximate the total backscatter (σ_{pq}^{tot}) for transfer signal snowfall with no living things in it (Ulaby et al., 1977):

$$\sigma_{pq}^{tot} = \sigma_{pq}^{air-snow} + \sigma_{pq}^{snowvol} + e^{(-2\tau/\cos\theta)} \cdot \sigma_{pq}^{grnd} \qquad (2)$$

with $\sigma_{pq}^{air-snow}$ the backscatter from the air-snow interface $\sigma_{pq}^{snowvol}$, the ground's higher-order interactions with the snow volume, as well as the snow volume's backscatter, and backscatter from the ground $\sigma_{pq}^{snowvol-grnd}$, all attenuated by the snowpack through $e(-2\tau_p/\cos\theta)$. The optical snow thickness (τ_p) and radar incident angle (θ) both affect attenuation levels. Frequently, and, $\sigma_{pq}^{air-snow}$ are disregarded (J. Zhu et al., 2018)and thus not further considered.

Due to dry snow's limited vv-polarization at C-band absorption or scattering, the co-polarized, σ_{vv}^{0}. observations exhibit little fluctuation during the winter. The snow's depletion and melting over spring, however, is shown to cause a dramatic (~5 dB) drop in σ_{vv}^{0}. This supports earlier research showing the substantial signal attenuation and reflection caused by wet snow as well as dry snow (Nagler et al., 2016; Shi & Dozier, 2000). Furthermore, it confirms past findings that snowmelt mapping may be accomplished using C-band vv-polarized data (Tsai et al., 2019). Wet SCA reduces surface area, which increases absorption, is what causes the increase in, VV polarization. near the end of the snowmelt season in late spring. (Snapir et al., 2019). Surface thawing and flora greening up in places without snow can both enhance dispersion simultaneously (Snapir et al., 2019). The snowpack only attenuates the fourth part in equation (2), the backscatter from the ground surface, when the snow is wet, dominates the evolution of σ_{vv}^{0}. during the snow season. The second term represents the scattering in vv-polarization that takes place inside a dry snow volume., but it is typically too little to make a difference at C-band.

Sentinel-1's cross-polarized σ_{vh}^{0} measurements gradually rise as (dry) snow falls over the winter. This indicates a rising depolarization of the entering v-polarized signal due to inhomogeneities in the snow volume, Ice crystal bonds or clusters, as well as anisotropic or higher sampling on ice crystals, are all examples of scattering that is not uniform. The chances of scattering grow as the snowpack's thickness increases because it lengthens the radar signal's travel across it (Moreira et al., 2013; Ulaby et al., 1977). It should be considered that in theory, the backscatter in co-polarization is likewise impacted by this anisotropic and multiple scattering. (σ_{vv}^{0}), but with a much smaller impact than the ground surface. We postulate that the significant decrease in σ_{vh}^{0} snow's ability to absorb and reflect signals during ablation is a result of the snow's moisture as well as a reduction in snow volume dispersion in a shallowing snowpack (Leinss et al., 2014; H. Li et al., 2017; Majumdar et al., 2019; Thakur et al., 2017). The second and fourth terms in Eq. (2) are both necessary to explain the changes in σ_{vh}^0 (Snapir et al., 2019).

In general, there is a larger link between the cross-polarization ratio, $\sigma_{vh}^0/\sigma_{vv}^0$. (in linear scale, converted to dB) and snow depth than , σ_{vh}^0. By using the ratio, one can somewhat offset the impacts of temporal changes in the terrain, the vegetation, and the snowpack, which have an impact on both co- and cross-polarization. During the fall and winter, $\sigma_{vh}^0/\sigma_{vv}^0$. rises as a result of the increased volume scattering σ_{vh}^0. for essentially constant surface scattering σ_{vv}^0. The ratio falls during spring melt as a result of the relative larger drop of , σ_{vh}^0 in comparison to σ_{vv}^0. As a result, moist snow's sensitivity to snow depth is significantly less definite. Variations in , $\sigma_{vh}^0/\sigma_{vv}^0$ may result from strong melt events with large liquid water volumes. since moist snow layers more powerfully reflect and absorb the signal(Snapir et al., 2019). Although it may be less noteworthy at C-band than at higher frequencies and every once in a while be remedied by freeze thaw of snow prior to actually Sentinel-1's early hours (6 a.m.) and late in the evening (6 p.m.) overpass times, this impact is expected to have a puzzling effect on the C-band sensitivity to SD. Similar to how recurrent melt-refreeze cycles can change the snowpack's microstructure and stratigraphy, they can have an effect on backscatter signals. The major objective of this work is to map the SD in dry snow. However, the effectiveness of the retrievals over the length of the whole snow season and wet snow conditions have both been examined (Thakur et al., 2017).

The cross-polarization ratio ($\sigma_{vh}^0/\sigma_{vv}^0$; in dB) data taken by Sentinel-1 are used as the basis for the SD (m) retrieval procedure. Additionally, it incorporates 1 km² snow cover (SC; 1 if present, 0 if absent) from MODIS as well as fractional forest cover (of evergreen species) from the global consensus land cover dataset (Dumont & Gascoin, 2016). First, for each location I and time step t, a change detection index (hereinafter referred to as snow index, SI; in dB) is calculated (Ulaby et al., 1977). This index connects freezing and melting of the snow with changes in time in Sentinel-1 $\sigma_{vh}^0/\sigma_{vv}^0$.

Snow cover's microwave radiation properties resemble those of freezing ground, frigid deserts, and precipitation (Grody & Basist, 1996). Using a decision tree, Grody & Basist, (1996) were able to eliminate scattering signs from freezing ground, frigid deserts, and precipitation that could interfere with the accurate SCA identification (Table 3). We deleted the criteria that contained 85 GHz channels in order to fully utilise without an 85 GHz channel, SSMIS brightness temperature data is unavailable. (Che et al., 2008a).

Table 3-1: Steps to differentiate between snow from precipitation, differentiate a cold desert from a frozen ground. K stands for Kelvin.

Steps		Conditions for SSM/I		Conditions for SSMIS
1. Scattering signature	or	$(Tb19V - Tb37V) > 0\,K$ $(Tb22V - Tb85V) > 0\,K$		$(Tb19V - Tb37V) > 0\,K$
2. Precipitation	or	$Tb22V \geq 259\,K$ $(254 \leq Tb22V \leq 258\,K\ and\ (Tb19V - Tb37V) \leq 2\,K)$	or	$Tb22V \geq 259\,K$ $(254 \leq Tb22V \leq 258\,K\ and\ (Tb19V - Tb37V) \leq 2\,K)$
3. Cold deserts	and and	$(Tb19V - Tb19H) \geq 18\,K$ $(Tb19V - Tb37V) \leq 10\,K$ $(Tb37V - Tb85V) \leq 10\,K$	and	$(Tb19V - Tb19H) \geq 18\,K$ $(Tb19V - Tb37V) \leq 10\,K$
4. Frozen ground		$(Tb19V - Tb19H) \geq 8\,K$		$(Tb19\,V - Tb19H) \geq 8\,K$

Steps	Conditions for SSM/I	Conditions for SSMIS
and	$(Tb19\,V - Tb3\,7\,V) \leq 2\,K$	and $(Tb19V - Tb37V) \leq 2\,K$
and	$(Tb22V - Tb85V) \leq 6\,K$	

Wet snow makes it difficult to utilizing microwave radiation, for estimation of SD and SWE. As the snow medium's liquid water concentration rises, volume scattering will be largely outweighed by microwave radiation absorption (M. Hallikainen et al., 1987). We have discovered that it is required to segregate In order to more accurately employ a snow-depth retrieval technique, PM data that evaluated how the snowpack disturbing wet or dry snow or melting of the snow. The SVR based SD retrieval method used several and wet and dry snow classification techniques has been used to remove dry snow from the total SCA (P. R. Singh & Gan, 2000; Walker & Goodison, 1993):

$$T_{b37V} < 250K \tag{3}$$

$$T_{b19V} - T_{b37V} < 9K \tag{4}$$

$$T_{b37V} - T_{b37H} < 250K \tag{5}$$

$$P_{factor} = \frac{T_{b37V} - T_{b37H}}{T_{b37V} - T_{b37H}}, P_{factor} > 0.026 \tag{6}$$

the variation in horizontal polarisation between the PMW TB values of 18 and 37GHz was used by (Chang et al., 1987) to build a method for passive remotely sensed of SD over snowfields that are generally uniform. Based on mathematical calculations and research, this algorithm

$$SD = 1.5\,[T_{b18H} - T_{b37H}] \tag{7}$$

In horizontal polarization, T_{b18H} and T_{b37H} are TBs at 18 and 37 GHz, respectively, and a method for passive remotely sensed of snow height over snowfields that are generally uniform. Info from of the snow volume dispersion is picked up at 37 GHz, while data from the surface of the ground the snow is incorporated at 18 GHz. Estimation of SD and SWE has been affected with snow volume r square value is has indeed been enchanced by field observations of the SD, is thus the fundamental concept of the spectral gradient approach..

The forest area proportion was taken into consideration here based on Reference (Foster et al., 1997a) findings regarding forest influence:

$$SD = \frac{a[T_{b18H} - T_{b37H}]}{1-f} \tag{8}$$

where *a* is variable coefficient, while *f* is the tree cover area fraction.

For SMMR data, the coefficient (slope) of the regression between is the the changes happens in regression line's standard deviation and the snow depth as determined by weather stations and the TB(18H) and TB(37H) values' spectral gradient is 0.78 cm. For the SSMI TB data, the SMMR 18GHz channel was swapped out for the 19GHz channel. The findings indicate that the coefficients is 0.66 and the regression line's standard deviation is 5.99 cm. The changed algorithm is as follows:

$$SD = \frac{0.78[T_{b18H} - T_{b37H}]}{1-f} \quad (7)$$

(for SMMR data from 1978 to 1987)

$$SD = \frac{0.66[T_{b19H} - T_{b37H}]}{1-f} \quad (8)$$

(for SMM/I data from 1987 to 2006)

3.3.2. SWE Measurement

The definition of SWE, which is essentially the how much snow weighs which is lying on the ground, may be defined as product of SD (ΔZ_{snow}) and snow density (ρ_{snow}), as illustrated below equation:

$$SWE = \langle \rho_{snow} \rangle \Delta Z_{snow} \quad (9)$$

Snow Density as a Governing Factor

The microwave propagation speed depends on the dry snow density which again governs the backscatter signal delay particularly in the 10 MHz to 1 THz range (Leinss et al., 2015). As discussed earlier, $\Re(\epsilon_{snow})$ is also dependent on ρ_{snow} given by Eq. (9). Thus, precise estimated values of SD or SWE , the snow density have to be properly measured. In case of fresh snow, the snow-density lies in between 0.03 and 0.12 g/cm3 , which then increases for vertical structures (depth hoar and firn) due to the occurrence of gradual snow metamorphosis (Judson & Doesken, 2000; Leinss et al., 2015; Roebber, Bruening, Schultz, & Cortinas, 2003). As a result, ρ_{snow} = 0.5 g/cm3 is common for dry or standing snow prior to the onset of snow melting. However, the seasonal snow density ($\rho_{critical}$) rarely exceeds 0.55 g/cm3 . Typically, $\rho snow$ = 0.83 g/cm3 is observed for firn located deep underneath glaciers and ice sheets (Leinss et al., 2015). Moreover, the density of solid ice (ρ_{ice}) has been experimentally found to be 0.917 g/cm3 (Spencer, Alley, & Creyts, 2001).

Many studies have been shown a linear relationship for SD estimation between SD and TB value differences. This algorithm uses spectral polarisation difference (SPD) (Aschbacher & Rott, 1989; Chang et al., 1987; Foster et al., 1997b). The difference between TB values at frequencies like 19 GHz and 37 Ghz is used to compute the PMW TB difference. A drawback of such a linear method is that it loses a lot of accuracy after a certain depth. It should be mentioned that depending on the features of the area, the projected snow depth's accuracy varies substantially. A study done by (Davis et al., 1993) has shown linear relationship between TB difference values and SD in order to get around these limitations. They found that factors like grain size, density, etc. should be considered when estimating SD. According to Goita et al. (2003), the link between the two attributes (PMW TB difference and SD) varies according on the kind of flora and cover present in the region where the snow is found. By employing SSMI (Special Sensor Microwave/Imager) data and an artificial neural network (ANN) technique to predict the SD, (Tedesco et al., 2004a) tested their findings against an existing algorithm accuracy metrices like R^2, MAE and RMSE. By using a fusion of dataset and machine learning model based on SVR for SSMI radar pictures, Zahir and Mahdi (2015) assessed the snow depth. As a result, an R-squared of 0.9 and an RMSE of 6.97 cm were obtained. In addition, Liang et al. (2015) combined SSMI data with the optical sensor of a MODIS image. Although there has been a lot of research employing microwaves, it is deduced area covered under the sensor is small- and has corase temporal resolution.

The issue stated as a restriction in microwave images can be resolved by using optical which can repeat the pas in good temporal resolution. The optical remote sensing sensor radiation from sun, however, only pierce a few inches of snow, unlike microwaves. As a result, the depth must be inferred. Snow is known to steadily

increase a surface's reflectivity up to a particular thickness. Baker et al., (1991) , as a result of the snow's ability to reflect light. By analysing the link between SD and fSCA which reflects some part of pixel that is covered in snow, Romanov & Tarpley, (2004) estimated the SD values with 30 cm arid, semi-arid regions. Some factor which affects SCF like forest cover fraction, was taken into consideration by Romanov & Tarpley, (2007) when estimating the SD in both a forest and non-forest regions. The estimated snow depth's validation result showed an RMSE of roughly 10 cm when applying the study's deduced empirical equation. Therefore, obtaining the SCF for each pixel unit is the most crucial step in the process of measuring snow depth using optical pictures. NDSI or NDVI could be used as independent variables in a quadratic equation to estimate the SCF, according to Salomonson & Appel, (2004) A technique of calculating the SCF using a straightforward equation with the reflectance of snow and land was proposed by Romanov et al. in 2003. Using Landsat 7 Enhanced Thematic Mapper Plus (ETM+) imagery, Salomonson & Appel, (2004) suggested an NDSI-based first-order equation and validated the outcomes of an empirically obtained equation. Lu et al., (2015) suggested utilising an estimating equation based on an exponential function and for each variable, SCF has been calculated such as NDSI, Ratio Snow Index (RSI), and Difference Snow Index (DSI). The validation using Landsat 7 ETM+ revealed that the RSI estimation has the highest R-square value (0.83).
It has been found logical that the given equation in Kim, (2018) was able to calculate the SCF indirectly utilising an index that was connected with the SCF in order to gather information that is difficult to estimate. Existing formulae, however, have a drawback in that the SCF tends to be if the independent's value is significant is more than a predetermined value and underestimated if it is less than a predetermined value. Additionally, current formulae only take into account one element to estimate the SCF, despite the fact that the SCF changes with changes in other fcators.

NDVI helps for determining the value of SCF which exhibits a value of at least 0.72 if the NDSI is larger than 0.68. Additionally, if the NDVI value is lesser than 0.06, the SCF It will at certainly have value 0.28 based on the NDSI value as follows:

$$\mathrm{SCF} = \begin{pmatrix} 0.58\mathrm{e}^{23.1(\mathrm{NDSI}-0.68)^2} + 0.42\mathrm{e}^{-286.68(\mathrm{NDVI}-0.06)^2} & \mathrm{NDSI} \le 0.68, \mathrm{NDVI} \ge 0.06 \\ 0.58\mathrm{e}^{23.1(\mathrm{NDSI}-0.68)^2} + 0.42 & \mathrm{NDSI} \le 0.68, \mathrm{NDVI} < 0.06 \\ 0.58 + 0.42\mathrm{e}^{-286.68(\mathrm{NDVI}-0.06)^2} & \mathrm{NDSI} > 0.68, \mathrm{NDVI} \ge 0.06 \\ 1, & \mathrm{NDSI} > 0.68, \mathrm{NDVI} < 0.06 \end{pmatrix}$$

Above list of equations are the outcomes of estimating the SCF using the deduced equations. As can be observed, the graph shapes of the equations based on linear and exponential functions are comparable, and the RMSE that was determined by confirming the two equations' estimates of SCF are also comparable.. Gaussian function-based equation was useful to determine SCF are superior to those obtained using the other equation. The two equations used in the prior investigation yielded an RMSE of 0.26, but the proposed equation used in this study yielded an RMSE of 0.24. This was considered to mean that while the proposed formula provides the best explanation for the general trend, the NDSI and NDVI's respective standard deviation (Kim, 2018).
An exponential function has been devloped from the SD calculation equation because it is generally known that the SD increases as the SCF rises, an exponential function has the form of. As a result, employing the SCF, the SD may be calculated using the following equation. Because so much of the country is hilly, wherein snowfall of 10 cm or even more occurs, the Republic of Korea normally experiences less than 10 cm of snowfall, and visibility of snow is difficult because of fog, clouds, etc. Maximum permitted SD using below formulae is 6.97 metres:

$$\mathrm{SD} = 6.95 * \mathrm{e}^{0.67*SCF} - 1 \qquad (10)$$

SWE Estimation using Multiple Differential Interferograms

Recently, a temporal integration-based approach incorporating a stack of differential interferograms have been developed by Leinss et al. (2015). Although limited to dry snow, it avoids the phase unwrapping problem (Chen & Zebker, 2002), reduces decorrelation and is insensitive to orbit and atmospheric disturbances. However, the prerequisites for applying this method include sufficiently high radar wavelength (results in negligible volume decorrelation) and a high temporal resolution (Leinss et al., 2015). Essentially, by summing up the absolute dry snow phase differences (ϕ^{u}_{snow}) obtained from a dense differential interferogram time-series, it is possible to isolate the phase fluctuations attributing to the temporal decorrelations, thereby improving the signal-to-noise ratio (SNR) (Leinss et al., 2015). Accordingly, the relation between this integrated or summed up phase (ϕ^{u}_{snow}) and the change in SWE (ΔSWE) from time t_m to t_s (m and s representing the master and slave images respectively) can be well approximated by Eq. (30). Moreover, the optimal value of the free parameter $\vartheta \approx 1$ maximum anticipated depends on snow density and the incidence angle (Leinss et al., 2015).

$$\Delta\mathrm{SWE} = \mathrm{SWE}(t_s) - SWE(t_m) = \frac{\lambda_0\,\Delta\phi^{u}_{snow}}{2\pi\theta\left(1.59+\theta^{\frac{5}{2}}\right)} \qquad (11)$$

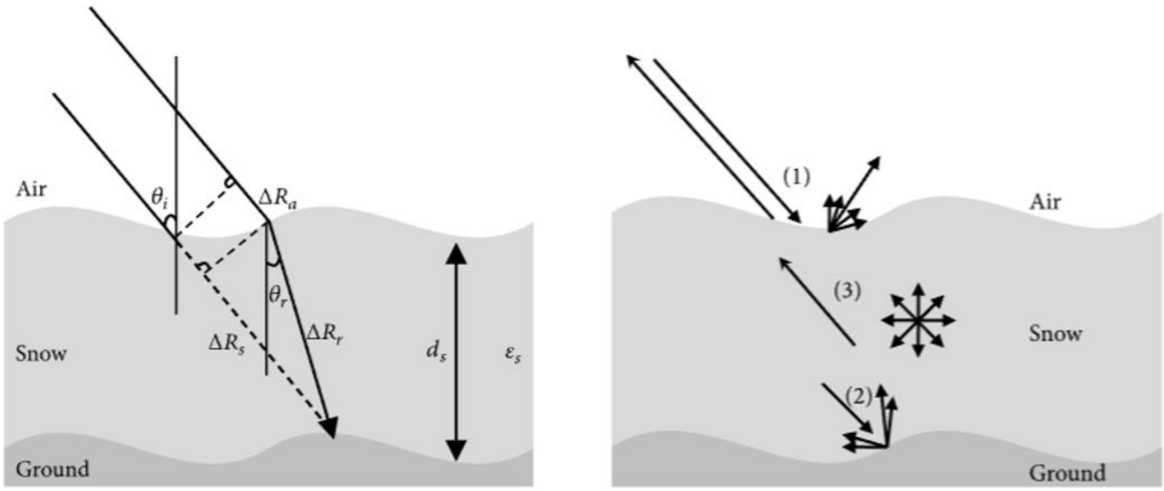

Figure 3-3: (a) Geometry of radar wave in snow and (b) scattering mechanism in snowpack (surface scattering in air-snow and snow-ground interface; volume scattering at snow grains within snowpack); (1) surface scattering at air-snow interface; (2) surface scattering at the ground-snow interface; (3) volume scattering at snow grains within the snowpack

Radar waves propagate differently with and without snow, as seen in Figure 3.3(a). The radar wave range for a stationary pixel is represented as ΔR_s. without snow cover and ΔR_a+ΔR_r with snow-air contact's refraction by radar beam causes snow to fall. The range discrepancy is depicted as

$$\Delta R = \Delta R_s - (\Delta R_a + \Delta R_r) \qquad (12)$$

The equation for the relationship is $\varepsilon_s = 1 + 1.6\rho + 1.86\rho^3$, and the formula for the refraction index, n , is $\varepsilon_s = n^2$ (Mätzler, 1996)

According to (12), the snow phase ϕ_{snow}, which can be derived as (Guneriussen et al., 2001; Rott et al., 2004)

$$\begin{aligned}\phi_{snow} &= -\frac{4\pi}{\lambda} d_s \left(cos\theta_i - \sqrt{\varepsilon_s - sin_i^2} \right) \\ &= -\frac{4\pi}{\lambda} d_s \left(cos\theta_i - \sqrt{1 + 1.6\rho + 1.86\rho^3 - sin^2\theta_i} \right)\end{aligned} \quad (13)$$

Where, λ is the radar wavelength, θ_i is the incidence angle, d_s is the snowpack depth, and ε_s is the snow's dielectric constant.

And SWE, the mass of snow on the ground, is the volume of water that results from the total melting of a snowpack. It can be pictured as

$$SWE = \langle \rho \rangle \mathrm{d}_s \quad (14)$$

where, $\langle \rho \rangle$ is the average value of the snowpack's snow density.

For snow densities between 0 and 0.5 g/cm^3, the interferometric phase difference and SWE can be approximated linearly using the nominal Envisat ASAR incidence angle. (Guneriussen et al., 2001; Rott et al., 2004).

$$\phi_{snow} = -\frac{4\pi}{\lambda} 0.87 \Delta SWE \quad (15)$$

Equation (14) shows that there is a linear approximation between variations in SWE and the InSAR phase difference of dry snow, ϕ_{snow} . Incidence angle θ_i and snow density ρ according to equations (13) and (15). In order to determine how these two variables, incident angle, I and snow density, would affect the phase difference acquired from InSAR measurement in the dry snow, a preliminary sensitivity analysis was created.

The sensitivity of incident angle θ_i and snow density ρ on the snow phase term ϕ_{snow} can be determined from (13) using the law of error propagation by considering the partial derivatives:

$$\frac{\partial \phi_{snow}}{\partial \theta_i} = -\frac{4\pi}{\lambda} d_s \left(-sin\theta_i - \frac{sin\theta_i cos\theta_i}{\sqrt{1+1.6+1.86\rho^3 - sin^2\theta_i}} \right) \quad (16)$$

$$\frac{\partial \phi_{snow}}{\partial \rho} = \frac{4\pi}{\lambda} d_s \frac{0.8 + 2.79\,\rho^2}{\sqrt{1+1.6+1.86\rho^3 - sin^2\theta_i}} \quad (17)$$

Several combinations of these values were confirmed in equations (16) and (17) during the early sensitivity analysis. The mean snow density in the central Tianshan Mountains during a winter season (December to April of the following year) varied between 0.14 g/cm^3 and 0.25 g/cm^3, according to field measurement data. Additionally, the incident angle varies for each spaceborne sensor platform. Envisat ASAR IMS data with a nominal incident angle range of 19.2°-26.7° were used in this application. Additionally, RADARSAT-1 and RADARSAT-2 are satellite data sources that are often utilised in InSAR measurement. They have pixel sizes that range from 3 to 100 m and incident angles that range from 20 to 49°. As seen from equation (13), the incidence angle is crucial to understanding the relationship (Esmaeily-Gazkohani et al., 2014).

The following components make up the entire repeat-pass interferometric phase, assuming that there is coherence between the two SAR scans and synchronisation of snowfall or redistribution:

$$\phi = \phi_{flat} + \phi_{topo} + \phi_{snow} + \phi_{atm} + \phi_{noise} \quad (18)$$

where the phase discrepancies for flat earth and terrain, respectively, are caused by variations in the target's and satellite's distances. Phase noise is referred to ϕ_{noise} . heterogeneous atmospheric (ionosphere and/or troposphere) disparities in air propagation. There is a discrepancy in the two-way propagation between both the snowpack as well as the surrounding air, or ϕ_{snow} is caused by the radar wave's refraction in the dry snowpack (see 13). When these elements are dissociated from one another, the phase acquires significance and value. Therefore, once ϕ_{flat}, ϕ_{topo}, and ϕ_{atm} have been eliminated, ϕ_{snow} would be the only variable left to retrieval of the SD and SWE.

As was mentioned in the preceding section, Dry snow's backscattering is governed by subsurface scattering just at snow-ground contact. The main factors that influence backscattering include the dielectric constant, the scattering surface's roughness, and other physical features. Temperature has little impact on the relative dielectric constant, which ranges from 2 to 4 (Ulaby et al., 1977). Since liquid water is present dielectric constant, even a small amount of it causes the soil's dielectric constant to rise significantly. Dielectric constant of soil could be greater than those of ice and dry materials in colder regions (M. T. Hallikainen et al., 1985; Liou, 1996) which suggests that some liquid water in the soil is still liquid and has not yet frozen. The soil temperature, total water content, and soil texture are the main factors that affect how much liquid water is present in frozen soil. The temperature is typically the most crucial element (X. Y. Zhong et al., 2021).As a result, whenever the soil temperature is below zero degrees Celsius, given the high liquid water content of the soil, temperature changes have a disproportionately large impact on the dielectric constant. (Liou, 1996)

According to research by Baghdadi et al., (1997), Bernier, (1999) and Gauthier et al., (2001) the soil's dielectric constant fluctuates with soil temperature when it is below 0 °C, as well as the scattering just at snow-ground interface is sensitive to a soil's dielectric constant. The thermal resistance of snow influences the temperature of the underlying soil. These researchers created a method for calculating the SWE using only a few field snow observations and SAR data based on their findings. Instead of using just one snow image, a ratio image has been employed to reduce the effects of topography and speckle on the SAR images.

The main loss mechanism for incident microwave radiation is volumetric scattering, and it is possible to empirically connect the TB of a certain frequencies or polarisation (H or V) to the SWE of a snowpacks. greater than 15 GHz [(Fierz et al., 2009; Gan et al., 2013). The National Snow and Ice Data Center (NSIDC) offers these passive microwave TB data in EASE Grid format at the University of Colorado Boulder. Equation was used to get the NSIDC's 1979–1987 SMMR SWE data (19),

$$SWE(mm) = 4.77\ [T_{b18H} - T_{b37H}] \tag{19}$$

Where TB18H and TB37H, which stand for the horizontally polarised TB at 18 and 37 GHz, respectively. From equation, the NSIDC's SSMI SWE data for the years 1987 to 2007 were obtained (20) (Armstrong & Brodzik, 2002),

$$SWE(mm) = 4.77\ [T_{b18H} - T_{b37H} - 5] \tag{20}$$

This differs only marginally from equation's formulation (19). Using land cover data, the SWE is adjusted for the quantity of surface forest cover per day (National Snow and Ice Data Center, 2016)

$$SWE(mm) = \frac{SWE}{(1 - Forest\%)} \tag{21}$$

3.4. Fusion of Optical and Microwave Remote Sensing Data

The ability to integrate images from same sensor or from several sensors, as well as the availability of a variety of imaging systems, have improved the capacity for interpretation compared to the use of a single image, image fusion is finding more and more uses in remote sensing. The method is frequently used to merge optical images with various spatial resolutions (Carper et al., 1990; Chavez et al., 1991) as well as images containing a range of information contents from microwave as well as and optical sensors (Baronti et al., 2004; Gungor & Shan, 2012; Lee et al., 2005). In many applications, including such land cover mapping, aiming to increase's methodological and object visualisation (Haack et al., 2014) , urban area detection (Garzelli, 2004), and forest categorization (Pugh et al., 2004) mineral mapping (Ramadan et al., 2006) optical-microwave image fusion work has been done previously .

Because optical and microwave results have ability to complement one other, the combining of radar with optical data further improves the results' interpretability and dependability. While the shape, orientation, roughness, and water particles of bright objects on the surface of the earth are all highly sensitive to radar, optical data only captures the reflectance for ground cover inside the visible and near-infrared range (Pugh et al., 2004).

3.5. Downscaling of Snow propertiers

For hydrological and climatological forecasts, precise, current estimates of SD and SWE are essential due to the spatiotemporal implications of seasonal snow variations on environmental and socioeconomic processes. PMW remote sensing has been efficiently utilized , consistently, and affordably monitor SWE just at global to regional scale. However, because passive microwave observations have a limited spatial resolution, local scale estimations are vulnerable to significant inaccuracies (25 x 25 km). By using related auxiliary datasets with a finer spatial resolution, Grid datasets' spatial resolution can be increased by using regression downscaling methods (Margot Flemming, 2020; Walters et al., 2014; L. Zhu et al., 2021a). These methods have been effectively used in multi-sensor datasets, such as estimations of soil moisture, but little research has been done on their use with datasets linked to snow (L. Zhu et al., 2021).

3.6. Machine Learning for Snow properties

Machine-learning and deep-learning technology power many aspects of remote sensing: from target recognition (Guo et al., 2019; Wu et al., 2019; F. Xu et al., 2019; Zhang et al., 2019) to semantic segmentation (Senthilnath et al., 2020; Y. Xu et al., 2018)] to spatial-temporal prediction (X. Chen et al., 2020), and they are increasingly present in snow parameter estimation and retrieval (Ahmad et al., 2019; de Gregorio et al., 2019; Xue & Forman, 2015). Tedesco et al., (2004) constructed a neural network to estimate the SD and SWE, which showed the highest accuracy compared with the other four retrieval algorithms. By employing a neural network to calculate snow depth and SWE in the Samsami Basin, Iran, Tabari et al., (2010) came to a similar conclusion. Theoretically speaking, microwave BTD enhances with the increases of SD, while SD exceeds a defined limit (50 cm) there will be a large error in the estimation results. By learning and summing up a huge quantity of data, the neural network can solve a variety of complicated problems that arise in large-scale retrievals, such as non-linear modelling, classification, and association, and it does so without depending on knowledge of physical processes. In the geosciences, the support vector machines (SVM) are frequently employed to address nonlinear issues. Xue & Forman, (2015) reveals that SVM is more sensitive than the neural network in estimating snow parameters. It has been found that the results based on the SVM algorithm have better accuracy no matter in deep or shallow snow cover, forest coverage area, snow accumulation and melting period. Xiao et al., (2018b) used the support vector regression (SVR) algorithm to establish a snow depth retrieval model based on different vegetation types and different snow periods, showing better accuracy, and reducing "snow saturation effect". Machine learning and deep learning technology can describe that the BTD and snow parameter correlation are nonlinear and overcome the limitations of a linear algorithm in different areas (Liang et al., 2015; Wu et al., 2019). Although the machine learning technologiy has shown a lot of usefulness in remote sensing field and high accuracy, there is no detailed snow physical model involved in the retrieval process (SUN et al., 2015) , thus the interpretability of the results is poor.

The model of retrieving snow depth from microwave data has developed from simple linear regression to non-linear models considering complex meteorological and geographical factors. However, the snow depth with spatial resolution from 10 km to 25 km is not suitable for arid and semi-arid alpine region where the vertical drop is extremely significant. In practical application, snow depth mapping with higher spatial resolution is more useful for regional snow disaster evaluation and hydrological model establishment. Recent studies have demonstrated that higher snow depth mapping can be developed based on high-resolution geographic and meteorological data, together with downscaling microwave data. Snow depth retrieval accuracy was considerably increased by Wang when he created a multifactor power snow depth downscaling model. MOD10A1 fSCA data (500 m) were downscaled for better resolution (30 m) spatially distributed binary SCA detection, Walters et al., (2014) explains and analysis a linear machine model. Downscaled AMSRE SWE dataset were created using MODIS Terra-Aqua data (Mhawej et al., 2014). For the least vegetated areas like Northern Xinjiang (NX) with complex topography and violent vertical variation, high-resolution snow depth mapping can more accurately describe the formation up and ablation of snow in the region and provide precise input parameters for hydrological process and snow disaster early warning.

Support Vector Regression (SVR)

The generalisation classification relation issues, the regression problem has the model returning a continuous-valued output rather than an output from a limited collection. In other words, a multivariate continuous-valued function is estimated via a regression model.

In order to tackle dual class classification issues, SVMs define those issues by convex optimization challenges. Finding the largest margin between the hyperplane and accurately classifying the most training points is the goal of the optimization issue. This ideal hyperplane is represented by SVMs using support vectors. The SVM's sparse solution and strong generalisation make it amenable to adjustment to regression issues. By inserting the "tube," a -insensitive zone surrounding the function, SVM generalisation to SVR is made possible. By first creating a convex-insensitive loss function to be lowered and identifying the flattest tube that conveys the necessary quantity of information, SVR is explicitly described as an optimization problem (Jap et al., 2015; Xiao et al., 2018b). Consequently, utilising the loss function and the tube's geometrical propertie, a multi-objective function is created. The convex optimization is then done using the proper numerical optimization procedures, It has a special remedy. The hyperplane is represented by support vectors, which are training samples that are beyond the tube's boundaries. The training and test data are thought to be independent and identically distributed (iid) in a supervised learning context since they come from the same fixed but unknowable probability distribution function. Similar to SVM, the most significant feature that affect the tube's form in SVR are the support vectors (Xiao et al., 2018b).

The usage of SVM methodology has the following benefits: it can be used for both classification and regression; It translates the given parameters to a high-dimensional feature space and has a model parameters that makes it easier to prevent overfitting that allows for the engineering of the kernel function to create expert knowledge about a problem; and, The algorithm is most significantly described as a problem of optimization with no local minima (unlike neural); Below, we present a brief description of our decision about the type of the SVR framework's kind of regression and kernel(Jap et al., 2015; Vapnik, 1998; Xiao et al., 2018b).

The goal is to discover a function $f(x) = \langle w, x\rangle + b,\ w \in \chi,\ b \in R$ that has a maximum deviation from the real measured objectives yi for all the training data while also being as flat as feasible given a set of training data $\{(x_1, y_1), (x_2, y_2), \ldots, (x_n, y_n)\} \subset \chi \in R$ (Jap et al., 2015).

We can formulate the issue of optimization of convex for a linear function as the Euclidean norm's minimization, but, in order to ensure that infeasible constraints are taken into account, we must also introduce slack variables ξ_i, ξ_i^*:

$$Minimize\colon \frac{1}{2}\left||w|\right|^2 \sum_{i=1}^{n}(\xi_i + \xi_i^*) \tag{22}$$

$$\text{subject to: } y_i - (\omega, x_i) - b \leq \varepsilon + \xi_i^*$$
$$(\omega, x_i) + b - y_i \leq \varepsilon + \xi_i^*$$
$$\xi_i, \xi_i^* \geq 0$$

where the value of the constant C>0 controls the trade-off between f's flatness and the tolerance limit for deviations greater than. ν -SVR developed by Xiao et al., (2018b) replaced Vapnik's -SVRwhere is a variable which value is balanced versus complexity and high and slack variables rather than being defined a priority using the constant ν∈[0,1].

When SVMs extends, one must first formulate the objective function and constraints using Lagrange functions. After optimising the equation and satisfying every constraint, we arrive at the so-called SV expansion, which is as follows:

$$f(x) = \sum_{i=1}^{n}(a_i - a_i^*)(x_i, x) + b \tag{23}$$

where cases with i>0 are support vectors and is fully specified as a linear mixture of the training patterns.

The third stage of the SVR modification process deals with the modelled nonlinear processes. Using a nonlinear mapping, the input vectors can be translated into a high-dimensional feature space, and the optimization issue can then be solved, and it can then be solved in that feature space for a minimal computing cost. We generate the nonlinear regression functions of the following kind using an appropriate, nonlinear function (referred to as the kernel):

$$f(x) = \sum_{i=1}^{n}(a_i - a_i^*).\,\kappa(x_i, x) + b \tag{24}$$

There are two basic types of kernels: one that samples from close regions influence kernel values, and other which assume that samples from any region are capable of affecting kernel values. spread widely apart still have an impact on the kernel value.

Random Forest Regressor (RFR)

The proportion of unique variables in spectral datasets is usually much higher than that in the physical measurements they are compared to. This is necessary since general linear models can't accurately describe response variables due to the large number of interrelated explanatory factors (thin spectral bands and VIs) (Mei et al., 2019) . Machine learning techniques such as RF use several decision trees as their primary classifiers (Belgiu & Drăgu, 2016; Breiman, 2001; Houborg & McCabe, 2018).

The RF approach has shown to deliver a fair level of accuracy as compared to other machine learning algorithms, despite the fact that there are several machine learning algorithms that could be applied (Abdel-Rahman et al., 2014; Houborg & McCabe, 2018; Sonobe et al., 2018). The bootstrapping technique reduces the prediction error by simulating the random select the sample from the entire dataset needed to create decision trees (Belgiu & Drăgu, 2016) . The approach is quite quick when numerous deep decision trees are grown simultaneously using parallel computing. The RF machine learning method also offers a simple

mechanism for choosing features and cascading variable priority. Since there aren't many assumptions associated with RF, setting up data and parameterizing models isn't as difficult.
It is very important to comprehend decision trees to comprehend how the RF operates. Statistics models that use decision trees to predict a response or target variable are used in supervised prediction problems. They are determined by a given number of variables which are self-explanatory (also referred to as input predictors or features). The tree-like organizational presentation of the prediction model is where decision trees get their name. The tree is analysed top to bottom, beginning at the beginning at the root (root node), continuing via hidden layers, then coming to an end when a terminal node (also known as a leaf) is reached. Each regression tree grows from the roots to the leaves when a particular set of requirements and limitations are met (Breiman, 2001) . Decision points are the internal nodes. From the bigger training dataset, a set of resamples (randomly chosen subset of data) are taken as the initial starting point for the construction of a single decision tree. Because of the increased diversity in the forest, the overall prediction is stronger as a result. Each bootstrap sample is fitted using a regression tree in such a way that part of randomly taken input feature is taken into account for binary partitioning every node (At each node, diividing rule is used for splitting). When splitting data using decision trees, the Gini Index is frequently utilised (It is decided to use the input prediction with the least Gini Index) (Mei et al., 2019):

$$I_G(t_{X_{xi}}) = 1 - \sum_{j-1}^{m} f(t_{X_{xi}}, j)^2 \quad (25)$$

$f(t_{X_{xi}}, j)$. is the percentage of samples that are part of leaf j at node t and have the value xi, where xi is a measurement of the sample proportion (Houborg & McCabe, 2018) .The root node of each decision tree sprouts branches (intermediate nodes), which split off, and finally terminal nodes (leaves). For all of the observations, only one predictor variable is examined at a time by each node in the tree. If the condition is satisfied, a binary decision is made, and another regression model is chosen for the next node. As a result, the decision tree develops to its terminal nodes (leaves), each of which is composed of a response. At the start of the RF implementation, two inputs must be optimised. One has to be the RF implementation; two inputs must be optimised. The first is the minimal quantity of regression trees (ntree) necessary for deep network. The second is "number of leaves," which is equivalent to the tree's terminal nodes. A tree with an excessive amount of leaves will grow shallowly, halting after only a few splits, which could lead to subpar prediction accuracy. On the other side, fewer leaves (deep trees) may lead to overfitting(Díaz-Uriarte & Alvarez de Andrés, 2006). A total of all the trees is used to calculate predictive power.

A separate model is used to build each tree in the random forest. The samples utilised for bootstrapping are known as "in bag" samples, whereas the samples that were not used to build the model are known as "out of bag" (OOB) samples. In other words, An OOB error method is used in the RF to quantify the prediction error, and independent cross-validation also isn't necessarily required. This theory gives random forest the ability to evaluate models without using a distinct set of data. Usually, two thirds of the samples are utilised for training the models, while the remaining one third is used as oob samples (Breiman, 2001) Since oob samples are not used to construct the trees, oob estimations give RF reliable measures of model accuracy. Thus, the overall model accuracy is obtained by averaging oob-based predictions across all trees. In this investigation, the RMSE was used to test the model results (Breiman, 2001).

3.7. Chapter Summary

In this chapter, the physical and electromagnetic properties of snow have been discussed with in detail with visible and microwave remote sensing of snow. The state-of-the-art models concerning SD and SWE estimation have been succinctly described along with their advantages and drawbacks along with other sections like climatological and topographical effects on snow properties, fusion of optical and microwave remote sensing data, downscaling and machine learning for snow properties. Moreover, several relevant literatures are cited for referring the reader to more advanced in-depth concepts that have been summarised in this chapter. Additionally, the symbolises or notations used in the equations and figures have been adopted from the existing literatures and in some cases, have been modified accordingly to remove any ambiguity. Starting from the next chapter, the thesis specific discussions are provided.

4. MATERIALS

4.1. Study Area

The North-Western Himalayas (NWH), which are comprised of the river basins of the Jhelum, Sutlej, Chenab, Ravi, and Beas in the states of Jammu & Kashmir and Himachal Pradesh, are bounded by longitudes 72°E to 80°E and latitudes 30°N to 37°N. The northern Karakoram Himalaya is roughly 8000 metres high, whereas the Siwalik Himalaya in the south is only a few hundred metres high. Westerly disturbances affect precipitation in the NWH between October and May, whereas the southwest monsoon is in charge between July and September. The region's climates vary significantly from one area to another (M. R. Bhutiyani et al., 2010) . The region's far east, which is thinly forested and near to Tibet, experiences little to no rainfall in the form of rain or snow and has a cold, dry environment. The west has a lot of rivers and valleys, a forest cover that ranges from evergreen to semi-evergreen, and very moist weather with a lot of precipitation (snow and rain) (M. R. Bhutiyani et al., 2010) The quantity of snowfall experienced by various ranges in the NWH varies depending on altitude and ranges from roughly 100 to >1600 cm. The Pir Panjal Range receives the most annual winter snowfall, and as one moves farther north toward the Great Himalaya, Zanskar, Ladakh, and Karakoram mountains, less snow is received. In higher altitudes, the majority of the year is spent with temperatures below zero, and the majority of the wintertime precipitation takes the form of snow (M. Bhutiyani, 1992) The Siwalik and Pir Panjal Ranges experience the highest monsoon precipitation, and the Great Himalaya, Zanskar, Ladakh, and Karakoram Ranges experience the lowest (Rakhecha et al., 1983).

The Tibetan Plateau, Himalaya, Hindu Kush, and Karakoram are mountain ranges that are home to the upper Indus basin (UIB). Seven separate Indus tributaries, totalling over 425.000 km², flow from the UIB (Fig 4.1) (Lutz et al., 2016). The UIB has a mean elevation of 3750 metres above sea level and an altitudinal range of about 8500 metres. The UIB is a transboundary river basin in a geopolitically complicated area, encompassing portions of Afghanistan, Pakistan, India, and China. With about 22.000 km² of glacier surface area, it is among the planet's most glaciated regions (Lund et al., 2020).

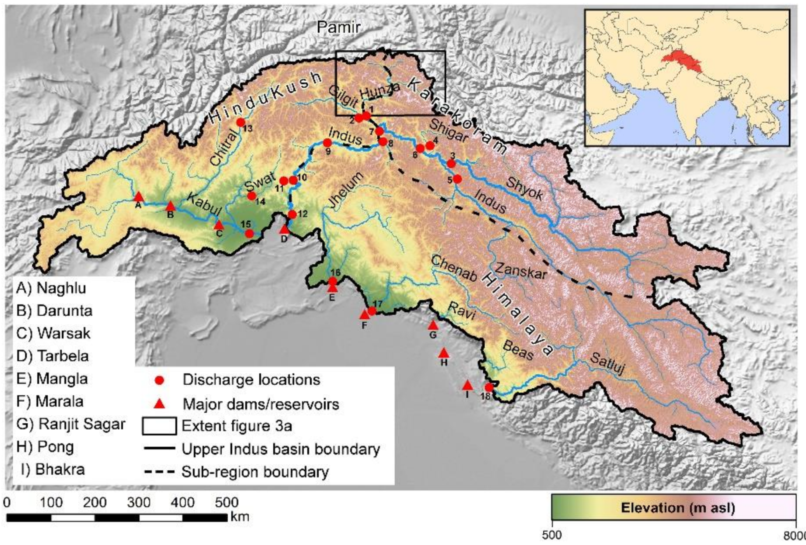

Figure 4-1: Upper Indus Basin (Lutz, 2016)

The UIB's complicated climate is the consequence of a complex interaction between the terrain, westerlies, and monsoon circulation (Bajracharya & Shrestha, 2011; Maussion et al., 2014; Williams, 2013). At several sizes, ranging from a synoptic scale of several hundred kilometres to an orographic meso-scale of fewer than thirty kilometres, the interaction between topography and precipitation can be seen (Lutz et al., 2016). The Himalayan region is where the monsoon has the most impact arc, but it diminishes in the north-western direction where mid-latitude westerlies become more significant, such as around the intersection of the Karakoram, Pamir, and Hindu-Kush mountain ranges (Fig 4.1) (Lund et al., 2020; Lutz et al., 2016). When low-pressure systems approach the western edge of the larger Himalaya in winter, precipitation from the westerlies is at its maximum. The increased tropospheric extent of the westerly wind may be the reason why this source of moisture reaches higher elevations than the summer monsoon (Bajracharya & Shrestha, 2011; Maussion et al., 2014; Williams, 2013). Indus River basin further consists of two major regions like Upper Beas basin and the upper Sutlej basin can be taken for our study.

4.1.1. Upper Beas Basin

In addition to being a tributary of the Indus River system, the Beas River feeds the River Sutlej. At a height of 3900 metres (m.a.s.l.), Beas Kund, a little ice body on the eastern side of the Rohtang Pass in the Himalayas, is where the Beas River begins It flows almost north-south till Larji, In order to reach Pandoh in Himachal Pradesh, turn west and continue in the same route. A diversion dam has been constructed at Pandoh (Rani & Sreekesh, 2019). The main river's flow and the flow of its tributaries are unaffected by human-made activity above the Pandoh Dam. Upstream of Pandoh Dam, the Beas basin's catchment area is 5278 km², of which 780 km² are permanently covered in snow and ice. The research area's elevation ranges from roughly 900 m to more than 5000 m above mean sea level (Rani & Sreekesh, 2019). Permanent snowfields and glaciers are present in the basin's upper portion. A few of the main tributaries that reach the Beas River upstream of Pandoh Dam are the Parvati River at Bhuntar, the Tirthan and Sainj rivers close to Larji, the Sabari Nala close to Kulu, and the Bakhli Khad close to Pandoh Dam. (Fig. 4.1) displays the river system's drainage map together with rain gauge stations(Rani & Sreekesh, 2019). All of these rivers have a constant flow; however, it fluctuates greatly from month to month. Power generation, irrigation, tourism, and other industries have very good potential along the Beas River and its tributaries.

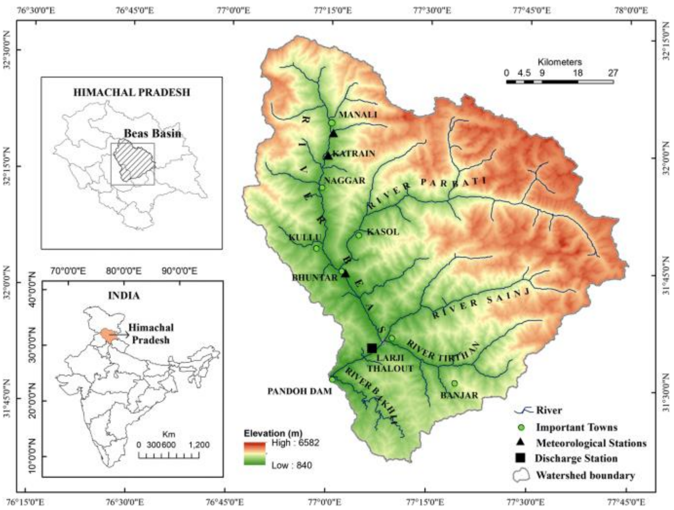

Figure 4-2: Part of Indus River basin regions focussed with ground observation data, in the right: Upper Beas Basin (Rani, 2019); and, in left: Sutlej Basin (Chauhan Rohit, 2016)

The Beas River originates in Rohtang Pass, which is located 51 kilometres north of Manali at a height of 4350 metres. The Beas Kund glacier serves as the primary water supply for the Beas up to Manali. A wide network of hydro - meteorological stations in the study region provided support for the project and ground truth data gathering (Thakur et al., 2013). A cool, dry climate characterizes the study area's three major seasons: cold from October through February, hot from March through June, and rainy from July through September. Since most of the mountain roads are blocked, the region is mostly cut off from the lowest part in December to February, when snowfall typically accumulates at elevations above 2000 metres. The region's wettest months are August and September (Thakur et al., 2017). The rainiest months are July and August, and the driest months are October and January. The average daily temperature varies from between 5 and 0 degrees Celsius in January to 20 °C to 30 °C in June (Thakur et al., 2012) The watershed's major snowmelt season lasts from the end of April to the second week Of September, with the most critical melting period being from April to June and the peak season from July to September. (M. Kumar et al., 2013; V. Kumar et al., 2007)

4.1.2. Upper Sutlej Basin

This study focused on the Sutlej River basin, located in the western Himalayan region upstream of the Bhakra Reservoir (Figure 4.3) (Chauhan et al., 2016). The Mansarover and Rakastal lakes on the Tibetan plateau, which are over 4500 metres above sea level, are the source of the Sutlej River, which is a branch of the Indus River system. Only rain is experienced in the basin's lowest portion (P. Singh & Bengtsson, 2004). The topographical situation and accessibility of plentiful water offer this river a significant hydropower generating potential. There are numerous hydropower projects in place, and more are planned for this river (Chauhan et al., 2016).

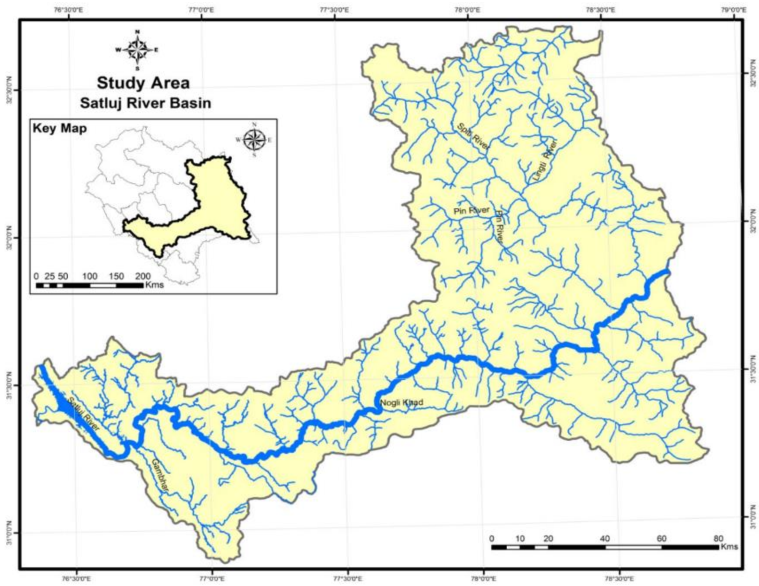

Figure 4-3: Sutlej Basin (Chauhan et al., 2016)

At the foot of the Himalayas, on this river, the Bhakra Dam sits, the oldest dam in India. This dam is regarded as a blessing for irrigation and electricity generation in north India. The study basin covers around 22, 275 km² of land (P. Singh & Bengtsson, 2004). The basin's altitude ranges greatly from 500 to 7000 metres. Figure 4.3 illustrates the area-elevation curve for the study basin. It reveals that only a very minor portion of the basin is above 6000 m, with the majority of the basin's area falling between 3600 and 5400 m. As a result of significant seasonal temperature fluctuations and the basin's wide range of elevations, the snowline dips to about 2000 meters in winter and recedes to about 5000 meters in summer. Wintertime snowfall covers the basin region to a degree of about 65% (P. Singh & Jain, 2002) Chauhan et al., (2016) reported that about11% area of the basin is covered by glaciers. Using remote sensing data, A. Kulkarni, (1999) conducted a glacier inventory of the Sutlej Basin and discovered that 2700 km², or around 12 percent of the basin, is covered with glaciers and permanent snowfields. Diverse climate trends can be seen in this river basin. During the winter, much of the precipitation turns to snow, and the western weather disturbance primarily dump it in the upper and central parts of the basin. The bigger Himalayas, which are mostly where the basin is located, frequently experience snowfall. The rainstorms have little effect in the wider Himalayan range, which receives 200 mm of rain annually on average (P. Singh & Bengtsson, 2004). The middle and outer Himalayan ranges, where a portion of the Sutlej River basin is located, receive 700 and 1300 mm of rainfall annually, respectively (P. Singh & Bengtsson, 2004). This demonstrates that the lower portion of the basin receives much of the rainfall. For the whole basin, accurate data on snowfall and its distribution is not available. This seasonal snowpack, which was created during the winter, begins to melt around March and depending on the climatic conditions over the basin, either completely or partially disappears throughout the upcoming summer. In the upper portion of the basin, snowmelt is the main factor causing runoff, but rainfall is the main factor in the bottom section of the basin. Snowmelt and rain both contribute to the basin's middle and upper regions. While snowmelt contributes more to streamflow as altitude rises within the basin, rain's contribution decreases. Above 3000 m, snowmelt-induced runoff dominates runoff, but above (P. Singh & Jain, 2002).

4.1.3. Field Visit

The extensive work on the field has been done in February 19-28, 2022, in the Kothi and Solang Valley areas where a snow fork (fork-shaped) radio wave sensor has been created in order to assess the density and moisture profiles of a snowfall simultaneously. The snow fork's foundation is the measuring of snow's real and imaginary dielectric characteristics at frequencies about 1 GHz. The measurement is non-destructive because of the open construction of the resonator. Automatic measurement findings are guaranteed by automatic measuring equipment and can be noted on the field (Sihvola & Tiuri, 1986). Nevertheless, in a few of the more practical locations, including the Dhundi base station and the Automatic Weather Station (AWS) of Sainj, Marhi and Kothi, the data has been collected.

Figure 4-4: Beas watershed with high (left) and low (right) snow cover

Figure 4-5:Taking snow fork reading near Kothi area (top left), AWS site, Sainj (Top right), Snow fork reading in Solang valley region, Manali (Bottom left), AWS data download (Bottom right)

4.2. Spatial data products and description

For this research work, varieties of dataset have been used. Passive microwave data, SAR data and different Optical data products have been used along with topographical and climatological datasets. All datasets have been processed for year 2016-2017 on availability of pixel values on each particular date. These datasets have been pre-processed stacked together to work on it as a time series data

4.2.1. High Mountain Asia UCLA Daily Snow Reanalysis, Version 1

Asia's High Mountains Incorporating fractional snow-covered area (fSCA) measurements from the Landsat and Moderate Resolution Imaging Spectroradiometer (MODIS) platforms over the combined Landsat-MODIS record between Water Year (WY) 2000 and 2017, the UCLA Daily Snow Reanalysis, Version 1 (HMASR) is a snow reanalysis over High Mountain Asia (HMASR) (Margulis et al., 2019). The data collection contains posterior forcings and daily estimations of the snowpack (SD, snow albedo, SWE, and fSCA). Key posterior snow estimations (SWE, fSCA, and SD) are provided ensemble statistics (e.g. mean, median, and spread), whereas other states and flow variables are given ensemble median values. As metrics of the data integrity and to provide some usage advice for this dataset, classification masks as well as a quasi snow/ice mask are used.

SWE, fSCA, and SD have the same dimensions (225 x 225 x 5 x 366) as latitude by longitude by quantity, ensemble statistics, or water year day. Ensemble mean, ensemble standard deviation, ensemble median, 25th percentile, and 75th percentile information is presented in that order. The snow albedo and posterior forcing variables' dimensions (225 x 225 x 366) match to latitude, longitude, and day. Either latitude by longitude (non-seasonal snow/ice mask) or latitude by longitude by water year (classification mask) match to the masks' size (225 x 225 x 18).

4.2.2. Sentinel-1 SAR

Sentinel-1 offers exceptionally precise pointing information and accurate orbit determination, which greatly improves the SAR outputs' geolocation accuracy. At a height of 693 km, Sentinel-1 is currently in a relatively close sun-synchronous orbit. (Miranda & Meadows, 2015; Torres et al., 2012). A 180-degree shift in orbital phasing would make Sentinel-1B's baseline orbit the same as Sentinel-1A's. Six-day exact repeat pass observations will be possible with the two-satellite constellation. Two to three days will pass between repeat coverage in the mid-latitudes using adjacent swaths. (Nagler et al., 2016).

The S1 SAR works at a 5.4 GHz centre frequency. This study's IW mode data across North India were collected in dual polarisation (VV and VH). In comparison to the standard ScanSAR mode, with a swath width of 250 km and a nominal ground resolution of 5 m 20 m for single look data, the IW mode functions like TOPS (Terrain Observation with Progressive Scans in azimuth) (Torres et al., 2012)In IW mode, each image swath is divided into three smaller swaths. Along the railway, individual swaths are separated into slices that are each around 350 km long. When corner reflector and transponder signals are evaluated, they produce spatial resolutions of 22 m in azimuth and 2.84 m, 3.10 m, and 3.50 m in LOS for sub-swath IW1, IW2, and IW3, respectively, for IW mode SLC data (Miranda & Meadows, 2015).

The SSMI radiometer, which would be deployed on top of the Defense Meteorological Satellite Program (DMSP) class spacecraft, would monitor snow globally. The device does not depend on clouds for its operation, and daily observations are accessible. The SSM/I is a microwave radiometric system with seven channels and four frequencies (19, 22, 37, and 85 GHz) (Tedesco & Jeyaratnam, 2016). Except for the 22 GHz channel, which is fixed at V polarisation, all channels operate in dual vertical (V) and horizontal (H) directions. According to (Armstrong & Brodzik, 2002; C. te Chen et al., 2001; Foster et al., 2005), the footprint varies from 6943 km^2 at 19 GHz to 12.512.5 km^2 at 85 GHz.

4.2.3. Moderate Resolution Imaging Spectroradiometer

The Terra and Aqua satellites' Moderate Resolution Imaging Spectroradiometer (MODIS), formerly known as EOS AM-1 and EOS PM-1, is an essential instrument on board. Aqua crosses the equator from The Terra and Aqua satellites' Moderate Resolution Imaging Spectroradiometer (MODIS), formerly known as EOS AM-1 and EOS PM-1, is an essential instrument on board Terra MODIS and Aqua MODIS observe the whole surface of the Earth every one to two days, recording data in 36 wavelength bands (MODIS Technical Specifications). Land, ocean, and lower atmosphere dynamics and processes will be better understood with these data. A crucial part of MODIS is being played in the creation of validated, global, interactive

4.2.3.1. MODIS Snow Cover Area

SCA, fSCA snow albedo, and quality assessment (QA) data are all included in the MODIS Snow Cover Daily Global 500m Terra and Aqua package. Based on a snow mapping technique that uses NDSI and other criteria tests, snow cover data are generated.

4.2.3.2. MODIS Normalized Difference of Snow Index

Based on snow's generally increased reflectance in the visible section of the spectrum compared to the mid-IR, the Normalized Difference Snow Index is used to identify snow. NDSI has a range of -1.0 to 1.0 and is calculated using the Green and Mid-IR bands. The surface reflectance composites from MODIS Terra and Aqua were used to create this product.

4.2.3.3. MODIS Normalized Difference of Vegetation Index

The NDVI has a value between -1.0 and 1.0 and is calculated using the Near-IR and Red bands of each scene. The surface reflectance composites from MODIS Terra and Aqua were used to create this product.

4.2.3.4. MODIS Land Surface Temperature

In a grid of 1200 x 1220 kilometres, the MODIS delivers emissivity and land surface temperature (LST) readings every day. The MOD11 L2 swath product yields the temperature value. Some pixels may have several observations above 30 degrees latitude where the requirements for a clear sky are met. The pixel value is the average of all qualifying observations when this happens. The daytime and nighttime surface temp bands and related quality indicator layers are also given, along with the MODIS band 31 and 32 and six observations layers.

4.2.4. Shuttle Radar Topography Mission – Digital Elevation Model

A worldwide research project called the Shuttle Radar Topography Mission produced digital elevation models on a nearly global scale (Farr et al., 2007). This study made use of the SRTM V3 product (SRTM Plus), which is offered by NASA JPL and has a resolution of 1 arc-second (about 30m).

4.2.5. Climate Hazards Group InfraRed Precipitation with Station Daily

Climate Hazards Group InfraRed Precipitation with Station data (CHIRPS), a dataset of quasi-global rainfall spanning more than 30 years, is accessible. in order to track seasonal droughts and analyse trends, CHIRPS creates gridded rainfall time series using in-situ station data and 0.05° resolution satellite images.

4.3. Softwares and Tools

In this research, GIS tools like Google Earth Engine, SNAP and QGIS has been used for data collection, data extraction, data pre-processing and data visualization. Python and programming language has been used to write code for Machine Learning and Deep Learning algorithms along with GEE API has been used a library in python for data management for model development. CRIB- ITC Geospatial Computing Platform played vital role in model development for our use case as dataset was very large before pre-processing. It provided large space to download and store datasets of different sensors along with high computational power for model developments.

4.4. Chapter Summary

This chapter consists of the discussion about Study area and field visits than happened during research phase. Followed by all the datasets than have been used in this thesis research work. In the end, all software and tools has been mentioned which have been used in this research work at different stages like, data extraction, data pre-processing, data management, model training and testing and data visualization

5. RESEARCH METHODOLOGY

5.1. Research Design

The methodological framework used to produce the SD and SWE results using machine learning algorithms is covered in this chapter. A flowchart that highlights the key process steps is displayed in Figure 5-1 in order to quickly summarise the whole workflow --

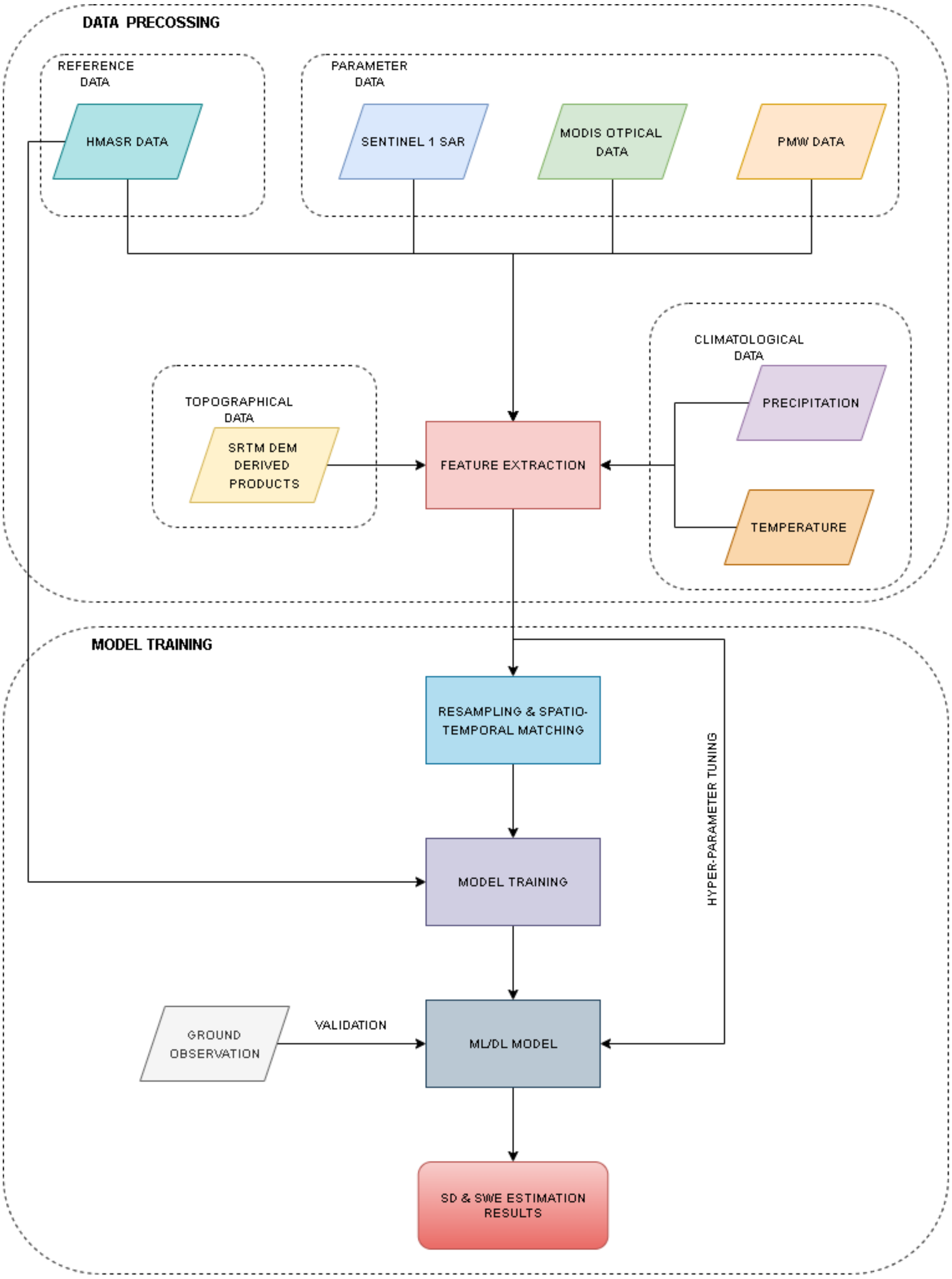

Figure 5-1: Methodological Flowchart

5.2. Data pre-processing

For two different sub basins, all dataset has been clipped to upper Beas basin and upper Sutlej basin with a projection of (EPSG:4326). Each dataset consists multiple feature which existed already as a band or derived from the different band combination or some different processing. Water year October 2016 to September has been taken for the research according to availability of all data dataset with respect to our reference data which is HMASR. Different sensors have been pre-processing like active microwave (SAR), passive microwave (SSMI) and Optical sensor (MODIS) along with some topographical and climatological data like Land Cover, DEM, temperature, and precipitation. Both direct and indirect features have been collected from these datasets. Reference data of this research work, HMASR has been processed separately as our aim was to spatio-temporal match all other dataset with our reference dataset.

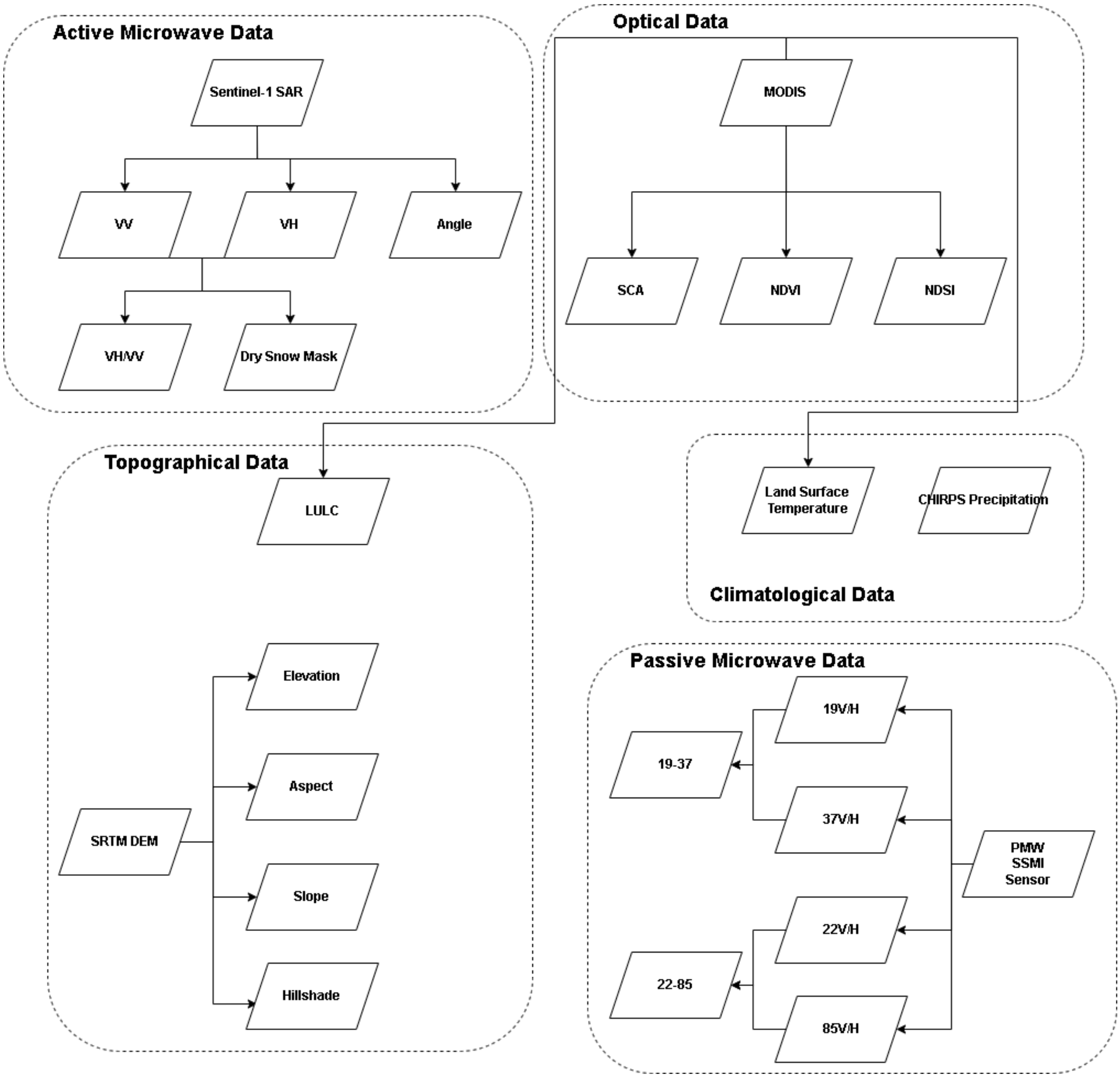

Figure 5-2: Data Pre-processing Block Diagram

5.2.1. Sentinel-1 SAR

Sentinel-1 SAR GRD (log scaled) data has been collected for all dates that were available in water year October 20176 to September 2017. All features that can be collected from Sentinel-1 GRD was VV band, VH band, ratio of VH and VV and, angle values (X. Zhong et al., 2018). Different SAR modalities like InSAR and PolSAR using Sentinel-1 SLC level 1 data has not been used to long processing data for a whole water year. It was less feasible to generate so many products from different modalities and later incorporate in model. All the dataset has been stacked to create a data cube later to put it into model.

A dry and wet snow classification has also been done for each SAR images to put into model (Baghdadi et al., 1997; Snapir et al., 2019). All the calculations and data collections has been done on GEE and later incorporated with python for model development.

5.2.2. MODIS

Both MODIS Aqua and Terra product has been to get optical data like snow cover area (SCA), Normalized Difference of Snow Index (NDSI) and Normalized Difference of Vegetation Index (NDVI). For SCA, maximum value of the pixel has been taken for each day from composite of Aqua and Terra products to get maximum snow cover extent and to fill cloud gapped values (Kim, 2018). For NDSI and NDVI, mean of Aqua and Terra product has been taken for each day in water year to create composites. All the dataset has been stacked to create a data cube later to put it into model. All the calculations and data collections has been done on GEE and later incorporated with python for model development.

5.2.3. Passive Microwave (SSMI)

PMW sensor SSMI consists of four temperature brightness (TB) bands at different frequencies which are 19 GHz, 22 GHz, 37 GHz, and 85 GHz (Che et al., 2008b, 2008a; C. te Chen et al., 2001; Foster et al., 2005; Josberger & Mognard, 2002; Margot Flemming, 2020; P. R. Singh & Gan, 2000; SUN et al., 2015; Walker & Goodison, 1993; Xiao et al., 2018b). Each these bands are available for both ascending and descending pass. As ascending pass was not coming in our study area, we skipped that. Now for each pass, two polarities are available which are Vertical and Horizontal. Both polarities have been used in this study to see how it correlated with SD and SWE. TB and difference of TB values has linear relationship with SD and SWE so difference of 19 and 37 GHz has been extracted as feature to put into model, but 22 GHz came as irrelevant so decision of dropping that band has been taken. All the dataset has been stacked to create a data cube later to put it into model. All the calculations and data collections has been done using python for model development.

5.2.4. SRTM DEM

SRTM DEM at 1src sec spatial resolution has been used for this research product which has been later resampled for specific use case (Farr et al., 2007; Hultstrand et al., 2022; Jost et al., 2007). Many products have been generated using this DEM like aspect, slope, hillshade and elevation was already there. All the dataset has been stacked to create a data cube later to put it into model. All the calculations and data collections has been done on GEE and later incorporated with python for model development.

5.2.5. Other topographical and climatological data

Land cover use was one of the major topographical data that has been used in this research as SD and SWE varies a lot in different terrains. Along with this data, climatological data like Land Surface Temperature (LST) which was daily composite of MODIS Aqua and Terra sensors and precipitation data was got from CHIRPS product. All the dataset has been stacked to create a data cube later to put it into model. All the calculations and data collections has been done on GEE and later incorporated with python for model development.

5.2.6. HMASR data

HMASR data consists of many products like fSCA, SD, SWE, Snow Albedo etc for each day of water year October 2016 to September 2017 (M. Liu et al., 2020). For SD and SWE different ensemble statistics are available at resolution 500m. Out of all ensemble's statistical values, ensemble mean, and ensemble median has been taken to give as reference data in model. Six different tiles have been mosaiced to cover whole study area and each day stacked as bands for both mean and median ensemble statistical values. Most the processing has been done using SNAP as the file was four-dimensional NETCDF file and mosaicking has been done using QGIS. Other the calculations and data collections has been done on GEE and later incorporated with python for model development.

5.3. Data exploratory Analysis

Data exploration has been done before development of the model to understand dataset in better way and to see what all dataset is going to be useful this research. First, fractional snow cover(fSCA) is most important factor to determine the snow cover area(SCA) in the given study area. SCA has been calculated using MODIS SCA product from GEE which gives SCA map with cloud mask. To reduce the cloud mask in single day, composite of Aqua ad Terra product has been taken. Further, all days of SAR availability has been considered to take only those date of SCA. Then, intersection of SAR and SCA image has been taken for each day of availability. Rest other dataset has bene clipped and resampled to HMASR resolution (500m) and projection (which is EPSG:4326) accordingly.
Datasets having coarser resolution than 500m have been downscaled using bilinear interpolation resampling. A limit of 2000 metres elevation has been put by considering it as an average snowline of the study area to reduce error in the model training. All the spatio-temporal matched images have been stacked as a data cube to do further analysis. All these images read as an array in python and a dataframe has been created to put all these data in the CSV file. Few small sample areas have been taken manually from the study area to avoid large number of dataset and dataframe for that created accordingly. Correlation has been checked for all these dataframe and static parameter like latitude and longitude has been avoided for model training to keep model generic.

5.4. Models Development

For estimation of SD and SWE, two different ML models have been implemented which SVR and RFR with having generic approach of model development as show in Figure 5.3. Each model development description has been mentioned here with having different combination spatial and temporal resolution of multiple sensors as mentioned in the table below:

Table 5-1: Different Combination of input dataset for model testing

Sensor Combination	PMW	SAR	Optical	Resolution
1	Yes	No	Yes	3125m/daily
2	No	Yes	Yes	500m/SAR availability
3	Yes	Yes	No	500m/SAR availability

4	Yes	Yes	Yes	500m/SAR availability
5	No	Yes	Yes	500m/Monthly composite

A generic approach of model creation has been aimed to create generalize the SD and SWE for given study and minimize the random error that comes when change in study area happens. According to Figure 5.3, the data cube of spatiotemporal matched dataset has been used as input dataset with testing optimal combinations of input features and HMASR given as reference data. Hyper-parameter tuning has been done using optimal input features and later validation has been using ground data. All these steps have been discussed in later stages of this chapter.

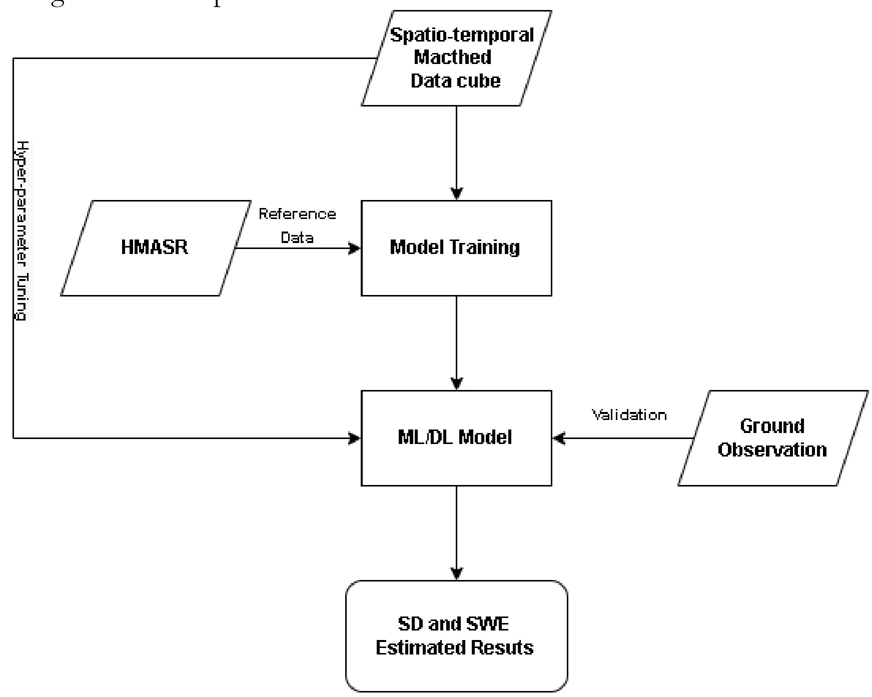

Figure 5-3: Model Development Flowchart

5.4.1. ML Models

For this study, SVR and ANN regression model has been analysed. These three different models have been used because each having its own merit and demerit. Explanation of usage of each regression model has been given below.

5.4.1.1. Support Vector Regression (SVR)

SVR model has been used using '*rbf*' which was apt for our use case. It has been used when the number of predictors is less as it gives poor accuracy when number of predictors are more. Along with this, SGD Boost function has been used to work on larger number of samples of dataset in given study area in order to get better accuracy than normal SVR function. Different combination and samples have been tried in order to get better accuracy in several combination has been tried to obtain minimum error.

As the samples were very large, SGD regressor model has been used using sklearn library of python that too after a Nystroem transformer. Nystroem transformer approximate a kernel map using a subset of the training data (Abdel-Rahman et al., 2014; Jap et al., 2015; Vapnik, 1998; Xiao et al., 2018a). It constructs an approximate feature map for an arbitrary kernel using a subset of the data as basis.

Training samples has been matched non-linearly with reference data that has been produced from HMA has a relationship which has been learned from model training. Using support vectors, a generalized model with less mean absolute errors and mean square has been produced.

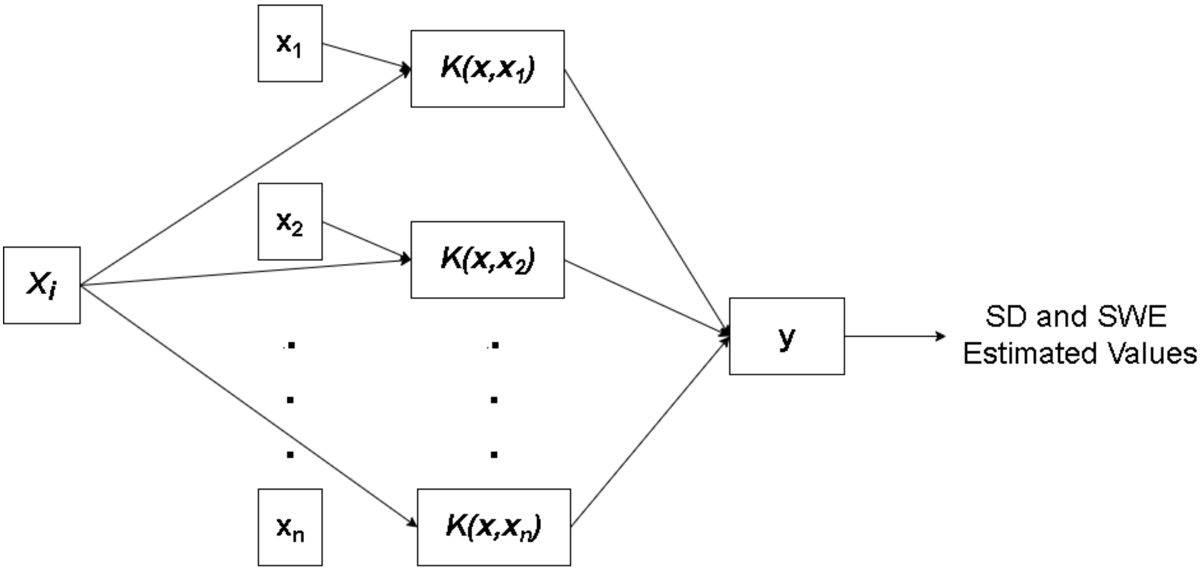

Figure 5-4: SVR Model

5.4.1.2. Random Forest Regressor (RFR)

Another model to check the performance of SVR has been used which was RFR in our case. RFR created bootstrap of samples from different trees. Each tree predicted values and average of predicted values has been taken as an overall prediction of full dataset that was given in the model. Due to the large number of datasets, case of overfitting has been appeared for the RFR model which increase the inaccuracy of the test data which was later provided to the RFR model after training (Belgiu & Drăgu, 2016; Biau & Scornet, 2016; Breiman, 2001; Houborg & McCabe, 2018).

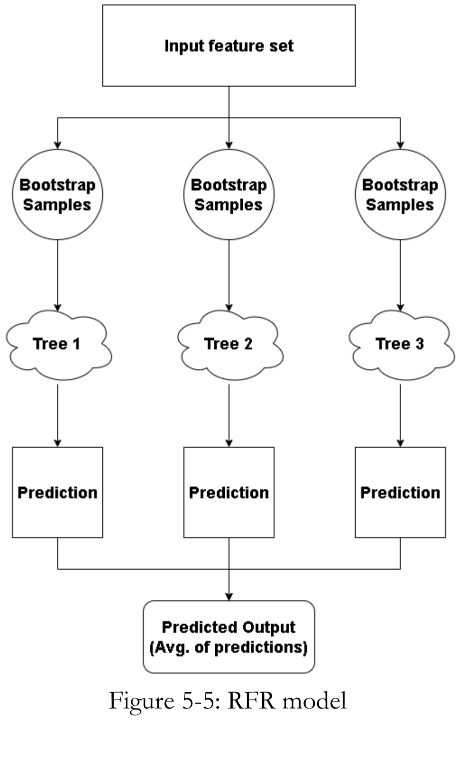

Figure 5-5: RFR model

To overcome the over-fitting issue, a sample dataset has been given by creating sample area from the full study area. This method helped to increase model accuracy but when model ran for full study area, predictions were not up to mark

5.4.2. Hyper-parameter Tuning

The most common method of hyper-parameter tuning in python is 'GridSearchCV' by sklearn library. This function can be used for both SVR and RFR models. Only the difference is there parameters which are different in both models will be different while create the grid of parameters.

SVR

The most important parameter in SVR model is kernel. For this research, two kernels have been considered which are 'poly' and 'rbf' but proceeded with the 'rbf' because of non-linearity aspect of it. As the input number of parameters were a lot, it increases the complexity in the SVR model (Xiao et al., 2018a). Other parameters in SVR models like gamma, regularization C, epsilon, verbose and max_iter have been given into parameter grid search to obtain optimum parameters for the given model.

RFR

Same grid search function has been used for RFR model also with having parameters in param grids like, n_estimators, max_depth, min_samples_split, min_sample_leaf , max_features etc. Some manual parameter tuning has also been done to get optimum accuracy (Yang et al., 2020).

5.4.3. Validation and Accuracy Assessment

As the problem in this thesis is a regression problem, along with r square values, other accuracy metrices like mean absolute error and root mean squared error has been analysed in order to obtain the best accuracy. We have tried to achieve accuracy in which error should be 10 percentage of the mean value. For validation of the model, results have been matched with reference data and with some ground data also. Some zonal statistics has also been done basin wise to check whether results are coming right or not so even in the absence of ground dataset, results can be get verified.

5.5. Chapter Summary

In this chapter, methodology for data pre-processing and model development has been discussed in detail. Along with that, data exploration also has been done to check how to put dataset into model. Hyper parameter tuning process and validation with accuracy assessment processes has been also discussed.
As the problem in this thesis is a regression problem, along with r square values, other accuracy metrices like mean absolute error and root mean squared error has been analysed in order to obtain the best accuracy. We have tried to achieve accuracy in which error should be 10 percentage of the mean value. For validation of the model, results have been matched with reference data and with some ground data also.

6. RESULTS

6.1. Pre-processing results

To extract features from several datasets, pre-processing has been done to put input data in machine learning model in correct manner. Many features have been extracted and pre-processed as per our requirement in the models are like, features from SAR data: co-polarized and cross-polarized bands (VV and VH) with their ratio in log scaled value only (VH/VV), incidence and binary classification of wet and dry also has been created using SAR data. From optical dataset like MODIS, Snow Covered Area (SCA) which gives fractional snow cover (fSCA), NDSI and NDVI values has been extracted. Some climatological and topographical data has also been extracted like Land Surface Temperature and Land Cover, respectively. Using passive microwave, the relevant Temperature Brightness values we got were like 19V GHz, 19HGHz, 37V GHz, 37H GHz, 85V GHz, 85H GHz and the difference of 37V GHz from 19V GHz and 37H GHz from 19H GHz has also been extracted and resampled to use predictors in our model. Some other topographical features like elevation, aspects slope and hill shade has also been extracted using SRTM DEM dataset.

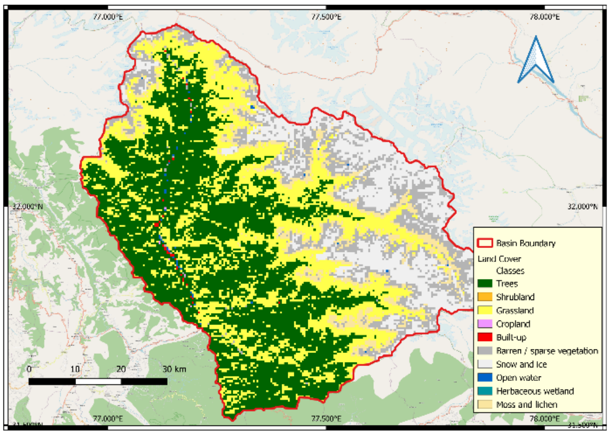

Figure 6-1: Land Cover Classes Map of Beas Basin

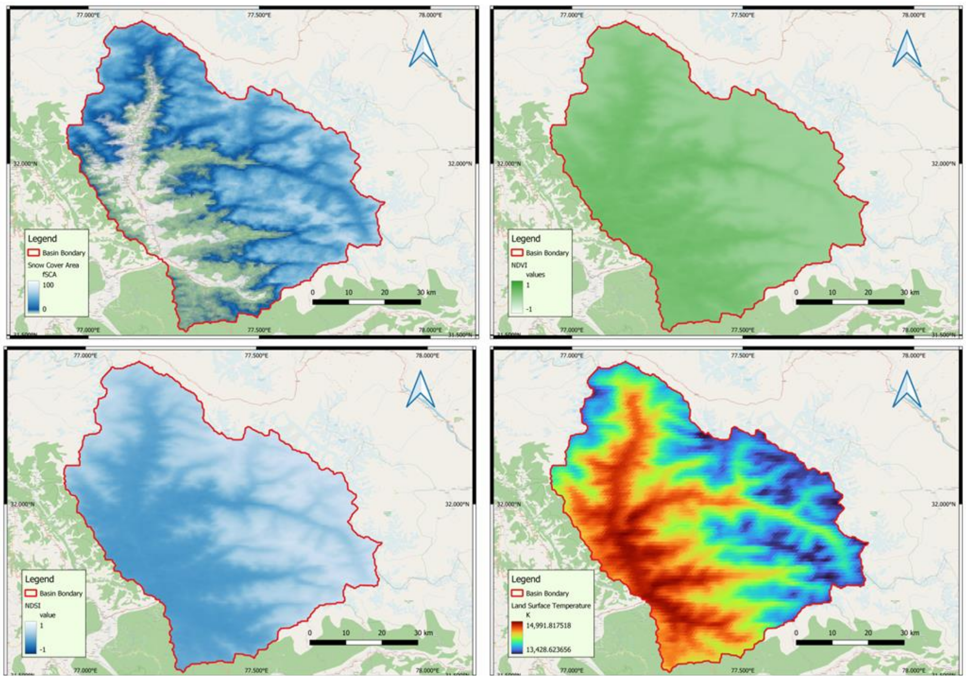

Figure 6-2: MODIS maps of Snow Cover (top right), NDVI (top left), NDSI (bottom left) and LST (bottom right)

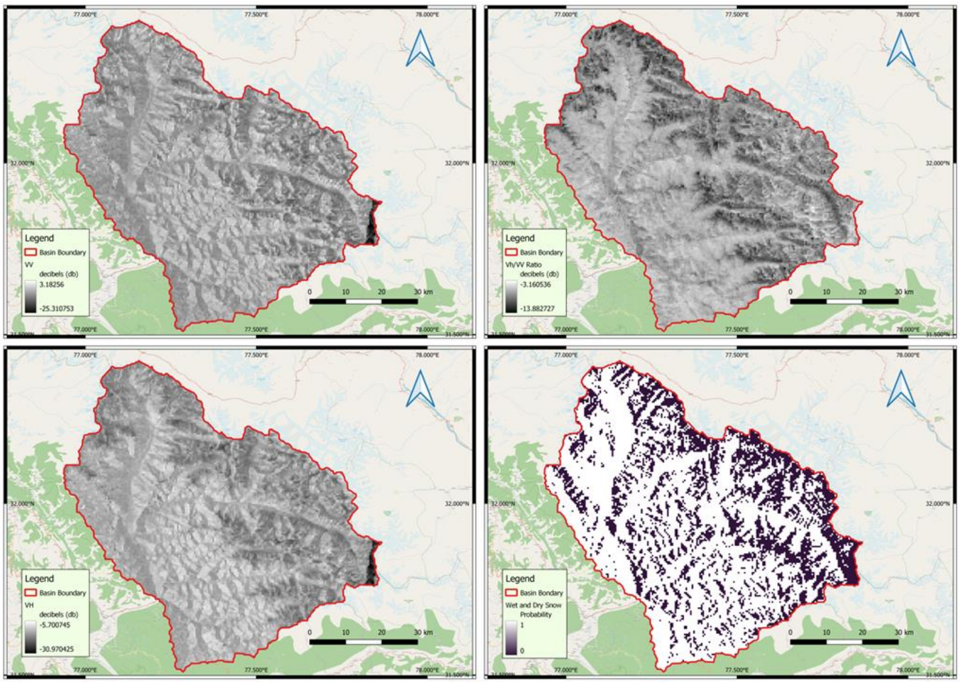

Figure 6-3: Sentinel-1's VV band (top left), VH band (bottom left), VH/VV (top right), wet (0) and dry snow (1) classification(bottom right)

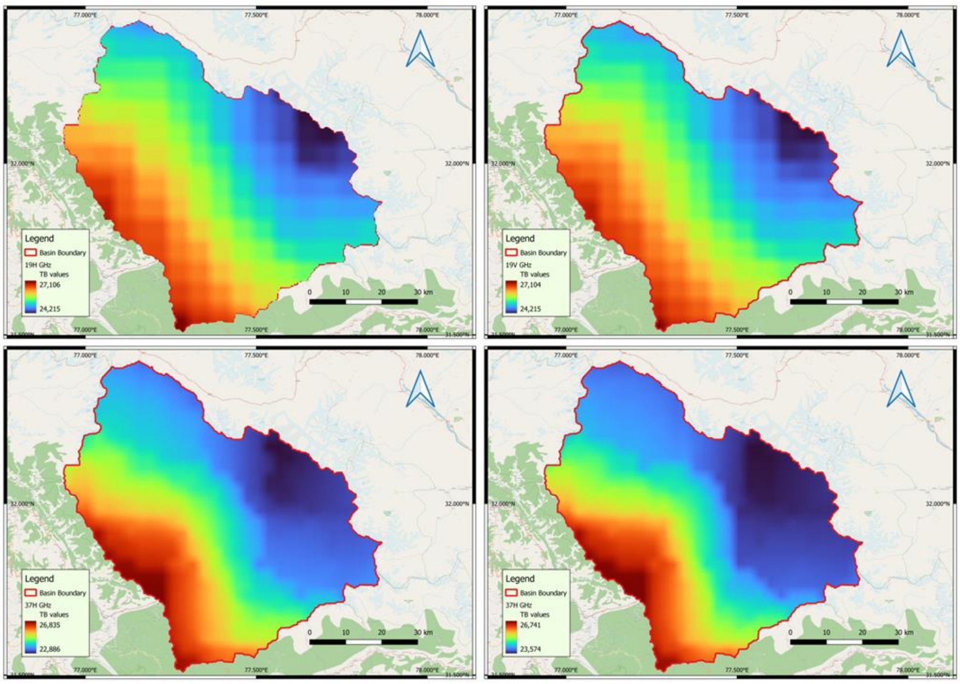

Figure 6-4: PMW TB values at 19H GHz(top left), 19V GHz (top right), 37H GHz (bottom left) and 37V GHz(bottom right)

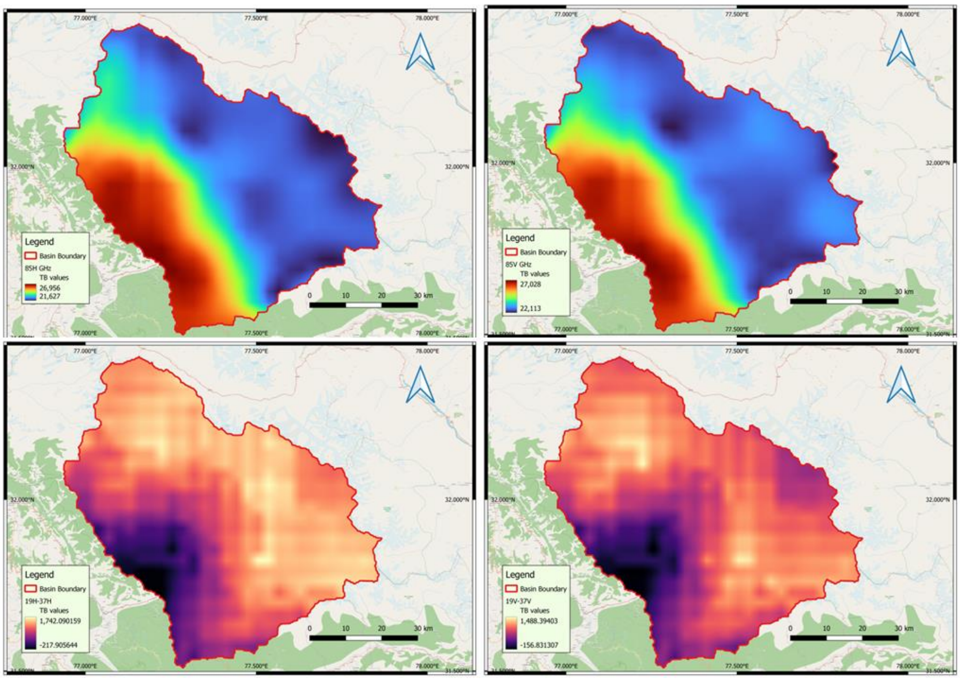

Figure 6-5: PMW TB Values at 85H GHz (top left), 85V GHz (top right), 19H-37H GHz (bottom left), 19V-37V GHz (bottom right)

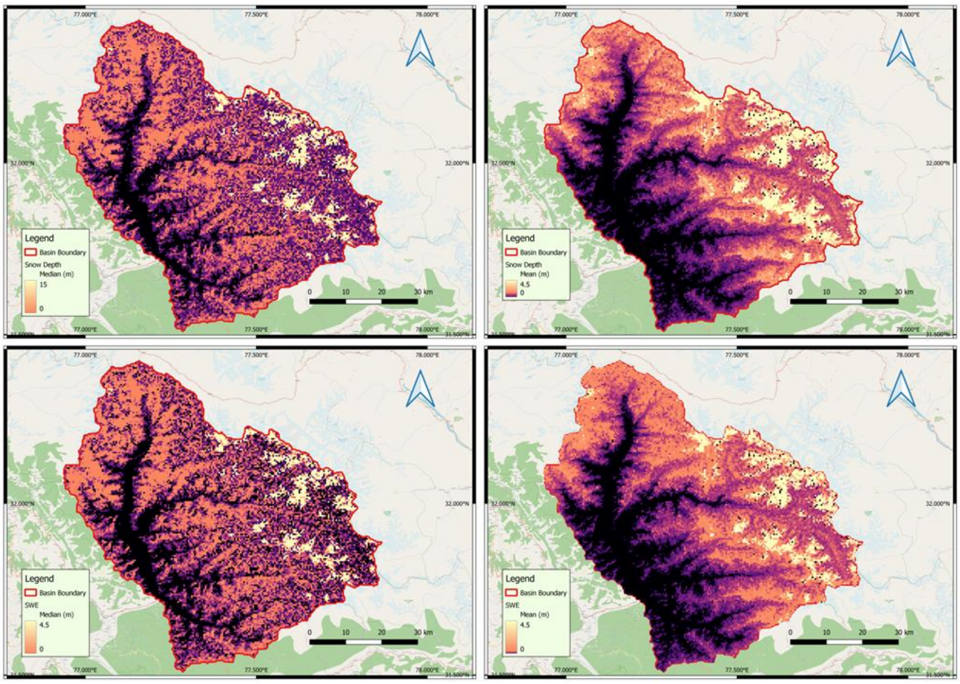

Figure 6-6: HMASR values of SD median (top left), SD mean (top right), SWE median (bottom left), and SWE mean (bottom right)

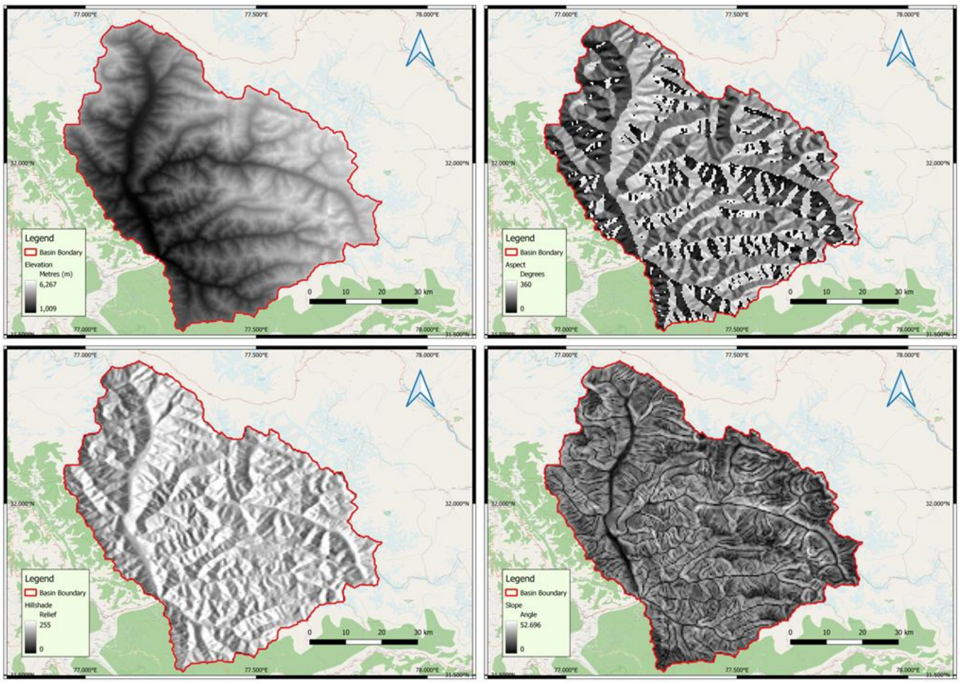

Figure 6-7: Feature extracted from SRTM DEM are elevation (top left), Aspect (top right), Slope (bottom left) and Hillshade (toom right)

6.2. Data Exploration Results

For data exploratory analysis, correlation between input features with SD and SWE has been calculated to check the weightage of each input variable which helped us to analysis like how each extracted features are affecting SD and SWE values.

Apart from that, SD and SWE time-series analysis has been done for water year 2016-2017. In this, it has been seen analysed that how SD and SWE values averagely varying on daily, monthly, and weekly basis. As snow cover changes from season to season, it has been expected that SD and SWE values will also varies season-wise.

For model training, missing outliers and no values handling is very important. To achieve that, all images has been masked with that date's snow cover area and SAR image. If snow cover pixel and SAR pixel is not present in study area, that pixel has been dropped for all other features. Similar problem arose when PMW temperature brightness values are not present because study area did not lie in either ascending or descending pass that day, those pixels has also been dropped.

Table 6-1: Correlation matrix of MODIS features with SD and SWE

	sca	ndvi	ndsi	sdmean	swemean
sca	1.000000	-0.539241	0.816160	0.247729	0.218141
ndvi	-0.539241	1.000000	-0.818601	-0.286607	-0.275002
ndsi	0.816160	-0.818601	1.000000	0.276786	0.257738
sdmean	0.247729	-0.286607	0.276786	1.000000	0.951886
swemean	0.218141	-0.275002	0.257738	0.951886	1.000000

Table 6-2: Correlation Matrix of Sentinel-1 SAR with SD and SWE

	vv	vh	dbr	angle	mask	sdmean	swemean
vv	1.000000	0.880295	-0.568742	-0.178278	0.566589	-0.039417	-0.066607
vh	0.880295	1.000000	-0.110437	-0.186604	0.535579	-0.011118	-0.077277
dbr	-0.568742	-0.110437	1.000000	0.049960	-0.258420	0.063300	0.005560
angle	-0.178278	-0.186604	0.049960	1.000000	-0.275517	0.012394	0.038595
mask	0.566589	0.535579	-0.258420	-0.275517	1.000000	-0.125548	-0.149189
sdmean	-0.039417	-0.011118	0.063300	0.012394	-0.125548	1.000000	0.951886
swemean	-0.066607	-0.077277	0.005560	0.038595	-0.149189	0.951886	1.000000

Table 6-3: Correlation Matrix of PMW features with SD and SWE

	stacked85v	stacked85h	stacked19h	stacked19v	stacked37h	stacked37v	stacked_diff_H	stacked_diff_V	sdmean	swemean
stacked85v	1.000000	0.987699	0.681051	0.680090	0.836007	0.848189	-0.739716	-0.616784	-0.208417	-0.192449
stacked85h	0.987699	1.000000	0.716505	0.713876	0.844774	0.842700	-0.714299	-0.563219	-0.213958	-0.188320
stacked19h	0.681051	0.716505	1.000000	0.997051	0.871418	0.821186	-0.431125	-0.173521	-0.200399	-0.122991
stacked19v	0.680090	0.713876	0.997051	1.000000	0.870608	0.820392	-0.433089	-0.175817	-0.198498	-0.121932
stacked37h	0.836007	0.844774	0.871418	0.870608	1.000000	0.987045	-0.818301	-0.619667	-0.221322	-0.184587
stacked37v	0.848189	0.842700	0.821186	0.820392	0.987045	1.000000	-0.853332	-0.704497	-0.220643	-0.193107
stacked_diff_H	-0.739716	-0.714299	-0.431125	-0.433089	-0.818301	-0.853332	1.000000	0.936483	0.172276	0.195409
stacked_diff_V	-0.616784	-0.563219	-0.173521	-0.175817	-0.619667	-0.704497	0.936483	1.000000	0.131550	0.180300
sdmean	-0.208417	-0.213958	-0.200399	-0.198498	-0.221322	-0.220643	0.172276	0.131550	1.000000	0.951886
swemean	-0.192449	-0.188320	-0.122991	-0.121932	-0.184587	-0.193107	0.195409	0.180300	0.951886	1.000000

Table 6-4: Correlation Matrix of Topographical and Climatological data with SD and SWE

	lulc	elevation	aspect	slope	hillshade	lst	chirps	sdmean	swemean
lulc	1.000000	0.731779	0.019336	-0.133235	0.008289	-0.229160	0.095101	0.316443	0.308731
elevation	0.731779	1.000000	0.029111	-0.143626	0.028483	-0.315855	0.115076	0.471044	0.451744
aspect	0.019336	0.029111	1.000000	-0.003426	0.688786	0.039474	0.001520	0.047512	0.050493
slope	-0.133235	-0.143626	-0.003426	1.000000	-0.080570	0.029442	0.053323	-0.112474	-0.114303
hillshade	0.008289	0.028483	0.688786	-0.080570	1.000000	0.055643	-0.013885	0.039922	0.044486
lst	-0.229160	-0.315855	0.039474	0.029442	0.055643	1.000000	0.135555	-0.242806	-0.150582
chirps	0.095101	0.115076	0.001520	0.053323	-0.013885	0.135555	1.000000	-0.036487	-0.008141
sdmean	0.316443	0.471044	0.047512	-0.112474	0.039922	-0.242806	-0.036487	1.000000	0.951886
swemean	0.308731	0.451744	0.050493	-0.114303	0.044486	-0.150582	-0.008141	0.951886	1.000000

Aggregate values of SD and SWE at daily, weekly and monthly basis and been plotted to see how it changes over the seasons

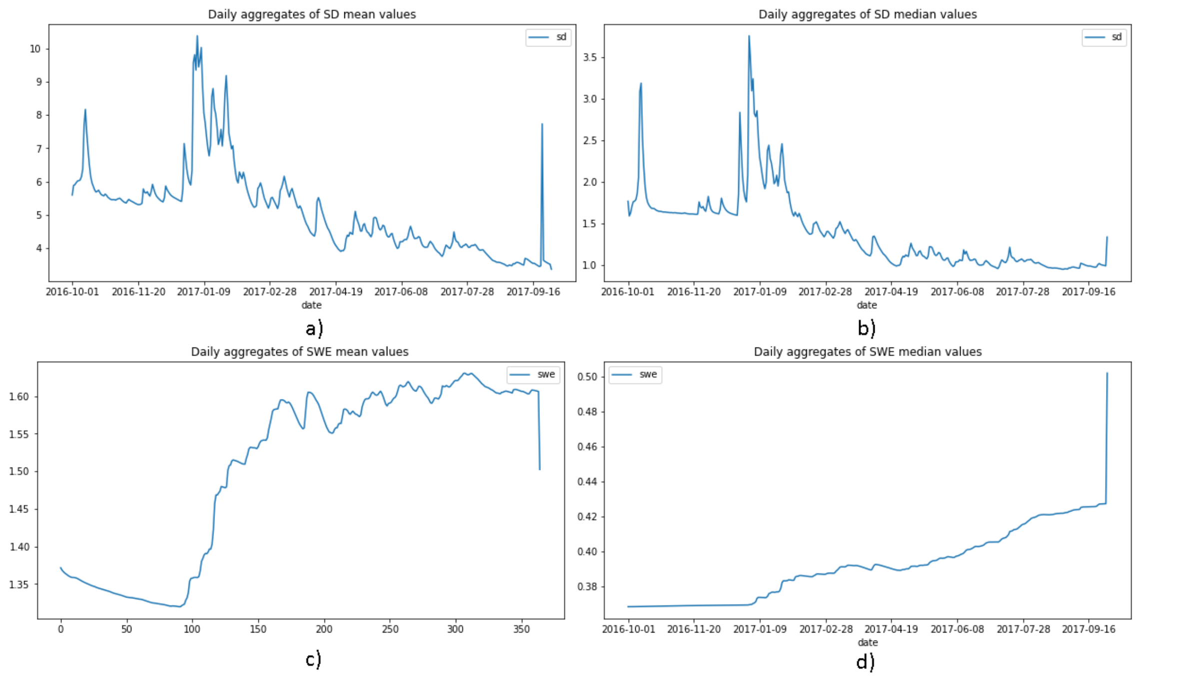

Figure 6-8: Daily aggregate values of a) SD mean values, b) SD median values, c) SWE mean values, d) SWE median values

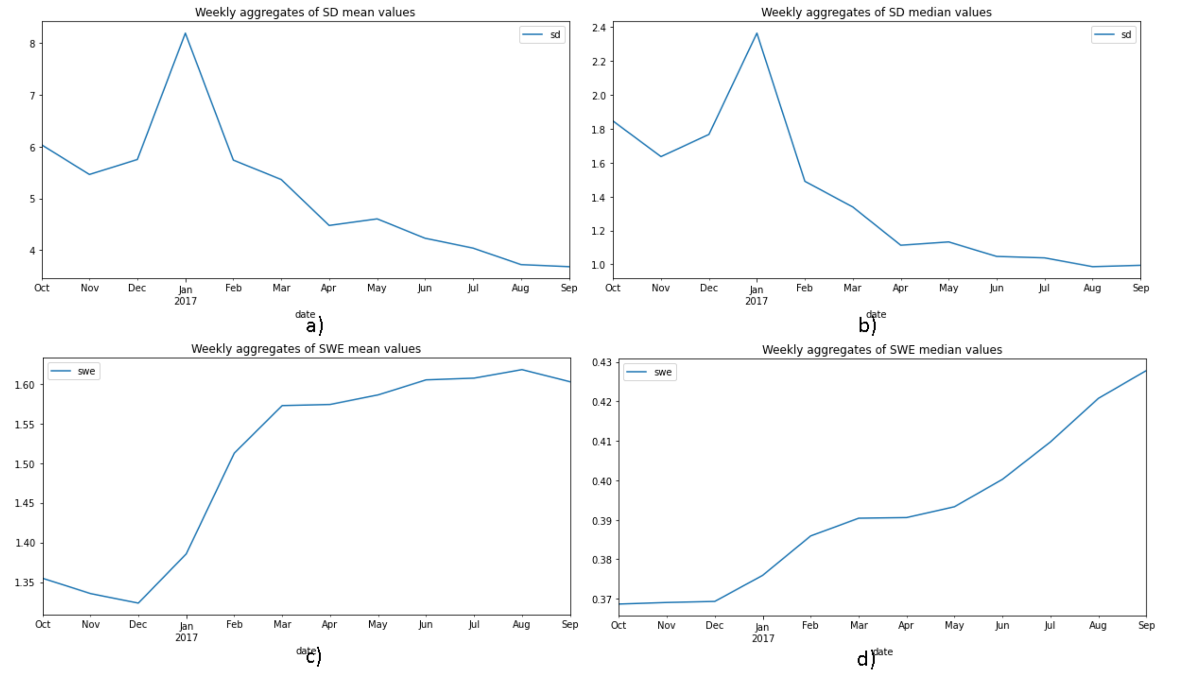

Figure 6-9: Weekly aggregate values of a) SD mean values, b) SD median values, c) SWE mean values, d) SWE median values

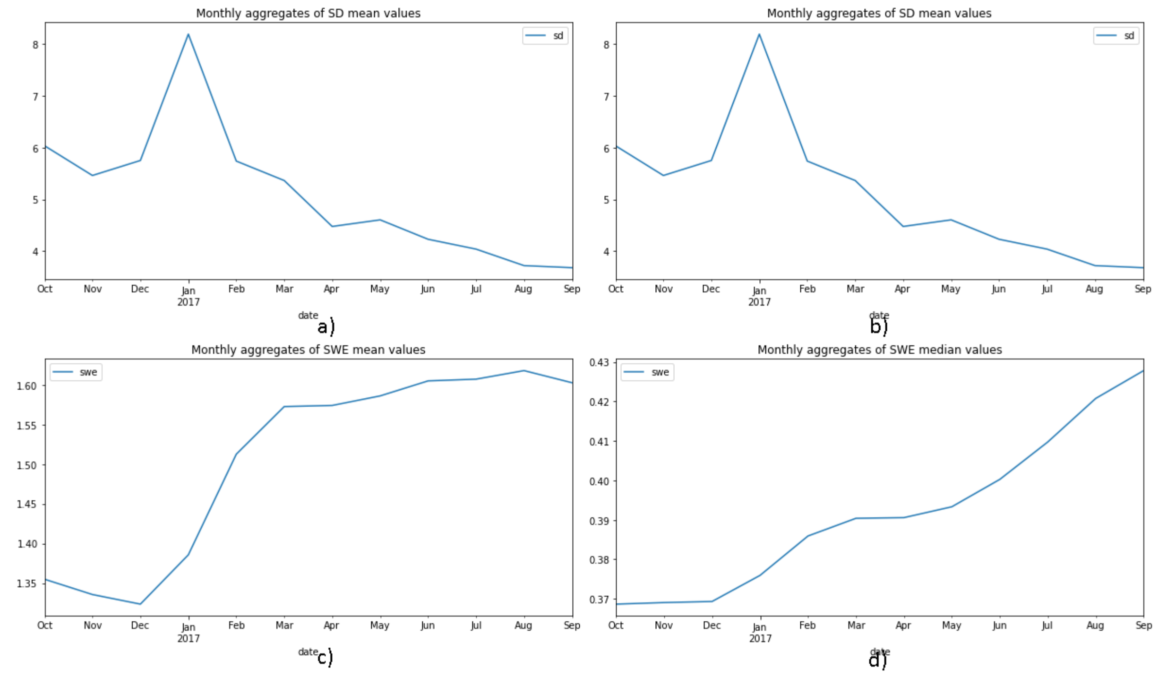

Figure 6-10: Monthly aggregate values of a) SD mean values, b) SD median values, c) SWE mean values, d) SWE median values

There is direct relation between SD and SWE according to their formula as their ratio gives snow density. But snow density varies with height, season and elevation. To analyze this changes in snow density, a correlation between SD and SWE values has also been created:

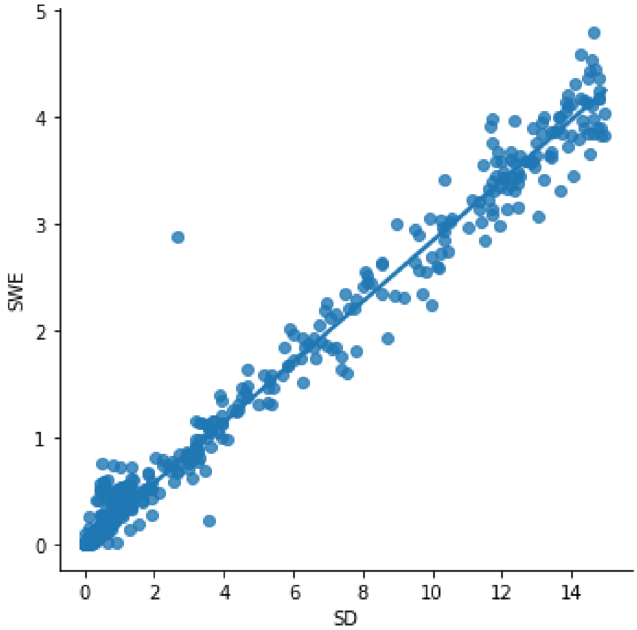

Figure 6-11: Correlation plot of SD and SWE

6.3. Model Results

Below tables shows the accuracy assessment of SD and SWE with both SVR and RFR model. With given results, further analysis with median data of SD and SWE will be disregarded due to lower accuracy and doubt on the quality of data.

Table 6-5: Model wise accuracy assessment

Model SVR	Accuracy Assessment	Train data	Test data
SD (mean)	**R squared**	0.894	0.675
	MAE	56.176	64.652
	RMSE	103.987	124.22
SD (median)	**R squared**	0.811	0.725
	MAE	7.447	9.401
	RMSE	13.940	24.302
SWE (mean)	**R squared**	0.861	0.708
	MAE	15.743	18.150
	RMSE	28.144	34.165
SWE (median)	**R squared**	0.7080	0.565
	MAE	2.750	15.743
	RMSE	5.407	28.144

Model RFR	Accuracy Assessment	Train data	Test data
SD (mean)	**R squared**	0.549	0.519
	MAE	92.459	96.018
	RMSE	169.565	175.498
SD (median)	**R squared**	0.322	0.227
	MAE	12.337	12.763
	RMSE	37.151	40.783
SWE (mean)	**R squared**	0.549	0.376
	MAE	92.459	26.243
	RMSE	169.565	47.745
SWE (median)	**R squared**	0.307	0.197
	MAE	4.547	4.752
	RMSE	13.396	14.851

Using above SVR model, SD and SWE results has been generated. As accuracy came better using ensemble mean values of HMASR data as a reference data, their accuracy has taken, and ensemble median results has been disregarded.

To create SD and SWE map, a gap filled data for date 24 Feb 2017 has been taken. Gaps generally occurred due to Full SAR pass was not present and cloud gaps in fSCA data. A composite of corresponding week has been taken to fill SAR and fSCA gap which resulted a complete input parameter datacube from which following results are generated

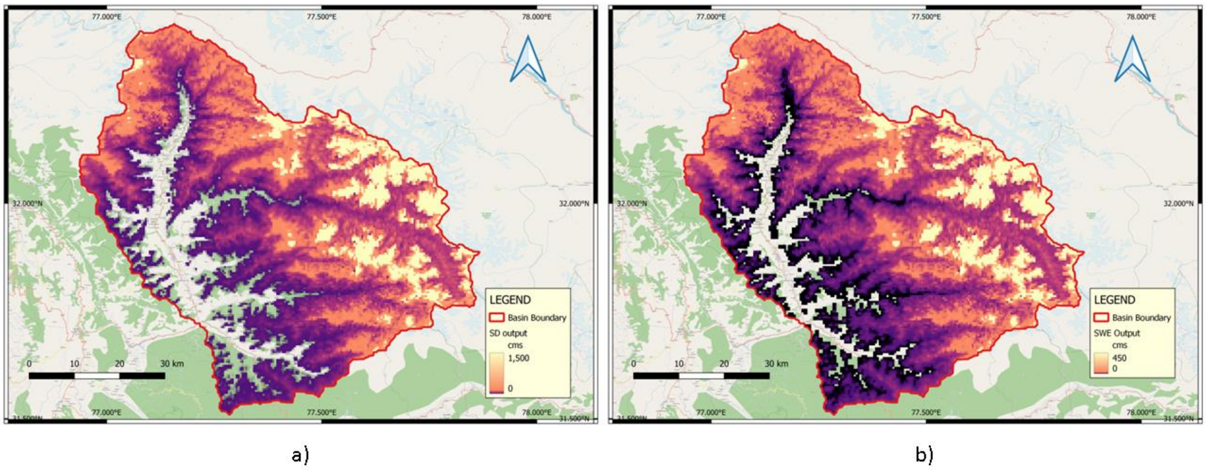

a) b)

Figure 6-12: Results of a) SD and b) SWE on date 24/02/2017 for Beas Basin

Using same approach, maps on same data has been generated for Sutlej Basin also.

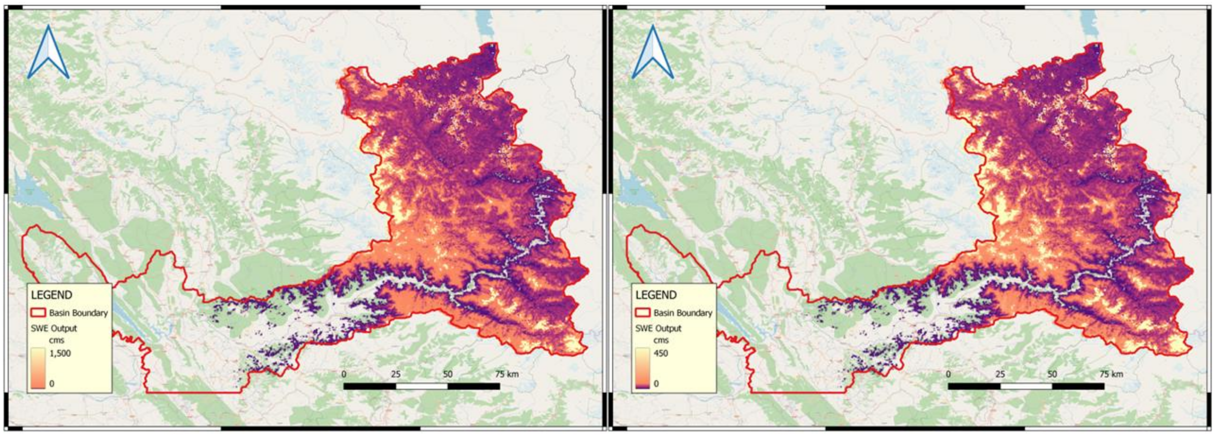

a) b)

Figure 6-13: Results of a) SD and b) SWE on date 24/02/2017 for Sutlej Basin

6.4. Field Visit Data

Table 6-6: Sample data of snow density at different depth, site- Kothi

DEPTH	ATTEN	FREQUEN	CY BAND	WETNESS	DENSITY	WETNESS
cm	A/D	MHz	MHz	%VOL	g/ccm	%WGT
0	001555	0730.2	23	1.72	0.184	9.2
5	001268	0795.0	16	0	0.133	0
10	001320	0797.2	17	0	0.129	0
15	001299	0809.7	19.5	0.1	0.103	0.9
20	001343	0814.8	18.7	0	0.099	0
25	000249	0720.8	45.3	6.17	(ice layer) 0	(ice layer) 0
30	000508	0589.8	22.3	5.73	0.337	16.9
35	000575	0671.1	19.8	2.31	0.291	7.9
40	000459	0643.5	18	2.41	0.359	6.6
45	000452	0646.1	17.8	2.26	0.358	6.2
50	000670	0631.1	16.2	2.02	0.413	4.8
55	000546	0649.7	19.5	2.81	0.322	8.6
60	000475	0649.8	19.7	2.95	0.315	9.3

6.5. Chapter Summary

In this chapter, results have presented in brief. First, data pre-processing results have been shared for important feature extracted to put into model followed by some charts that came across in data exploratory analysis. In last, model results have been presented and implementation has been done on different study area also.

7. DISCUSSION

As it is shown in previous chapter, model did not show good results with ensemble median values of HMASR data so that dataset has been disregarded and based of one study area, another study area has also been trained and model tested for that also.

SVR model has performed better as compared to RFR model in terms of minimizing the mean absolute error and root mean square error. Other issue while generating results came arrive because of missing values in dataset so a composite of nearby dates has been taken to create input data cube to put into model in order to receive SD and SWE estimated values

As both study area is different, problems came arrive in generalize the model for both as region is very different in terms of Land Cover and elevation. Upper part of Sutlej basin more arid as compared to that of Beas basin hence probability of getting more snow is more in Beas than that of Sutlej basin. So, a different dataset has been prepared to train in Sutlej basin area.

To the further analysis, elevation wise SD and SWE map has been created for both basins for February 2017 and result are as follows:

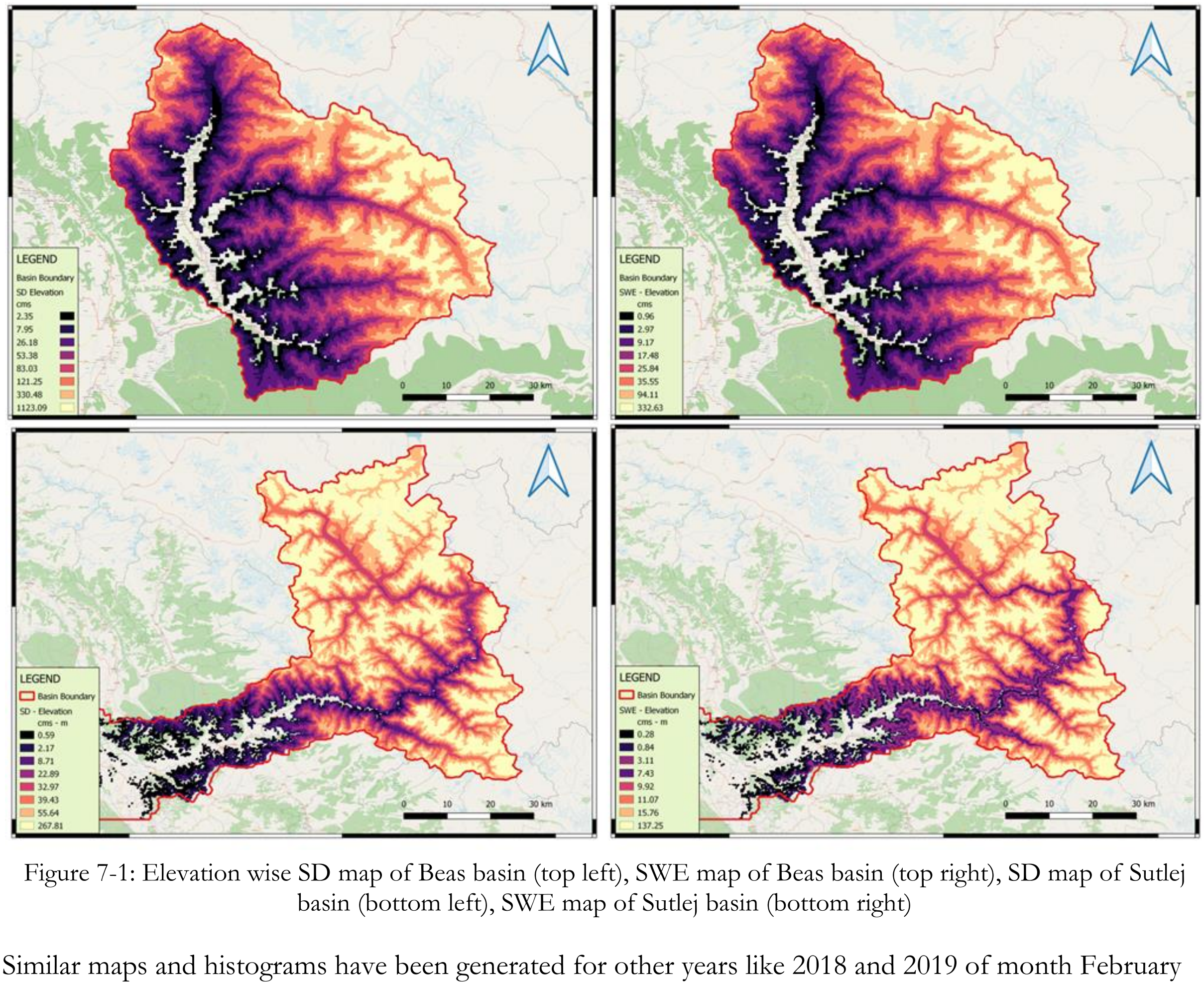

Figure 7-1: Elevation wise SD map of Beas basin (top left), SWE map of Beas basin (top right), SD map of Sutlej basin (bottom left), SWE map of Sutlej basin (bottom right)

Similar maps and histograms have been generated for other years like 2018 and 2019 of month February as we can see from our data exploratory analysis that mostly snow occurred around month of February. Above analysis has shown that that SD and SWE increase with increase in elevation of the region. This scenario we can see year wise in Sutlej basin for both SD and SWE values.

Table 7-1: SD and SWE elevation wise analysis for Sutlej basin

Sutlej	**SD**			**SWE**		
Year Elevations	**2017**	**2018**	**2019**	**2017**	**2018**	**2019**
<2000	0.083754	0.036721	0.230779	0.029243	0.013228	0.072357
2000-2500	1.934065	1.022234	5.450933	0.709462	0.404925	1.602610
2500-3000	8.616761	6.296936	19.863842	3.058381	2.381330	5.199774
3000-3500	22.768587	22.796783	38.741451	7.382878	7.461391	9.085172
3500-4000	32.919804	38.831807	47.032205	9.906069	11.351293	10.493782
4000-4500	39.309015	47.546993	49.988230	11.035028	12.975639	10.848758
4500-5000	55.033350	63.148932	65.976222	14.573079	16.442250	14.269657
5000-5500	202.440446	209.738348	220.417821	56.025328	57.694861	55.719734
6000>	402.869077	408.799256	426.014604	113.519374	114.607745	113.293399

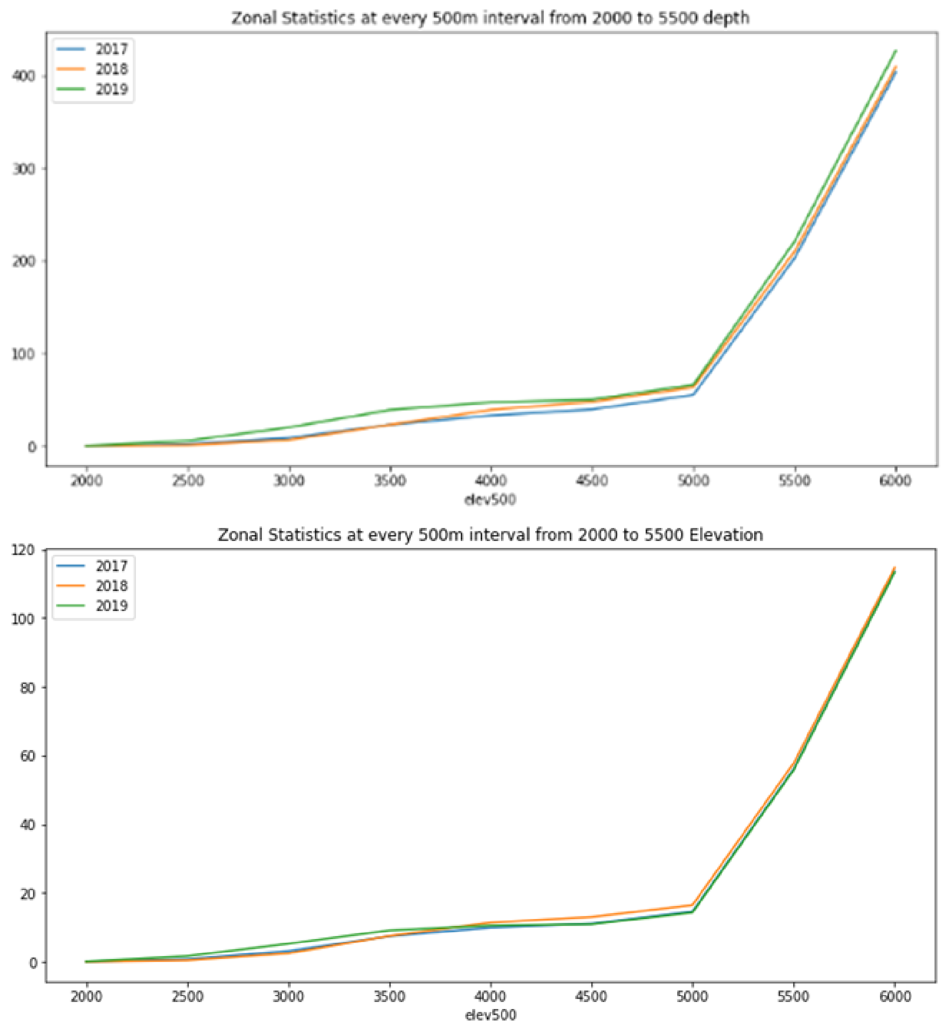

Figure 7-2: Line chart displays how SD(top) and SWE (bottom) values increases with increase in Elevation in Sutlej Basin

Above results has been obtained by taking aggregate value of SD and SWE in particular range of elevation values. In our case range has been taken at every step of 500m

Table 7-2: SD and SWE elevation wise analysis for Beas basin

Beas	SD			SWE		
Year Elevations	2017	2018	2019	2017	2018	2019
<2000	1.258780	0.732588	2.620102	0.029243	0.013228	0.072357
2000-2500	7.623067	5.382102	14.938209	0.709462	0.404925	1.602610
2500-3000	26.245470	23.106960	43.288546	3.058381	2.381330	5.199774
3000-3500	53.540944	57.249449	75.160110	7.382878	7.461391	9.085172
3500-4000	83.027661	95.605519	103.515829	9.906069	11.351293	10.493782
4000-4500	121.003070	136.831918	143.344074	11.035028	12.975639	10.848758
4500-5000	328.789750	341.397052	364.406894	14.573079	16.442250	14.269657
5000-5500	1088.927581	1093.728857	1124.717101	56.025328	57.694861	55.719734
6000>	1347.049442	1350.717261	1372.286646	113.519374	114.607745	113.293399

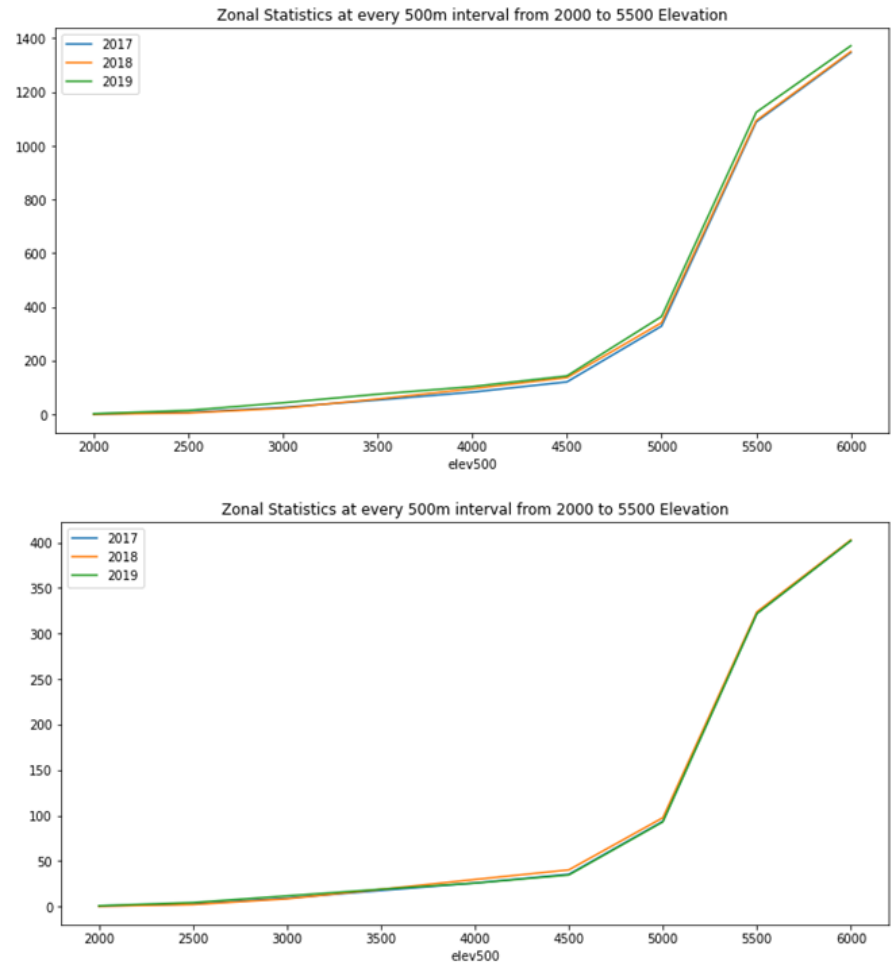

Figure 7-3: Line chart displays how SD(top) and SWE (bottom) values increases with increase in Elevation in Beas Basin

Similar analysis has been done to check how SD and SWE values are varying with change in aspect. Again, SD and SWE values has been aggregated for year 2017,2018 and 2019 of month February and results has been matched:

Table 7-3: Aggregated values of SD and SWE according to Aspect for year 2017,2018 and 2019 in Beas Basin

Sutlej	SD			SWE		
Year Elevations	2017	2018	2019	2017	2018	2019
0-90	94.054635	98.039571	102.626162	25.829816	26.843304	25.807562
90-180	96.008271	100.174380	106.993528	27.519179	28.434375	27.634578
180-270	45.840738	49.590333	55.265001	13.081784	13.788167	13.349906
270-360	82.072269	86.020528	91.820914	22.310112	23.278484	22.405013

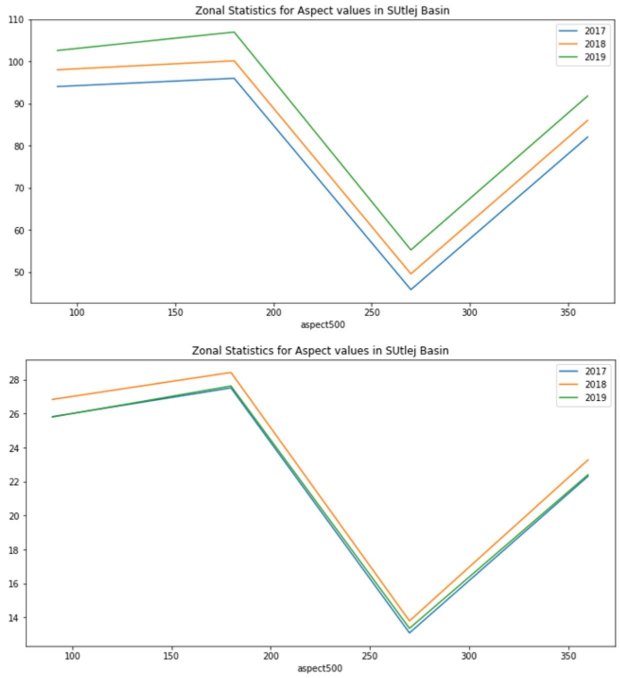

Figure 7-4: Line chart for observing change of SD and SWE values with Aspect in Sutlej basin

Table 7-4: Aggregated values of SD and SWE according to Aspect for year 2017,2018 and 2019 in Beas Basin

Beas	SD			SWE		
Year Elevations	2017	2018	2019	2017	2018	2019
0-90	182.026578	186.192781	196.925913	53.192698	54.638080	53.498531
90-180	211.880395	216.549148	230.945087	63.458188	64.931158	64.039908
180-270	196.873659	203.644062	220.800583	59.167766	61.098120	59.914660
270-360	196.299510	201.789571	216.440989	57.399274	59.266770	57.816401

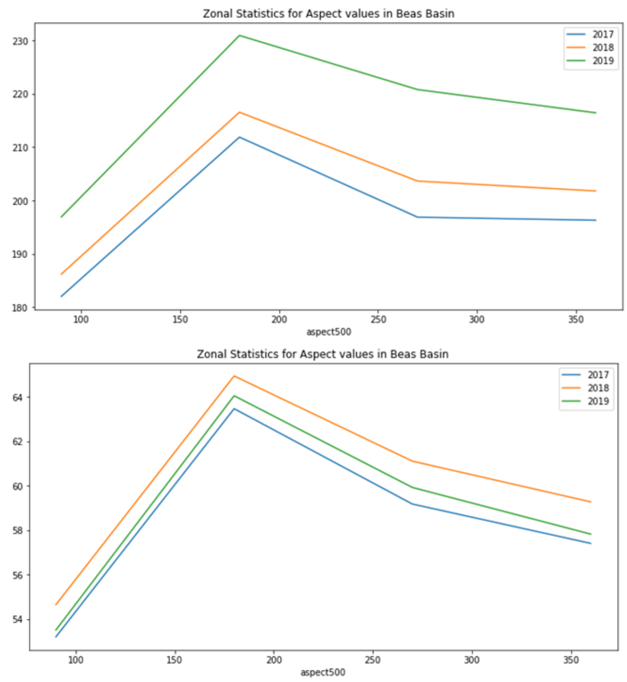

Figure 7-5: Line chart for observing change of SD and SWE values with Aspect in Sutlej basin

To extract the different types of features using different multi-sensor data for SD and SWE estimation

In all feature that has been extracted, CHIRPS data and 22 GHz did not play any important role. CHIRPS was not sufficient for model training because of its very coarse resolution and accuracy issues. On another hand, 22GHz TB values of SSMI sensor were not falling in our study area. Apart from that, all feature played decent role in development of model out of them, elevation related features played more important role in model training as elevation and aspect (to be precise) highly correlates with SD and SWE values.

To find an optimal downscaling technique for the fusion of extracted features from multi-sensor data

Out of all spatial and temporal resolution tested, 500m at availability of SAR, or Weekly composite of all features to fill gaps has been the most optimal resolution for our model and results obtained. Having availability of high-resolution dataset like for optical sensor could have increased the spatial resolution but temporal resolution as challenge has been continued.

To create a generalized model based on features extracted from the collection of datasets and implement a machine learning model for SD and SWE estimation

Even though a generalized approach has been followed to train the model, even then having two different study area was quite a challenge to create a single generalized model. Apart from SVR, other deep learning models could have been tested to increase the accuracy and reduce the error coming along with it. Overall SR performed nice, and a comparison has also been done with RFR model.

8. CONCLUSION AND RECOMMENDATIONS

8.1. Conclusions

This research work majorly focussed on SD and SWE estimation with optimal spatial and temporal resolution using multi-sensor remote sensing data with some other topographical and climatological dataset using ML model like SVR and a comparison of it has been done using RFR model. Results for Beas basin has been common better than Sutlej basin because of sampling of dataset was better for Beas basin as compared to Sutlej basin. Beas basin has lower snowline and has more forest cover whereas Sutlej basin especially near in Lauhal and Spiti district, it is arid and snow line is much higher as compare that of Beas basin. Both results have been displayed and discussed in previous chapters. In section more talks about the research questions which came in start of this thesis and when the idea formulated for the further procedure of the research work.

What are input optimal features that can be obtained from multi-sensor data?

Different datasets gave us different values which we can correlate with SD and SWE values. Let us take first case of Sentinel-1 SAR. Sentinel-1 GRD data primarily has been used for this research from which we can obtain backscattering values of VV and VH band for our study and angle values at every 12 days and taking both ascending and descending pass it was 6 days. For optical sensor, MODIS different product has been used primarily SCA, NDSI and NDVI values. A climatological data has also been obtained from optical sensor which is LST. MODIS data was available daily, but it was having cloud gaps due inability of optical and thermal sensors for cloud penetration. In the end, PMW gave us brightness temperature at different frequencies like 19 GHz, 22 GHz, 37 GHz, 85 GHz from SSMI sensor for both ascending and descending pass out of which descending pass has been used because of its ability in our study area (Ahmad et al., 2019; Brodzik et al., 2020; Gan et al., 2013). Both Horizontal and vertical polarization of dataset has been used for feature extraction from PMW sensor. It was available at daily scale but sometime there was unavailability of dataset in both ascending and descending pass so such days has been skipped later based on either of data frequency's unavailability.

What are the useful SAR modalities (i.e., SAR, PolSAR, InSAR) for optimal feature extraction?

There are much research works which are done for SD and SWE using SAR and many of them use SAR modalities like PolSAR, PolInSAR and InSAR. PolSAR generally used for snow cover classification whereas other two has been used for SD and SWE estimation at different level of snow (Nagler et al., 2016; Snapir et al., 2019). The problem is these techniques required a lot of data processing before putting it into the model whereas in this research work, SAR backscattering like co-polarized (VV) and cross-polarized (VH) of SAR GRD data has been used because this dataset is smaller in size and easy to process as compared SAR SLC Level-1 data which used for techniques like InSAR and PolInSAR (Guneriussen et al., 2001). Availability of SAR GRD data on GEE made it easier to process for our study area and important parameter like backscattering ratio of VV and VH has been used because it highly affects the SD in a particular area. Other than that, angle values from SAR images have been used because it also correlated with SD and SWE values and help to avoid SAR shadowing issues like layover and foreshortening. A mask wet and dry snow cover has also been processed using co-polarized band of SAR for snow cover area to do different estimation for both (X. Zhong et al., 2018).

Which downscaling technique can be used to get SD and SWE at an efficient resolution?
To keep model generalized and efficient, same machine learning model which used for the SD and SWE estimation has been used for the downscaling also. Including another model separately for downscaling could increase the complexity of overall SD and SWE estimation process. To solve this issue, coarse resolution data has been resampled using bilinear interpolation and trained with model at 500m resolution. Using this input dataset, downscaling, which was required for especially PMW sensor has been done using the same model for training. Using this method, we were able to achieve efficient resolution both spatially and temporally. Some other datasets which had to resample from coarse resolution to fine resolution apart from PMW were LST and CHIRPS precipitation. Bilinear interpolation performed well for input dataset and estimation model generated decent resolution at fine resolution also.

What optimal resolution can be obtained by the fusion of multi-sensor data?
Aim of this research was to publish estimated SD and SWE values at optimal temporal and spatial resolution. As it has been already known that different datasets have different spatial and temporal resolution like SAR is available at 10m resolution, but it is available at 12 days repeat cycle. Even if we are taking both ascending and descending pass into consideration, we can get max 6 days repeat pass. On the other hand, PMW sensor data was available at 3.125km to 6.25km range at daily cycle. It is almost 300 times coarse spatial resolution and 6-to-12-times better temporal resolution as compared to SAR. In the last, we had MODIS data mostly at 500m resolution twice a day (Aqua and Terra). An optimum solution for fusion of all these datasets came as SD and SWE estimation 500m as per the availability of SAR in the study area. Apart from that, daily SD and SWE estimation at 500m resolution using PMW and optical data has been tried to achieve. A monthly SD and SWE maps has been also tried to achieve at 30m fine resolution using other optical datasets like Landsat along with fusion of SAR for experimental purpose only whose results has been not verified because of lack of validation data availability and unavailability of reference data at that much fine resolution (Margot Flemming, 2020; Walters et al., 2014; L. Zhu et al., 2021b).

How can input features extracted affect the training of the model from SVR?
Different features show different feature importance with referenced SD and SWE values which has to be estimated using SVR model. According to the model which has been developed in this research has been shown that topographical factors like elevation, aspect and slope highly affects SD and SWE values. Due to shadowing error of SAR and mixing of both ascending and descending pass, SAR backscattering values and backscattering ratio has shown less feature importance as compared to topographical factors like elevation, aspect and slope. Other factors have been shown somewhat similar importance for SVR model. SVR has a drawback that with increase in number of different types of input features, it tends to show less accuracy so because of this reason, fusion of three different remote sensing sensors and other topographical and climatological data has been too much load on SVR model (Xiao et al., 2018a). Even then, decent accuracy has been achieved. Some static factors like land cover, week and month of the pixel data collect have been shown good correlation with SD and SWE values.

What are the optimal parameters of SVR to create a generalized model that gives results with minimum error?
Apart from some topographical and climatological data, precipitation data has shown very weak correlation with SD and SWE values in some regions because of unavailability of fine resolution rainfall data for water year which has taken in this research. Other factors like wet and dry snow have not been shown good correlation with SD and SWE due to unaffectedness of snow cover type or not good processing of wet and dry snow mask using SAR in GEE. Apart from that, different datasets have dropped according to the

different scenarios which came across in the model training. To keep the model most generalized, physiographical factors like latitude and longitude has been dropped from model training to estimate model results in any region in North-western Himalayas (Kirkham et al., 2019; Thakur et al., 2013, 2017).

What is the performance of SVR based model, and how precisely can SD and SWE be estimated?
SVR model came out to be better performed as compared to RFR model as it reduced the generalized error and estimated SD and SWE more accurately as compared to RFR. The major drawback has been seen in RFR model was the higher mean absolute and root mean square in the estimated regression values of SD and SWE.

8.2. Recommendations

Even though this research work was able to produce an optimum spatial and temporal resolution for SD and SWE estimation but many factor could have been more improved for this work. Model can be trained on ground data which are frequently available like SNOTEL data of USA but issue of spatial transfer of that model has been very difficult in our given study area. SAR was available at every 12 days repeat pass. To overcome this issue, other SAR sensors dataset could have been used like ERS, RADARSAT etc to reduce temporal gap between them. Other SAR modalities like time-series InSAR has been generated using High Performance Computing (HPC) systems priority or on cloud to use interferograms for time-series analysis on SD and SWE. Interpolation of Landsat or Sentinel-2 could have been used to generated daily snow cover maps to estimate SD and SWE values with temporal resolution. LiDAR could have also been used to validate the depth of fresh snow in the given study area. PMW sensor like SSMI-S could also have been to filled gaps in PMW data and to use frequencies like 91 GHz to estimate SD and SWE more accurately.

There are new models has been introduced like GAN or LSTM to fill spatial and temporal gap in dataset. These models work in Deep Learning algorithm, and they are able to generate outputs with good accuracies too. The major concern in thesis is going to be usage of too many datasets so fusion of PMW and optical dataset could have been done nicely to generate daily SD and SWE maps in the thesis work. Doing study in Himalayas is very hard because of too much debris present in Himalayas due to its harsh and sharp terrain. Weather conditions also varies in Himalayas rapidly but dataset for such climatological changes is not available as of now. Interpolation of coarse resolution dataset like CHIRPS for precipitation didn't help in thesis much. In future, availability of high-resolution air temperature data and precipitation data is going to be great help in better estimation of SD and SWE.

LIST OF REFERENCES

Abdel-Rahman, E. M., Mutanga, O., Adam, E., & Ismail, R. (2014). Detecting Sirex noctilio grey-attacked and lightning-struck pine trees using airborne hyperspectral data, random forest and support vector machines classifiers. *ISPRS Journal of Photogrammetry and Remote Sensing*, *88*, 48–59. https://doi.org/10.1016/J.ISPRSJPRS.2013.11.013

Abe, T., Yamaguchi, Y., & Sengoku, M. (1990). Expermental Study of Microwave Transmission in Snowpack. *IEEE Transactions on Geoscience and Remote Sensing*, *28*(5), 915–921. https://doi.org/10.1109/36.58981

Ahmad, J. A., Forman, B. A., & Kwon, Y. (2019). Analyzing Machine Learning Predictions of Passive Microwave Brightness Temperature Spectral Difference Over Snow-Covered Terrain in High Mountain Asia. *Frontiers in Earth Science*, *7*. https://doi.org/10.3389/FEART.2019.00212/PDF

Armstrong, R. L., & Brodzik, M. J. (2002). Hemispheric-scale comparison and evaluation of passive-microwave snow algorithms. *Annals of Glaciology*, *34*, 38–44. https://doi.org/10.3189/172756402781817428

Aschbacher, J., & Rott, H. (1989). Microwave emission of snow-covered and snow-free terrain from satellite measurements. *Advances in Space Research*, *9*(1), 289–295. https://doi.org/10.1016/0273-1177(89)90496-1

Avanzi, F., de Michele, C., Ghezzi, A., Jommi, C., & Pepe, M. (2014). A processing-modeling routine to use SNOTEL hourly data in snowpack dynamic models. *Advances in Water Resources*, *73*, 16–29. https://doi.org/10.1016/J.ADVWATRES.2014.06.011

Baghdadi, N., Gauthier, Y., & Bernier, M. (1997). Capability of multitemporal ERS-1 SAR data for wet-snow mapping. *Remote Sensing of Environment*, *60*(2), 174–186. https://doi.org/10.1016/S0034-4257(96)00180-0

Bair, E. H., Calfa, A. A., Rittger, K., & Dozier, J. (2018). Using machine learning for real-time estimates of snow water equivalent in the watersheds of Afghanistan. *Cryosphere*, *12*(5), 1579–1594. https://doi.org/10.5194/tc-12-1579-2018

Bajracharya, S. R., & Shrestha, B. (2011). *The Status of Glaciers in the Hindu Kush-Himalayan Region*. https://doi.org/10.53055/ICIMOD.551

Baker, D. G., Skaggs, R. H., & Ruschy, D. L. (1991). Snow Depth Required to Mask the Underlying Surface. *Journal of Applied Meteorology and Climatology*, *30*(3), 387–392.

Balk, B., & Elder, K. (2000). Combining binary decision tree and geostatistical methods to estimate snow distribution in a mountain watershed. *Water Resources Research*, *36*(1), 13–26. https://doi.org/10.1029/1999WR900251

Baronti, S., Alparone, L., Garzelli, A., & Nencini, F. (2004). Landsat ETM+ and SAR image fusion based on generalized intensity Modulation. *IEEE TRANSACTIONS ON GEOSCIENCE AND REMOTE SENSING*, *42*(12). https://doi.org/10.1109/TGRS.2004.838344

Belgiu, M., & Drăgu, L. (2016). Random forest in remote sensing: A review of applications and future directions. *ISPRS Journal of Photogrammetry and Remote Sensing*, *114*, 24–31. https://doi.org/10.1016/J.ISPRSJPRS.2016.01.011

Bernier, M. (1999). Determination of snow water equivalent using RADARSAT SAR data in eastern Canada. *Hydrological Processes*.

Bhutiyani, M. (1992). Avalanche problems in Nubra and Shyok valleysin Karakoram Himalaya, India. *Journal of Institution of Military Engineers of India*, *3*, 3–5.

Bhutiyani, M. R., Kale, V. S., & Pawar, N. J. (2010). Climate change and the precipitation variations in the northwestern Himalaya: 1866-2006. *International Journal of Climatology*, *30*(4), 535–548. https://doi.org/10.1002/JOC.1920

Biau, G., & Scornet, E. (2016). A random forest guided tour. *TEST*, *25*(2), 197–227. https://doi.org/10.1007/s11749-016-0481-7

Bohleber, P., Wagner, N., & Eisen, O. (2012). Permittivity of ice at radio frequencies: Part II. Artificial and natural polycrystalline ice. *Cold Regions Science and Technology*, *Complete*(83–84), 13–19. https://doi.org/10.1016/J.COLDREGIONS.2012.05.010

Breiman, L. (2001). Random forests. *Machine Learning*, *45*(1), 5–32. https://doi.org/10.1023/A:1010933404324

Brodzik, M. J., Long, D. G., Hardman, M. A., Paget, A., & Armstrong, R. (2020). MEaSUREs Calibrated Enhanced-Resolution Passive Microwave Daily EASE-Grid 2.0 Brightness Temperature ESDR, Version 1 NASA National Snow and Ice Data Center Distributed Active Archive Center. *National Snow and Ice Data Center*, 0–24. https://doi.org/https://doi.org/10.5067/MEASURES/CRYOSPHERE/NSIDC-06

Brown, R. D., & Mote, P. W. (2009). The response of Northern Hemisphere snow cover to a changing climate. *Journal of Climate*, *22*(8), 2124–2145. https://doi.org/10.1175/2008JCLI2665.1

Brown, R. D., & Robinson, D. A. (2011). Northern Hemisphere spring snow cover variability and change over 1922-2010 including an assessment of uncertainty. *Cryosphere*, *5*(1), 219–229. https://doi.org/10.5194/TC-5-219-2011

Broxton, P. D., van Leeuwen, W. J. D., & Biederman, J. A. (2019). Improving Snow Water Equivalent Maps With Machine Learning of Snow Survey and Lidar Measurements. *Water Resources Research*, *55*(5), 3739–3757. https://doi.org/10.1029/2018WR024146

Bryan, A. B., & Sanders, I. C. (1928). The Dielectric Constant of Air at Radio Frequencies. *Physical Review*, *32*(2), 302. https://doi.org/10.1103/PhysRev.32.302

Buchner, R., Barthel, J., & Stauber, J. (1999). The dielectric relaxation of water between 0 ° C and 35 ° C. *Chemical Physics Letters*, *306*(1–2), 57–63. https://doi.org/10.1016/S0009-2614(99)00455-8

Carper, W. J., Lillesand, T. M., & Kiefer, R. W. (1990). *The Use of Intensity-Hue-Saturation Transformations for Merging SPOT Panchromatic and ~ultispectral Image Data*.

Caruana, R., & Lawrence, S. (2000). *Overfitting in Neural Nets: Backpropagation, Conjugate Gradient, and Early Stopping*.

Chang, J. S., Brost, R. A., Isaksen, I. S. A., Madronich, S., Middleton, P., Stockwell, W. R., & Walcek, C. J. (1987). A three-dimensional Eulerian acid deposition model: Physical concepts and formulation. *Journal of Geophysical Research*, *92*(D12), 14681–14700. https://doi.org/10.1029/JD092ID12P14681

Chauhan, R., Chandra Kuniyal, J., Pandey, D. C., & Jamwal, J. (2016). The Spatial Analysis of Satluj Basin, Himachal Pradesh, India. *International Research Journal of Earth Sciences*, *4*(7), 15–26. http://www.isca.in/EARTH_SCI/Archive/v4/i7/2.ISCA-IRJES-2016-027.php#references

Chavez, P. S., Sides, S. C., & Anderson, J. A. (1991). *Comparison of Three Different Methods to Merge Multiresolution and Multispectral Data: Landsat TM and SPOT Panchromatic*.

Che, T., Li, X., Jin, R., Armstrong, R., & Zhang, T. (2008a). Snow depth derived from passive microwave remote-sensing data in China. *Annals of Glaciology*, *49*, 145–154. https://doi.org/10.3189/172756408787814690

Che, T., Li, X., Jin, R., Armstrong, R., & Zhang, T. (2008b). Snow depth derived from passive microwave remote-sensing data in China. *Annals of Glaciology*, *49*, 145–154. https://doi.org/10.3189/172756408787814690

Chen, C. te, Nijssen, B., Guo, J., Tsang, L., Wood, A. W., Hwang, J. N., & Lettenmaier, D. P. (2001). Passive microwave remote sensing of snow constrained by hydrological simulations. *IEEE Transactions on Geoscience and Remote Sensing*, *39*(8), 1744–1756. https://doi.org/10.1109/36.942553

Chen, X., Xu, C., Yang, X., & Tao, D. (2020). Long-Term Video Prediction via Criticization and Retrospection. *IEEE Transactions on Image Processing*, *29*, 7090–7103. https://doi.org/10.1109/TIP.2020.2998297

Davis, D. T., Chen, Z., Tsang, L., Hwang, J. N., & Chang, A. T. C. (1993). Retrieval of Snow Parameters by Iterative Inversion of a Neural Network. *IEEE Transactions on Geoscience and Remote Sensing*, *31*(4), 842–852. https://doi.org/10.1109/36.239907

de Gregorio, L., Callegari, M., Marin, C., Zebisch, M., Bruzzone, L., Demir, B., Strasser, U., Marke, T., Gunther, D., Nadalet, R., & Notarnicola, C. (2019). A Novel Data Fusion Technique for Snow Cover Retrieval. *IEEE Journal of Selected Topics in Applied Earth Observations and Remote Sensing*, *12*(8), 2862–2877. https://doi.org/10.1109/JSTARS.2019.2920676

Deems, J. S., Painter, T. H., & Finnegan, D. C. (2013). Lidar measurement of snow depth: A review. *Journal of Glaciology*, *59*(215), 467–479. https://doi.org/10.3189/2013JOG12J154

Deronde, B., Debruyn, W., Gontier, E., Goor, E., Jacobs, T., Verbeiren, S., & Vereecken, J. (2014). 15 years of processing and dissemination of SPOT-VEGETATION products. *Https://Doi.Org/10.1080/01431161.2014.883102*, *35*(7), 2402–2420. https://doi.org/10.1080/01431161.2014.883102

Díaz-Uriarte, R., & Alvarez de Andrés, S. (2006). Gene selection and classification of microarray data using random forest. *BMC Bioinformatics*, *7*(1), 1–13. https://doi.org/10.1186/1471-2105-7-3/FIGURES/1

Dietz, A. J., Kuenzer, C., Gessner, U., & Dech, S. (2012). Remote sensing of snow - a review of available methods. In *International Journal of Remote Sensing* (Vol. 33, Issue 13, pp. 4094–4134). https://doi.org/10.1080/01431161.2011.640964

Dumont, M., & Gascoin, S. (2016). Optical Remote Sensing of Snow Cover. *Land Surface Remote Sensing in Continental Hydrology*, 115–137. https://doi.org/10.1016/B978-1-78548-104-8.50004-8

Elder, K., & Dozier, J. (2000). Improving methods for measurement and estimation of snow storage in alpine watersheds. *International Association of Hydrological Sciences*.

Elder, K., Rosenthal, W., & Davis, R. E. (n.d.). *Estimating the spatial distribution of snow water equivalence in a montane watershed*. https://doi.org/10.1002/(SICI)1099-1085(199808/09)12:10/11

Ellison, W. J., Lamkaouchi, K., & Moreau, J. M. (1996). Water: a dielectric reference. *Journal of Molecular Liquids*, *68*(2–3), 171–279. https://doi.org/10.1016/0167-7322(96)00926-9

Erickson, T. A., Williams, M. W., & Winstral, A. (2005). Persistence of topographic controls on the spatial distribution of snow in rugged mountain terrain, Colorado, United States. *Water Resources Research*, *41*(4), 1–17. https://doi.org/10.1029/2003WR002973

Esmaeily-Gazkohani, A., Granberg, H. B., & Gwyn, Q. H. J. (2014). Repeat-pass cross-track interferometric SAR to measure dry snow water equivalent and depth. *Http://Dx.Doi.Org/10.5589/M10-064*, *36*, S316–S326. https://doi.org/10.5589/M10-064

Evans, S. (2016). DIELECTRIC PROPERTIES OF ICE AND SNOW-A REVIEW. *Scott Polar Research Institute, Cambridge, England.*

Faria, D. A., Pomeroy, J. W., & Essery, R. L. H. (2000). Effect of covariance between ablation and snow water equivalent on depletion of snow-covered area in a forest. *Hydrological Processes* , *14*(15), 2683–2695. https://doi.org/10.1002/1099-1085

Farr, T. G., Rosen, P. A., Caro, E., Crippen, R., Duren, R., Hensley, S., Kobrick, M., Paller, M., Rodriguez, E., Roth, L., Seal, D., Shaffer, S., Shimada, J., Umland, J., Werner, M., Oskin, M., Burbank, D., &

Alsdorf, D. E. (2007). The Shuttle Radar Topography Mission. *Reviews of Geophysics*, *45*(2), 2004. https://doi.org/10.1029/2005RG000183

Fassnacht, S. R., Brown, K. S. J., Blumberg, E. J., López Moreno, J. I., Covino, T. P., Kappas, M., Huang, Y., Leone, V., & Kashipazha, A. H. (2018). Distribution of snow depth variability. *Frontiers of Earth Science 2018 12:4*, *12*(4), 683–692. https://doi.org/10.1007/S11707-018-0714-Z

Fassnacht, S. R., & Deems, J. S. (2006). Measurement sampling and scaling for deep montane snow depth data. *Hydrological Processes*, *20*(4), 829–838. https://doi.org/10.1002/HYP.6119

Fassnacht, S. R., Dressler, K. A., & Bales, R. C. (2003). Snow water equivalent interpolation for the Colorado River Basin from snow telemetry (SNOTEL) data. *Water Resources Research*, *39*(8), 1208. https://doi.org/10.1029/2002WR001512

Fierz, C., Armstrong, R. L., Durand, Y., Etchevers, P., Greene, E., McClung, D. M., Nishimura, K., Satyawali, P. K., & Sokratov, S. a. (2009). The international classification for seasonal snow on the ground. In *UNESCO, IHP–VII, Technical Documents in Hydrology, No 83; IACS contribution No 1*. https://www.dora.lib4ri.ch/wsl/islandora/object/wsl%3A10162

Foster, J. L., Chang, A. T. C., & Hall, D. K. (1997a). Comparison of snow mass estimates from a prototype passive microwave snow algorithm, a revised algorithm and a snow depth climatology. *Remote Sensing of Environment*, *62*(2), 132–142. https://doi.org/10.1016/S0034-4257(97)00085-0

Foster, J. L., Chang, A. T. C., & Hall, D. K. (1997b). Comparison of snow mass estimates from a prototype passive microwave snow algorithm, a revised algorithm and a snow depth climatology. *Remote Sensing of Environment*, *62*(2), 132–142. https://doi.org/10.1016/S0034-4257(97)00085-0

Foster, J. L., Sun, C., Walker, J. P., Kelly, R., Chang, A., Dong, J., & Powell, H. (2005). Quantifying the uncertainty in passive microwave snow water equivalent observations. *Remote Sensing of Environment*, *94*(2), 187–203. https://doi.org/10.1016/J.RSE.2004.09.012

Gan, T. Y., Barry, R. G., Gizaw, M., Gobena, A., & Balaji, R. (2013). Changes in North American snowpacks for 1979–2007 detected from the snow water equivalent data of SMMR and SSM/I passive microwave and related climatic factors. *Journal of Geophysical Research: Atmospheres*, *118*(14), 7682–7697. https://doi.org/10.1002/JGRD.50507

Garzelli, A. (2004). *WAVELET-BASED FUSION OF OPTICAL AND SAR IMAGE DATA OVER URBAN AREA*.

Gauthier, G., Lebreton, J.-D., Menu, S., & Pradel, R. (2001). *SEASONAL SURVIVAL OF GREATER SNOW GEESE AND EFFECT OF HUNTING UNDER DEPENDENCE IN SIGHTING PROBABILITY*.

Gharaei-Manesh, S., Fathzadeh, A., & Taghizadeh-Mehrjardi, R. (2016). Comparison of artificial neural network and decision tree models in estimating spatial distribution of snow depth in a semi-arid region of Iran. *Cold Regions Science and Technology*, *122*, 26–35. https://doi.org/10.1016/J.COLDREGIONS.2015.11.004

Grody, N. C., & Basist, A. N. (1996). Global identification of snowcover using ssm/i measurements. *IEEE Transactions on Geoscience and Remote Sensing*, *34*(1), 237–249. https://doi.org/10.1109/36.481908

Grünewald, T., Bühler, Y., & Lehning, M. (2014). Elevation dependency of mountain snow depth. *Cryosphere*, *8*(6), 2381–2394. https://doi.org/10.5194/TC-8-2381-2014

Guneriussen, T., HǄgda, K. A., Johnsen, H., & Lauknes, I. (2001). InSAR for estimation of changes in snow water equivalent of dry snow. *IEEE Transactions on Geoscience and Remote Sensing*, *39*(10), 2101–2108. https://doi.org/10.1109/36.957273

Gungor, O., & Shan, J. (2012). *An Optimal Fusion Approach for Optical and SAR Images*.

Guo, Y., Li, C., & Liu, Q. (2019). R2n: A novel deep learning architecture for rain removal from single image. *Computers, Materials and Continua*, *58*(3), 829–843. https://doi.org/10.32604/CMC.2019.03729

Haack, B., Mahabir, R., & Kerkering, J. (2014). Remote sensing derived national Land cover Land use maps: A comparison for Malawi. *Geocarto International*. https://doi.org/10.1080/10106049.2014.952355

Hallikainen, M. T., Ulabz, F. T., Dobson, M. C., El-Rayes, M. A., & Wu, L. K. (1985). Microwave Dielectric Behavior of Wet Soil-Part I: Empirical Models and Experimental Observations. *IEEE Transactions on Geoscience and Remote Sensing*, *GE-23*(1), 25–34. https://doi.org/10.1109/TGRS.1985.289497

Hallikainen, M., Ulaby, F., van Deventer, T., Hallikainen, M., Ulaby, F., & van Deventer, T. (1987). Extinction Behavior of Dry Snow in the 18-to 90-GHz Range. *ITGRS*, *25*(6), 737–745. https://doi.org/10.1109/TGRS.1987.289743

Hornik, K., Stinchcombe, M., & White, H. (1989). *"Multilayer feedforward networks are universal approximators."*

Houborg, R., & McCabe, M. F. (2018). A hybrid training approach for leaf area index estimation via Cubist and random forests machine-learning. *ISPRS Journal of Photogrammetry and Remote Sensing*, *135*, 173–188. https://doi.org/10.1016/J.ISPRSJPRS.2017.10.004

Hultstrand, D. M., Fassnacht, S. R., Stednick, J. D., & Hiemstra, C. A. (2022). Snowpack distribution using topographical, climatological and winter season index inputs. *Atmosphere*, *13*(1), 3. https://doi.org/10.3390/ATMOS13010003/S1

Immerzeel, W. W., van Beek, L. P. H., & Bierkens, M. F. P. (2010). Climate change will affect the asian water towers. *Science*, *328*(5984), 1382–1385. https://doi.org/10.1126/science.1183188

Jap, D., Stöttinger, M., & Bhasin, S. (2015). Support vector regression. *Neural Information Processing – Letters and Reviews*, *11*, 1–8. https://doi.org/10.1145/2768566.2768568

Josberger, E. G., & Mognard, N. M. (2002). A passive microwave snow depth algorithm with a proxy for snow metamorphism. *Hydrological Processes*, *16*(8), 1557–1568. https://doi.org/10.1002/HYP.1020

Jost, G., Weiler, M., Gluns, D. R., & Alila, Y. (2007). The influence of forest and topography on snow accumulation and melt at the watershed-scale. *Journal of Hydrology*, *347*(1–2), 101–115. https://doi.org/10.1016/J.JHYDROL.2007.09.006

Kanchan Vasdev. (2021, June 16). Punjab: Water crisis looms as Bhakra dam level hits a record low. *The Indian Express*. https://indianexpress.com/article/cities/punjab-water-crisis-looms-as-bhakra-dam-level-hits-a-record-low-5219455/

Kim, D. H.-S. (2018). Mapping Snow Depth Using Moderate Resolution Imaging Spectroradiometer Satellite Images: Application to the Republic of Korea. *Korean Journal of Remote Sensing*, *34*(4), 625–638. https://doi.org/10.7780/KJRS.2018.34.4.5

Kirkham, J. D., Koch, I., Saloranta, T. M., Litt, M., Stigter, E. E., Møen, K., Thapa, A., Melvold, K., & Immerzeel, W. W. (2019). Near real-time measurement of snow water equivalent in the Nepal Himalayas. *Frontiers in Earth Science*, *7*. https://doi.org/10.3389/feart.2019.00177

Kulkarni, A. (1999). *Snow and glacier melt runoff model to estimate hydropower potential*.

Kulkarni, S. C., & Rege, P. P. (2020). Pixel level fusion techniques for SAR and optical images: A review. *Information Fusion*, *59*, 13–29. https://doi.org/10.1016/j.inffus.2020.01.003

Kumar, M., Marks, D., Dozier, J., Reba, M., & Winstral, A. (2013). Evaluation of distributed hydrologic impacts of temperature-index and energy-based snow models. *Advances in Water Resources*, *56*, 77–89. https://doi.org/10.1016/j.advwatres.2013.03.006

Kumar, V., Singh, P., & Singh, V. (2007). Snow and glacier melt contribution in the Beas River at Pandoh Dam, Himachal Pradesh, India. *Hydrological Sciences Journal*, *52*(2), 376–388. https://doi.org/10.1623/hysj.52.2.376

Kuusisto, E. (1984). *Snow accumulation and snowmelt in Finland*. https://helda.helsinki.fi/bitstream/handle/10138/31432/Vesientutkimuslaitoksen?sequence=1

Lee, P.-F., Chen, I.-C., & Tzeng, W.-N. (2005). Lee, P. F., Chen, I.-C., & Tzeng, W. N. (2005) Spatial and temporal distribution pattern of bigeye tuna (Thunnus obesus) in the Indian Ocean. Zoological Studies, 44, 260-270. *Zoological Studies*, *44*, 260–270.

Leinss, S., Parrella, G., & Hajnsek, I. (2014). Snow height determination by polarimetric phase differences in X-Band SAR Data. *IEEE Journal of Selected Topics in Applied Earth Observations and Remote Sensing*, *7*(9), 3794–3810. https://doi.org/10.1109/JSTARS.2014.2323199

Li, H., Wang, Z., He, G., & Man, W. (2017). Estimating snow depth and snow water equivalence using repeat-pass interferometric SAR in the northern piedmont region of the Tianshan Mountains. *Journal of Sensors*, *2017*. https://doi.org/10.1155/2017/8739598

Li, Q., Yang, T., Zhou, H., & Li, L. (2019a). Patterns in snow depth maximum and snow cover days during 1961–2015 period in the Tianshan Mountains, Central Asia. *Atmospheric Research*, *228*, 14–22. https://doi.org/10.1016/J.ATMOSRES.2019.05.004

Li, Q., Yang, T., Zhou, H., & Li, L. (2019b). Patterns in snow depth maximum and snow cover days during 1961–2015 period in the Tianshan Mountains, Central Asia. *Atmospheric Research*, *228*, 14–22. https://doi.org/10.1016/J.ATMOSRES.2019.05.004

Liang, J., Liu, X., Huang, K., Li, X., Shi, X., Chen, Y., & Li, J. (2015). Improved snow depth retrieval by integrating microwave brightness temperature and visible/infrared reflectance. *Remote Sensing of Environment*, *156*, 500–509. https://doi.org/10.1016/J.RSE.2014.10.016

Liou, Y. A. (1996). Annual temperature and radiobrightness signatures for bare soils. *IEEE Transactions on Geoscience and Remote Sensing*, *34*(4), 981–990. https://doi.org/10.1109/36.508415

Liu, C., Huang, X., Li, X., & Liang, T. (2020). MODIS fractional snow cover mapping using machine learning technology in a mountainous area. *Remote Sensing*, *12*(6). https://doi.org/10.3390/rs12060962

Liu, J., Zhang, Y., Cheng, X., & Hu, Y. (2019). Retrieval of snow depth over Arctic Sea ice using a deep neural network. *Remote Sensing*, *11*(23). https://doi.org/10.3390/rs11232864

Liu, M., Xiong, C., Pan, J., Wang, T., Shi, J., & Wang, N. (2020). High-resolution reconstruction of the maximum snow water equivalent based on remote sensing data in a mountainous area. *Remote Sensing*, *12*(3). https://doi.org/10.3390/RS12030460

Lu, L., Kuenzer, C., Wang, C., Guo, H., & Li, Q. (2015). Evaluation of three MODIS-derived vegetation index time series for dryland vegetation dynamics monitoring. *Remote Sensing*, *7*(6), 7597–7614. https://doi.org/10.3390/rs70607597

Lund, J., Forster, R. R., Rupper, S. B., Deeb, E. J., Marshall, H. P., Hashmi, M. Z., & Burgess, E. (2020). Mapping Snowmelt Progression in the Upper Indus Basin With Synthetic Aperture Radar. *Frontiers in Earth Science*, *7*, 318. https://doi.org/10.3389/feart.2019.00318

Lutz, A. F., Immerzeel, W. W., Kraaijenbrink, P. D. A., Shrestha, A. B., & Bierkens, M. F. P. (2016). Climate Change Impacts on the Upper Indus Hydrology: Sources, Shifts and Extremes. *PLOS ONE*, *11*(11), e0165630. https://doi.org/10.1371/journal.pone.0165630

Ma, C., & Tzler, «. (2002). Relation between grain-size and correlation length of snow. *Journal of Glaciology*, *48*(162), 461–466. https://doi.org/10.3189/172756502781831287

Majumdar, S., Thakur, P., Chang, L., Mani, S., & Kumar, S. (2019). *Snow Depth and Snow Water Equivalent Estimation in the Northwestern Himalayan Watershed using Spaceborne Polarimetric SAR Interferometry*. https://doi.org/10.31223/OSF.IO/6V4H3

Margot Flemming. (2020). *Downscaling Coarse Resolution Satellite Passive Microwave SWE Estimates*. Waterloo, Ontario, Canada. https://uwspace.uwaterloo.ca/handle/10012/15919

Mätzler, C. (1996). Microwave permittivity of dry snow. *IEEE Transactions on Geoscience and Remote Sensing*, *34*(2), 573–581. https://doi.org/10.1109/36.485133

Matzler, C., & Wegmuller, U. (1987). Dielectric properties of freshwater ice at microwave frequencies. *Journal of Physics D: Applied Physics*, *20*(12), 1623–1630. https://doi.org/10.1088/0022-3727/20/12/013

Maussion, F., Scherer, D., Mölg, T., Collier, E., Curio, J., & Finkelnburg, R. (2014). Precipitation Seasonality and Variability over the Tibetan Plateau as Resolved by the High Asia Reanalysis. *Journal of Climate*, *27*(5), 1910–1927. https://doi.org/10.1175/JCLI-D-13-00282.1

McClung, D., & Schaerer, P. A. (2006). *The avalanche handbook. The Mountaineers Books.*

Mei, X., Pan, E., Ma, Y., Dai, X., Huang, J., Fan, F., Du, Q., Zheng, H., & Ma, J. (2019). A Random Forest Machine Learning Approach for the Retrieval of Leaf Chlorophyll Content in Wheat. *Remote Sensing 2019, Vol. 11, Page 920*, *11*(8), 920. https://doi.org/10.3390/RS11080920

Mhawej, M., Faour, G., Fayad, A., & Shaban, A. (2014). Towards an enhanced method to map snow cover areas and derive snow-water equivalent in Lebanon. *Journal of Hydrology*, *513*, 274–282. https://doi.org/10.1016/j.jhydrol.2014.03.058

Miranda, N., & Meadows, P. J. (2015). *Radiometric Calibration of S-1 Level-1 Products Generated by the S-1 IPF.* https://sentinel.esa.int/documents/247904/685163/S1-Radiometric-Calibration-V1.0.pdf

Moreira, A., Prats-Iraola, P., Younis, M., Krieger, G., Hajnsek, I., & Papathanassiou, K. P. (2013). A tutorial on synthetic aperture radar. *IEEE Geoscience and Remote Sensing Magazine*, *1*(1), 6–43. https://doi.org/10.1109/MGRS.2013.2248301

Nagler, T., Rott, H., Ripper, E., Bippus, G., & Hetzenecker, M. (2016). Advancements for snowmelt monitoring by means of Sentinel-1 SAR. *Remote Sensing*, *8*(4). https://doi.org/10.3390/rs8040348

National Snow and Ice Data Center. (2016, November 30). *"All About Snow—Snow Science."* University of Colorado, Boulder. https://nsidc.org/cryosphere/snow

Petrenko, V. F., & Whitworth, R. W. (2002). Physics of Ice. *Physics of Ice*. https://doi.org/10.1093/ACPROF:OSO/9780198518945.001.0001

Pflug, J. M., & Lundquist, J. D. (2020). Inferring Distributed Snow Depth by Leveraging Snow Pattern Repeatability: Investigation Using 47 Lidar Observations in the Tuolumne Watershed, Sierra Nevada, California. *Water Resources Research*, *56*(9), e2020WR027243. https://doi.org/10.1029/2020WR027243

Pugh, M. L., Duggin, M. J., Waxman, A. M., & Hassett, J. M. (2004). Neural image fusion of remotely sensed electro-optical and synthetic aperture radar data for forest classification. *International Geoscience and Remote Sensing Symposium (IGARSS)*, *1*, 617–620. https://doi.org/10.1109/IGARSS.2004.1369103

Rakhecha, P., Kulkarni, A., Mandal, B., & Dhar, O. (1983). Winter andspring precipitation over the northwestern Himalaya., New Delhi,175 – 181. *Proceedings of the First National Symposium on Seasonal Snow Cover*, 175–181.

Ramadan, T. M., Nasrp, A. H., & Mahmood, A. (2006). *INTEGRATION OF RADARSAT-1 AND LANDSAT TM IMAGES FOR MINERAL EXPLORATION IN EAST OWEINAT DISTRICT, SOUTH WESTERN DESERT, EGYPT.*

Rani, S., & Sreekesh, S. (2019). Evaluating the Responses of Streamflow under Future Climate Change Scenarios in a Western Indian Himalaya Watershed. *Environmental Processes*, *6*(1). https://doi.org/10.1007/s40710-019-00361-2

Rees, A., English, M., Derksen, C., Toose, P., & Silis, A. (2014). Observations of late winter Canadian tundra snow cover properties. *Hydrological Processes*, *28*(12), 3962–3977. https://doi.org/10.1002/HYP.9931

Riche, F., Montagnat, M., & Schneebeli, M. (2013). Evolution of crystal orientation in snow during temperature gradient metamorphism. *Journal of Glaciology*, *59*(213), 47–55. https://doi.org/10.3189/2013JOG12J116

Romanov, P., & Tarpley, D. (2004). Estimation of snow depth over open prairie environments using GOES imager observations. *Hydrological Processes*, *18*(6), 1073–1087. https://doi.org/10.1002/HYP.5508

Romanov, P., & Tarpley, D. (2007). Enhanced algorithm for estimating snow depth from geostationary satellites. *Remote Sensing of Environment*, *108*(1), 97–110. https://doi.org/10.1016/J.RSE.2006.11.013

Rosenfeld, S., & Grody, N. (2000). Anomalous microwave spectra of snow cover observed from Special Sensor Microwave/Imager measurements. *Journal of Geophysical Research: Atmospheres*, *105*(D11), 14913–14925. https://doi.org/10.1029/1999JD900486

Rott, H., Nagler, T., & Scheiber, R. (2004). SNOW MASS RETRIEVAL BY MEANS OF SAR INTERFEROMETRY. *Proceedings of FRINGE 2003 Workshop*.

Salomonson, V. v., & Appel, I. (2004). Estimating fractional snow cover from MODIS using the normalized difference snow index. *Remote Sensing of Environment*, *89*(3), 351–360. https://doi.org/10.1016/J.RSE.2003.10.016

Senthilnath, J., Varia, N., Dokania, A., Anand, G., & Benediktsson, J. A. (2020). Deep TEC: Deep transfer learning with ensemble classifier for road extraction from UAV imagery. *Remote Sensing*, *12*(2). https://doi.org/10.3390/RS12020245

Shi, J., & Dozier, J. (2000). Estimation of snow water equivalence using SIR-C/X-SAR, Part I: Inferring snow density and subsurface properties. *IEEE Transactions on Geoscience and Remote Sensing*, *38*(6), 2465–2474. https://doi.org/10.1109/36.885195

Shukla, S., Jain, S. K., Kansal, M. L., & Chandniha, S. K. (2017). Assessment of sedimentation in Pong and Bhakra reservoirs in Himachal Pradesh, India, using geospatial technique. *Remote Sensing Applications: Society and Environment*, *8*, 148–156. https://doi.org/10.1016/j.rsase.2017.08.008

Sihvola, A., & Tiuri, M. (1986). Snow Fork for Field Determination of the Density and Wetness Profiles of a Snow Pack. *IEEE Transactions on Geoscience and Remote Sensing*, *GE-24*(5), 717–721. https://doi.org/10.1109/TGRS.1986.289619

Singh, P., & Bengtsson, L. (2004). Hydrological sensitivity of a large Himalayan basin to climate change. *Hydrological Processes*, *18*(13), 2363–2385. https://doi.org/10.1002/hyp.1468

Singh, P., & Jain, S. K. (2002). Snow and glacier melt in the Satluj River at Bhakra Dam in the western Himalayan region. *Undefined*, *47*(1), 93–106. https://doi.org/10.1080/02626660209492910

Singh, P. R., & Gan, T. Y. (2000). Retrieval of snow water equivalent using passive microwave brightness temperature data. *Remote Sensing of Environment*, *74*(2), 275–286. https://doi.org/10.1016/S0034-4257(00)00121-8

Smith, T., & Bookhagen, B. (2018). Changes in seasonal snow water equivalent distribution in high mountain Asia (1987 to 2009). In *Science Advances* (Vol. 4, Issue 1). https://doi.org/10.1126/sciadv.1701550

Snapir, B., Momblanch, A., Jain, S. K., Waine, T. W., & Holman, I. P. (2019). A method for monthly mapping of wet and dry snow using Sentinel-1 and MODIS: Application to a Himalayan river basin. *International Journal of Applied Earth Observation and Geoinformation*, *74*, 222–230. https://doi.org/10.1016/j.jag.2018.09.011

Sonobe, R., Sano, T., & Horie, H. (2018). Using spectral reflectance to estimate leaf chlorophyll content of tea with shading treatments. *Biosystems Engineering*, *175*, 168–182. https://doi.org/10.1016/J.BIOSYSTEMSENG.2018.09.018

Sturm, M., & Benson, C. (2004). Scales of spatial heterogeneity for perennial and seasonal snow layers. *Annals of Glaciology*, *38*, 253–260. https://doi.org/10.3189/172756404781815112

SUN, Z., YU, P., XIA, L., WU, S., JIANG, L., & GUO, L. (2015). Progress in study of snow parameter inversion by passive microwave remote sensing. *Remote Sensing for Land & Resources*, *1*, 9–15.

Tabari, H., Marofi, S., Abyaneh, H. Z., & Sharifi, M. R. (2010). Comparison of artificial neural network and combined models in estimating spatial distribution of snow depth and snow water equivalent in Samsami basin of Iran. *Neural Computing and Applications*, *19*(4), 625–635. https://doi.org/10.1007/S00521-009-0320-9

Takala, M., Luojus, K., Pulliainen, J., Derksen, C., Lemmetyinen, J., Kärnä, J. P., Koskinen, J., & Bojkov, B. (2011). Estimating northern hemisphere snow water equivalent for climate research through assimilation of space-borne radiometer data and ground-based measurements. *Remote Sensing of Environment*, *115*(12), 3517–3529. https://doi.org/10.1016/j.rse.2011.08.014

Tedesco, M., & Jeyaratnam, J. (2016). A new operational snow retrieval algorithm applied to historical AMSR-E brightness temperatures. *Remote Sensing*, *8*(12). https://doi.org/10.3390/rs8121037

Tedesco, M., Pulliainen, J., Takala, M., Hallikainen, M., & Pampaloni, P. (2004a). Artificial neural network-based techniques for the retrieval of SWE and snow depth from SSM/I data. *Remote Sensing of Environment*, *90*(1), 76–85. https://doi.org/10.1016/J.RSE.2003.12.002

Tedesco, M., Pulliainen, J., Takala, M., Hallikainen, M., & Pampaloni, P. (2004b). Artificial neural network-based techniques for the retrieval of SWE and snow depth from SSM/I data. *Remote Sensing of Environment*, *90*(1), 76–85. https://doi.org/10.1016/J.RSE.2003.12.002

Thakur, P. K., Aggarwal, S. P., Arun, G., Sood, S., Senthil Kumar, A., Mani, S., & Dobhal, D. P. (2017). Estimation of Snow Cover Area, Snow Physical Properties and Glacier Classification in Parts of Western Himalayas Using C-Band SAR Data. *Journal of the Indian Society of Remote Sensing*, *45*(3), 525–539. https://doi.org/10.1007/S12524-016-0609-Y/FIGURES/11

Thakur, P. K., Aggarwal, S. P., Garg, P. K., Garg, R. D., Mani, S., Pandit, A., & Kumar, S. (2012). Snow physical parameters estimation using space-based Synthetic Aperture Radar. *Geocarto International*, *27*(3), 263–288. https://doi.org/10.1080/10106049.2012.672477

Thakur, P. K., Garg, P. K., Aggarwal, S. P., Garg, R. D., & Mani, S. (2013). Snow Cover Area Mapping Using Synthetic Aperture Radar in Manali Watershed of Beas River in the Northwest Himalayas. *Journal of the Indian Society of Remote Sensing*, *41*(4), 933–945. https://doi.org/10.1007/s12524-012-0236-1

Torres, R., Snoeij, P., Geudtner, D., Bibby, D., Davidson, M., Attema, E., Potin, P., Rommen, B. Ö., Floury, N., Brown, M., Traver, I. N., Deghaye, P., Duesmann, B., Rosich, B., Miranda, N., Bruno, C., L'Abbate, M., Croci, R., Pietropaolo, A., … Rostan, F. (2012). GMES Sentinel-1 mission. *Remote Sensing of Environment*, *120*, 9–24. https://doi.org/10.1016/J.RSE.2011.05.028

Tsai, Y.-L. S., Dietz, A., Oppelt, N., & Kuenzer, C. (2019). Remote Sensing of Snow Cover Using Spaceborne SAR: A Review. *Remote Sensing*, *11*(12). https://doi.org/10.3390/rs11121456

Tsang, L., Pan, J., Liang, D., Li, Z., Cline, D. W., & Tan, Y. (2007). Modeling Active Microwave Remote Sensing of Snow Using Dense Media Radiative Transfer (DMRT) Theory With Multiple-Scattering Effects. *IEEE TRANSACTIONS ON GEOSCIENCE AND REMOTE SENSING*, *45*(4). https://doi.org/10.1109/TGRS.2006.888854

Ulaby, F. T., Stiles, W. H., Dellwig, L. F., & Hanson, B. C. (1977). Experiments on the Radar Backscatter of Snow. *IEEE Transactions on Geoscience Electronics*, *15*(4), 185–189. https://doi.org/10.1109/TGE.1977.294490

USDA Natural Resources Conservation Service. (2021). SNOwpack TELemetry Network (SNOTEL). *NRCS*. https://data.nal.usda.gov/dataset/snowpack-telemetry-network-snotel

Vapnik, V. (1998). The Support Vector Method of Function Estimation. *Nonlinear Modeling*, 55–85. https://doi.org/10.1007/978-1-4615-5703-6_3

Vikas Vasudeva. (2021, October 9). Environmentalists alarmed as Himachal witnesses lesser snow. *The HIndu*. https://www.thehindu.com/sci-tech/energy-and-environment/environmentalists-alarmed-as-himachal-witnesses-lesser-snow/article36915978.ece

Walker, A. E., & Goodison, B. E. (1993). Discrimination of a wet snow cover using passive microwave satellite data. *Annals of Glaciology*, *17*, 307–311. https://doi.org/10.3189/S026030550001301X

Walters, R. D., Watson, K. A., Marshall, H. P., McNamara, J. P., & Flores, A. N. (2014). A physiographic approach to downscaling fractional snow cover data in mountainous regions. *Remote Sensing of Environment*, *152*, 413–425. https://doi.org/10.1016/j.rse.2014.07.001

Warren, S. G., & Brandt, R. E. (2008). Optical constants of ice from the ultraviolet to the microwave: A revised compilation. *J. Geophys. Res*, *113*, 14220. https://doi.org/10.1029/2007JD009744

Williams, M. W. (2013). The Status of Glaciers in the Hindu Kush–Himalayan Region. *Mountain Research and Development*, *33*(1), 114. https://doi.org/10.1659/MRD.MM113

Winkler, R. D., Spittlehouse, D. L., & Golding, D. L. (2005). Measured differences in snow accumulation and melt among clearcut, juvenile, and mature forests in southern British Columbia. *Hydrological Processes*, *19*(1), 51–62. https://doi.org/10.1002/HYP.5757

Winstral, A., & Marks, D. (2002). Simulating wind fields and snow redistribution using terrain-based parameters to model snow accumulation and melt over a semi-arid mountain catchment. *Hydrological Processes*, *16*(18), 3585–3603. https://doi.org/10.1002/HYP.1238

Winther, J. G., Gerland, S., Ørbæk, J. B., Ivanov, B., Blanco, A., & Boike, J. (1999). Spectral reflectance of melting snow in a high Arctic watershed on Svalbard: Some implications for optical satellite remote sensing studies. *Hydrological Processes*, *13*(12–13), 2033–2049. https://doi.org/10.1002/(SICI)1099-1085(199909)13:12/13<2033::AID-HYP892>3.0.CO;2-M

Wu, H., Liu, Q., & Liu, X. (2019). A review on deep learning approaches to image classification and object segmentation. *Computers, Materials and Continua*, *60*(2), 575–597. https://doi.org/10.32604/CMC.2019.03595

Xiao, X., Zhang, T., Zhong, X., Shao, W., & Li, X. (2018a). Support vector regression snow-depth retrieval algorithm using passive microwave remote sensing data. *Remote Sensing of Environment*, *210*, 48–64. https://doi.org/10.1016/j.rse.2018.03.008

Xiao, X., Zhang, T., Zhong, X., Shao, W., & Li, X. (2018b). Support vector regression snow-depth retrieval algorithm using passive microwave remote sensing data. *Remote Sensing of Environment*, *210*, 48–64. https://doi.org/10.1016/J.RSE.2018.03.008

Xu, F., Zhang, X., Xin, Z., & Yang, A. (2019). Investigation on the Chinese text sentiment analysis based on convolutional neural networks in deep learning. *Computers, Materials and Continua*, *58*(3), 697–709. https://doi.org/10.32604/CMC.2019.05375

Xu, Y., Xie, Z., Feng, Y., & Chen, Z. (2018). Road extraction from high-resolution remote sensing imagery using deep learning. *Remote Sensing*, *10*(9). https://doi.org/10.3390/RS10091461

Xue, Y., & Forman, B. A. (2015). Comparison of passive microwave brightness temperature prediction sensitivities over snow-covered land in North America using machine learning algorithms and the Advanced Microwave Scanning Radiometer. *Remote Sensing of Environment*, *170*, 153–165. https://doi.org/10.1016/J.RSE.2015.09.009

Yang, J., Jiang, L., Luojus, K., Pan, J., Lemmetyinen, J., Takala, M., & Wu, S. (2020). Snow depth estimation and historical data reconstruction over China based on a random forest machine learning approach. *Cryosphere*, *14*(6), 1763–1778. https://doi.org/10.5194/tc-14-1763-2020

Yu, H., Zhang, X., Liang, T., Xie, H., Wang, X., Feng, Q., & Chen, Q. (2012). A new approach of dynamic monitoring of 5-day snow cover extent and snow depth based on MODIS and AMSR-E data from Northern Xinjiang region. *Hydrological Processes*, *26*(20), 3052–3061. https://doi.org/10.1002/HYP.8253

Yueh, S. H., Dinardo, S. J., Akgiray, A., West, R., Cline, D. W., & Elder, K. (2009). Airborne Ku-Band Polarimetric Radar Remote Sensing of Terrestrial Snow Cover. *IEEE TRANSACTIONS ON GEOSCIENCE AND REMOTE SENSING*, *47*(10), 3347. https://doi.org/10.1109/TGRS.2009.2022945

Zhang, X., Lu, W., Li, F., Peng, X., & Zhang, R. (2019). Deep feature fusion model for sentence semantic matching. *Computers, Materials and Continua*, *61*(2), 601–616. https://doi.org/10.32604/CMC.2019.06045

Zhong, X. Y., Zhang, T., Su, H., Xiao, X. X., Wang, S. F., Hu, Y. T., Wang, H. J., Zheng, L., Zhang, W., Xu, M., & Wang, J. (2021). Impacts of landscape and climatic factors on snow cover in the Altai Mountains, China. *Advances in Climate Change Research*, *12*(1), 95–107. https://doi.org/10.1016/J.ACCRE.2021.01.005

Zhong, X., Zhang, T., Kang, S., Wang, K., Zheng, L., Hu, Y., & Wang, H. (2018). Spatiotemporal variability of snow depth across the Eurasian continent from 1966 to 2012. *Cryosphere*, *12*(1), 227–245. https://doi.org/10.5194/TC-12-227-2018

Zhong, X., Zhang, T., & Wang, K. (2014). Snow density climatology across the former USSR. *Cryosphere*, *8*(2), 785–799. https://doi.org/10.5194/TC-8-785-2014

Zhu, J., Tan, S., King, J., Derksen, C., Lemmetyinen, J., & Tsang, L. (2018). Forward and inverse radar modeling of terrestrial snow using snowSAR data. *IEEE Transactions on Geoscience and Remote Sensing*, *56*(12), 7122–7132. https://doi.org/10.1109/TGRS.2018.2848642

Zhu, L., Zhang, Y., Wang, J., Tian, W., Liu, Q., Ma, G., Kan, X., & Chu, Y. (2021a). Downscaling snow depth mapping by fusion of microwave and optical remote-sensing data based on deep learning. *Remote Sensing*, *13*(4), 1–25. https://doi.org/10.3390/rs13040584

Zhu, L., Zhang, Y., Wang, J., Tian, W., Liu, Q., Ma, G., Kan, X., & Chu, Y. (2021b). Downscaling Snow Depth Mapping by Fusion of Microwave and Optical Remote-Sensing Data Based on Deep Learning. *Remote Sensing 2021, Vol. 13, Page 584*, *13*(4), 584. https://doi.org/10.3390/RS13040584

Zuniga, M. A., Habashy, T. M., & Kong, J. A. (1979). Active Remote Sensing of Layered Random Media. *IEEE Transactions on Geoscience Electronics*, *17*(4), 296–302. https://doi.org/10.1109/TGE.1979.294658

APPENDICES

Accuracy scores of models:

SVR- SD MEDIAN

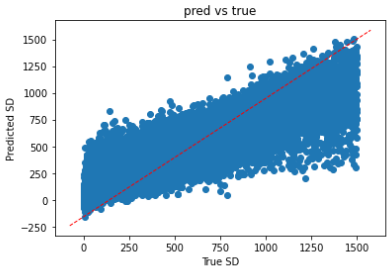

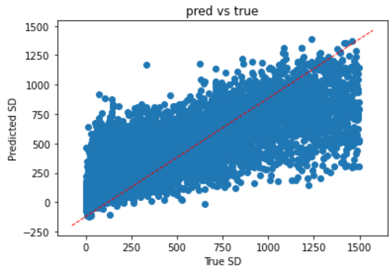

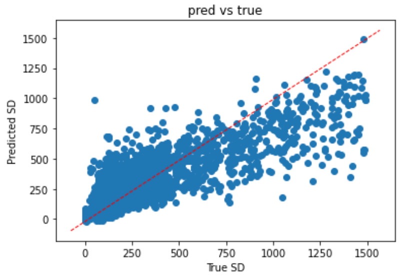

SVR- SD MEAN

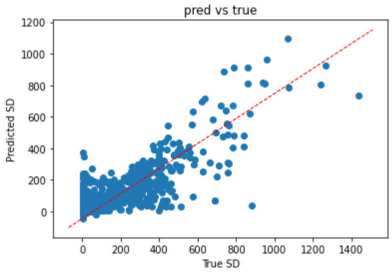

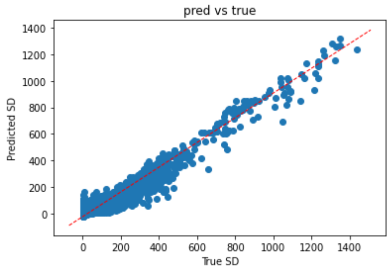

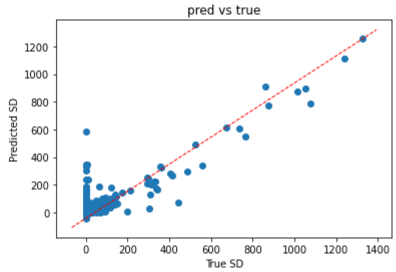

SVR- SWE MEAN

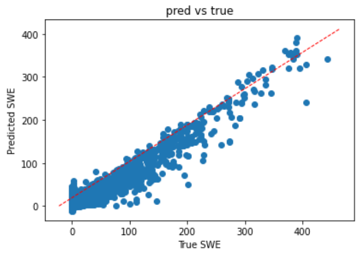

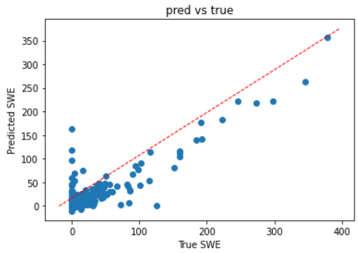

SVR- SD MEDIAN

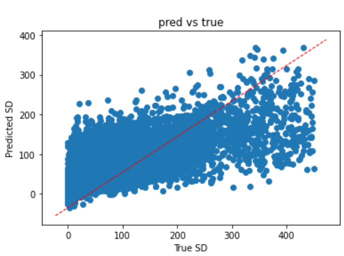

RFR- SD MEDIAN

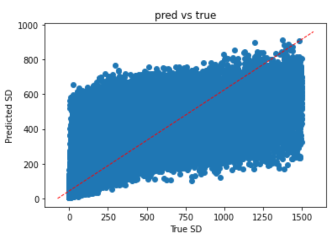

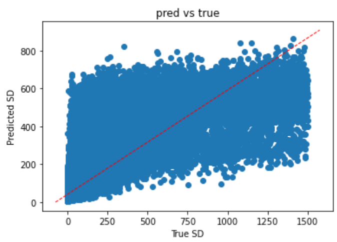

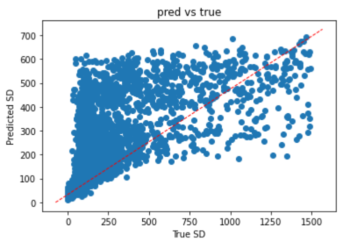

RFR- SD MEDIAN

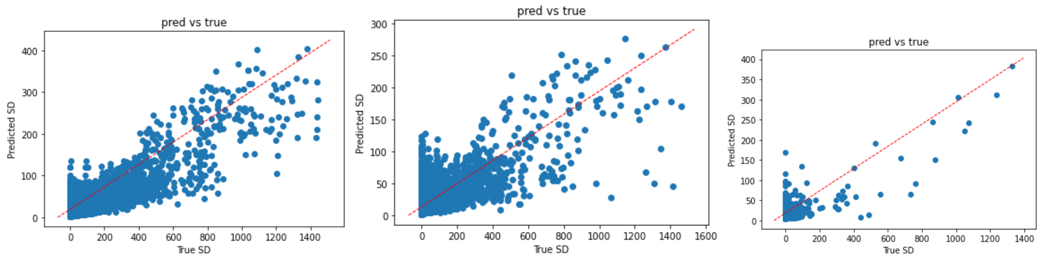

RFR- SWE MEAN

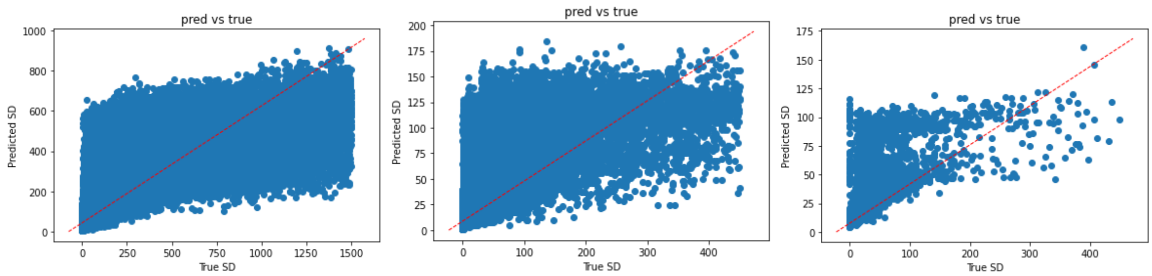

RFR- SWE MEDIAN

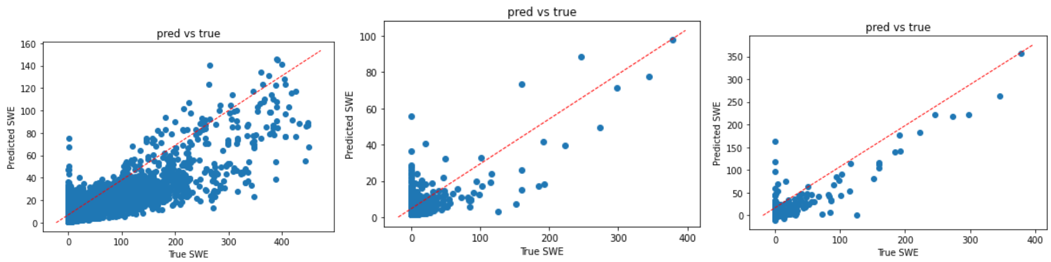

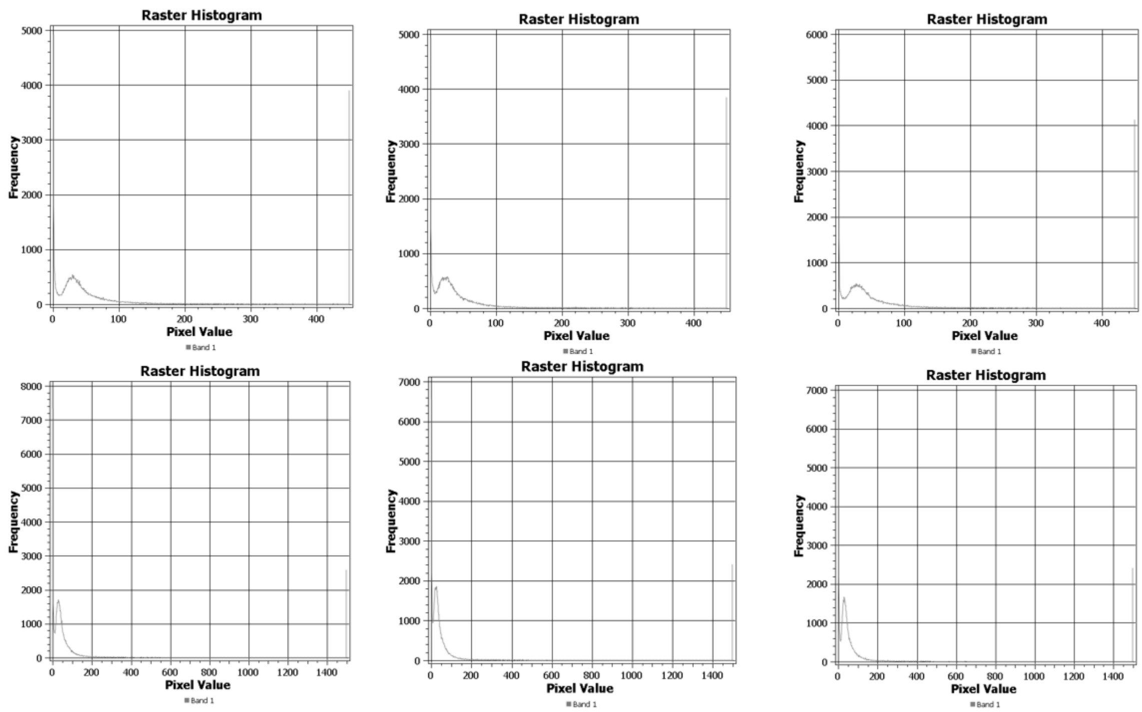

Sutlej Basin SWE (up) and SD(down) histograms for Feb 2017,2018,2019

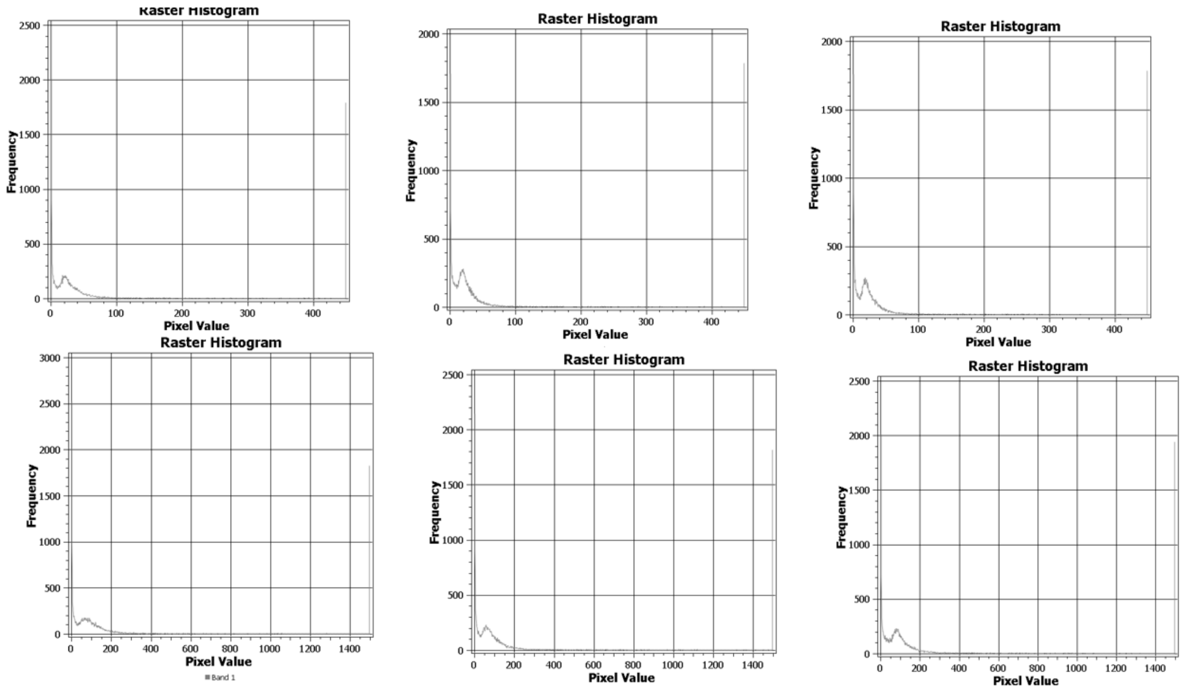

Beas Basin SWE (up) and SD(down) histograms for Feb 2017,2018,2019

HMASR Data Description

Table 1. Parameter Details

File name extensions	Parameters	Reference to Parameter Details
SWE_SCA_POST	Posterior snow water equivalent (SWE) and posterior fractional snow covered area (fSCA)	Table 2
SD_POST	Posterior snow depth (SD)	Table 3
SNOW_ALBEDO	Posterior snow albedo	Table 4
FORCING_POST	Posterior forcing variables	Table 5
MASK	Classification mask and non-seasonal snow/ice mask	Table 6

Table 4. Parameter Details for *SNOW_ALBEDO* files

Parameter	Description	Unit	Dimension
Snow_Albedo_Post	posterior snow albedo	-	225 x 225 x 366
Latitude	latitude	degrees N	225 x 1
Longitude	longitude	degrees E	225 x 1

Table 5. Parameter Details for *FORCING_POST* files

Parameter	Description	Unit	Dimension
PPT_Post	posterior surface precipitation	mm	225 x 225 x 366
Ps_Post	posterior surface pressure	mbar	225 x 225 x 366
q_Post	posterior reference-level specific humidity	kg/kg	225 x 225 x 366
Rl_Post	posterior downwelling longwave surface radiation	W/m^2	225 x 225 x 366
Rs_Post	posterior surface downwelling solar radiation	W/m^2	225 x 225 x 366
Ta_Post	posterior reference-level air temperature	K	225 x 225 x 366
Latitude	latitude	degrees N	225 x 1
Longitude	longitude	degrees E	225 x 1

Table 2. Parameter Details for *SWE_SCA_POST* files

Parameter	Description	Unit	Dimension
SCA_Post	posterior fSCA	-	225 x 225 x 5 x 366
SWE_Post	posterior snow water equivalent	m	225 x 225 x 5 x 366
Latitude	latitude	degrees N	225 x 1
Longitude	longitude	degrees E	225 x 1

Table 3. Parameter Details for *SD_POST* files

Parameter	Description	Unit	Dimension
SD_Post	posterior snow depth	m	225 x 225 x 5 x 366
Latitude	latitude	degrees N	225 x 1
Longitude	longitude	degrees E	225 x 1

Table 6. Parameter Details for *MASK* files

Parameter	Description	Unit	Dimension
Classification_mask	indicators of whether prior simulation or posterior update was performed within a certain pixel/year	-	225 x 225 x 18
Non_seasonal_snow_mask	indicators of whether a pixel was classified as non-seasonal snow/ice	-	225 x 225
Latitude	latitude	degrees N	225 x 1
Longitude	longitude	degrees E	225 x 1
Water_Year	water year corresponds to the classification mask	WY	18 x 1

Table 7. File Naming Convention

File Designator	Description
HMA_SR_D	Data set ID.
v[nn]	Data set version number.
N[latitude]	N for north, followed by a 3-digit latitude, e.g. N34_0 for 34° N indicating the latitude of the lower-left corner of the 1° latitude by 1° longitude file.
E[longitude]	E for east, followed by a 3- or 4-digit longitude, e.g. E66_0 for 66° E and E103_0 for 103° E indicating the longitude of the lower-left corner of the 1° latitude by 1° longitude file.
agg_16	This refers to a spatial aggregation factor of 16 from the original resolution of the DEM (30 m) to the model resolution (480 m).
[parameter]	Main data parameter. Options are SWE_SCA_POST, SD_POST, SNOW_ALBEDO, FORCING_POST, and MASK. More details on each individual file type can be found in Table 1 to Table 6.
WY[YYYY_YY]	WY is short for water year, followed by the starting year and the last two digits of the ending year. E.g. WY1999_00 refers to data for the period of 01 October 1999 to 30 September 2000.
.nc	File extension indicating this is a NetCDF file.